Dissolution control of highly soluble active pharmaceutical ingredients via cocrystallisation

by

Kudzanai Nyamayaro

Thesis submitted in fulfilment of the requirements for the degree
Master of Applied Sciences: Chemistry
in the Faculty of Applied Sciences at the

Cape Peninsula University of Technology

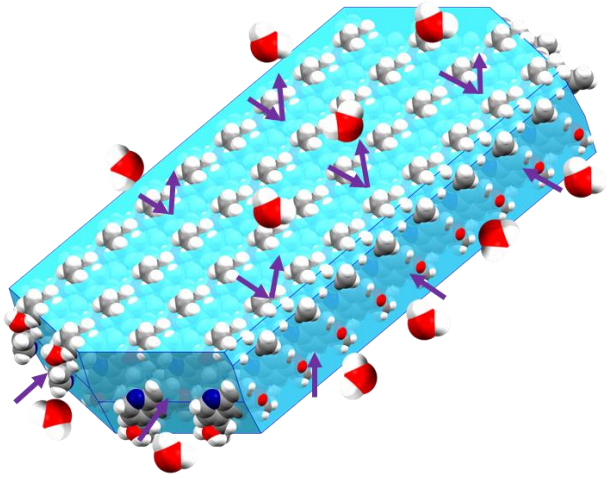

Supervisor: Professor Nikoletta B. Báthori
Co-supervisor: Dr Meredith Hearshaw

Cape Town
December 2017

The financial assistance of the National Research Foundation towards this research is acknowledged. Opinions expressed in this thesis and the conclusions arrived at, are those of the author, and are not necessarily to be attributed to the National Research Foundation.

DECLARATION

I, **Kudzanai Nyamayaro**, declare that the contents of this dissertation/thesis represent my own unaided work, and that the dissertation/thesis has not previously been submitted for academic examination towards any qualification. Furthermore, it represents my own opinions and not necessarily those of the Cape Peninsula University of Technology.

Signed

14/03/2018

Date

ABSTRACT

Crystal engineering involves the manipulation of intermolecular interactions to design functionalised crystalline materials and has proved to be an effective tool for the modification of physicochemical properties of active pharmaceutical ingredients (APIs). In the first section of this study, the aim was to systematically influence the rate of dissolution of a highly soluble active pharmaceutical ingredient using crystal engineering principles.

Salicylic acid (SA) was employed as a model API to form multicomponent crystals with a series of selected cinchona alkaloids, namely quinine (QUIN), quinidine (QUID), cinchonine (CINC), cinchonidine (CIND), N-benzylquininium chloride (NBQUIN), N-benzylcinchonidinium chloride (NBCIND) and N-benzylcinchoninium chloride (NBCINC). The resulting novel crystalline forms were found to be salts, and were characterised using single crystal X-ray diffraction, powder X-ray diffraction, differential scanning calorimetry and thermogravimetric analysis. The dissolution profiles of the salicylate salts, measured from an aqueous media using high performance liquid chromatography-mass spectroscopy, show a significant decrease in the rate of dissolution of SA. Subsequently, Hirshfeld surface analysis was used as a tool for quantitative and qualitative comparison of the crystal structures. This study indicates that the rate of dissolution can be successfully influenced by methodically adding extra hydrophobic groups onto the coformer.

In the second section, we applied the information obtained from the SA studies to acetylsalicylic acid (aspirin, ASA). We sought to improve its thermal stability and dissolution via the formation of new solid forms with the aforementioned cinchona alkaloids. We successfully synthesized a novel drug-drug salt of an analgesic, non-steroidal anti-inflammatory and antipyretic drug (ASA), and an antimalarial and analgesic drug (QUIN). The salt was formed both by using solution methods and liquid assisted grinding - a green chemistry technique. The salt exhibited physicochemical properties different from the parent drugs, and a reduced rate of dissolution.

ACKNOWLEDGEMENTS

Firstly, I would like to extend my gratitude to my supervisor Professor Nikoletta B. Báthori. I started working in her laboratory as a sophomore, and that experience was the first time I got exposed to research. Therefore, she is the very reason I developed a keen interest in research. I have gained an unbelievable amount of knowledge from Prof Báthori, not only regarding chemistry but about life as well. She has put a lot of effort into making me a better person both academically and socially, and for that I will always be thankful.

I would like to thank my co-supervisor Dr Meredith Hearshaw, and Dr Merrill Wicht and Dr Elise de Vries, for their support and encouragement. I am also grateful to Dr Ogheneochuko Oputu who taught me much about chromatography, and always found time from his busy schedule to lend a helping hand.

I would also like to thank the present and past members of the research group at CPUT, especially Sylvia Kantengwa who laid the groundwork for this work before her premature death. I would also like to thank all my friends, particularly Kelly Shunje and Nigel Sharara who have shared not only the hardships of obtaining single crystals with me, but have also shared many life experiences.

Lastly, I would like to thank my family. Much appreciation goes to my father who has sacrificed a lot to get me here. To Patricia, Tawanda, Farai, Tafadzwa, Tatenda, Fadzai and Munashe; thank your all for all your support and encouragement.

DEDICATION

To my parents

TABLE OF CONTENTS

LIST OF FIGURES

LIST OF TABLES

GLOSSARY OF TERMS

Terms/Acronyms/Abbreviations	Definition
a, b, c	Unit cell axes
API	Active Pharmaceutical Ingredient
ASA	Acetylsalicylic acid
CINC	Cinchonine
CIND	Cinchonidine
CSD	Cambridge Structural Database
DSC	Differential Scanning Calorimetry
FTIR	Fourier Transform Infra-Red spectroscopy
GRAS	Generally Regarded as Safe
H-bonds	Hydrogen bonds
HPLC-MS	High performance liquid chromatography - mass spectrometry
LAG	Liquid assisted grinding
NBCINC	N-benzylcinchoninium chloride
NBCIND	N-benzylcinchonidinium chloride
NBQUIN	N-benzylquininium chloride
PXRD	Powder X-ray diffraction
pK_a	Acid dissociation constant
ΔpK_a	Difference in acid dissociation constants
QUID	Quinidine
QUIN	Quinine
SA	Salicylic acid
SE	Solvent evaporation
SXRD	Single crystal X-ray diffraction
α	Angle between b and c in unit cell
β	Angle between a and c in unit cell
γ	Angle between a and b in unit cell

PUBLICATIONS FROM PAST RESEARCH

Chowdhury, M.; Ntiribinyange, M.; **Nyamayaro, K**.; Fester, V., Photocatalytic activities of ultra-small β-FeOOH and TiO_2 heterojunction structure under simulated solar irradiation. *Materials Research Bulletin* **2015,** *68*, 133-141.

Oputu, O.; Chowdhury, M.; **Nyamayaro, K**.; Cummings, F.; Fester, V.; Fatoki, O., A novel β-FeOOH/NiO composite material as a potential catalyst for catalytic ozonation degradation of 4-chlorophenol. *RSC Advances* **2015,** *5* (73), 59513-59521.

Oputu, O.; Chowdhury, M.; **Nyamayaro, K**.; Fatoki, O.; Fester, V., Catalytic activities of ultra-small β-FeOOH nanorods in ozonation of 4-chlorophenol. *Journal of Environmental Sciences* **2015,** *35*, 83-90.

CONFERENCE POSTER PRESENTATIONS

"Multicomponent crystals of baclofen", poster presented at the 23rd International Conference on the Chemistry of the organic Solid State, Stellenbosch, South Africa (April 2017).

"Dissolution control of highly soluble active pharmaceutical ingredients via cocrystallization", poster presented at the South African Chemical Institute Inorganic conference, Hermanus, South Africa (June 2017).

CONFERENCE ORAL PRESENTATION

"Dissolution control of highly soluble active pharmaceutical ingredients via cocrystallization", Flash Talk at the South African Chemical Institute Inorganic conference, Hermanus, South Africa (June 2017).

AWARD

Gold Medal Award for Flash Talk at the South African Chemical Institute Inorganic Conference (2017)

Chapter 1:

Introduction

1.1 Supramolecular chemistry

Supramolecular chemistry is a widely adopted field of chemistry; as such it has been defined in a myriad of ways. These ever-evolving definitions seek to encompass new aspects of the field that have been identified over the years. The story of supramolecular chemistry begins with the discovery of chlorine hydrate by sir Humphry Davy in 1810 and some of its milestones have been summarised by Steed and Atwood in 'Supramolecular Chemistry'.[1] The subsequent journey is marked by several significant events; the Nobel Prize in chemistry awarded to Donald J. Cram, Jean-Marie Lehn and Charles J. Pedersen in 1987 for their work in supramolecular chemistry marks the zenith of this journey. The architect of the term 'supramolecular chemistry', Jean-Marie Lehn, defines supramolecular chemistry as the chemistry of molecular assemblies and of the intermolecular bond.[2] Supramolecular chemistry focuses on the design and synthesis of supermolecules by utilising complementary recognition, and subsequent assembly, of well-defined subunits.[3] The self-assembly is achieved and maintained through noncovalent interactions such as hydrogen bonding, halogen bonding, coordination forces and π···π stacking. Basically, the synthesis of target molecules in supramolecular chemistry is achieved through non-covalent interactions; as such differentiating it from molecular chemistry, which involves formation of covalent bonds in synthesizing target molecules (Figure 1.1).

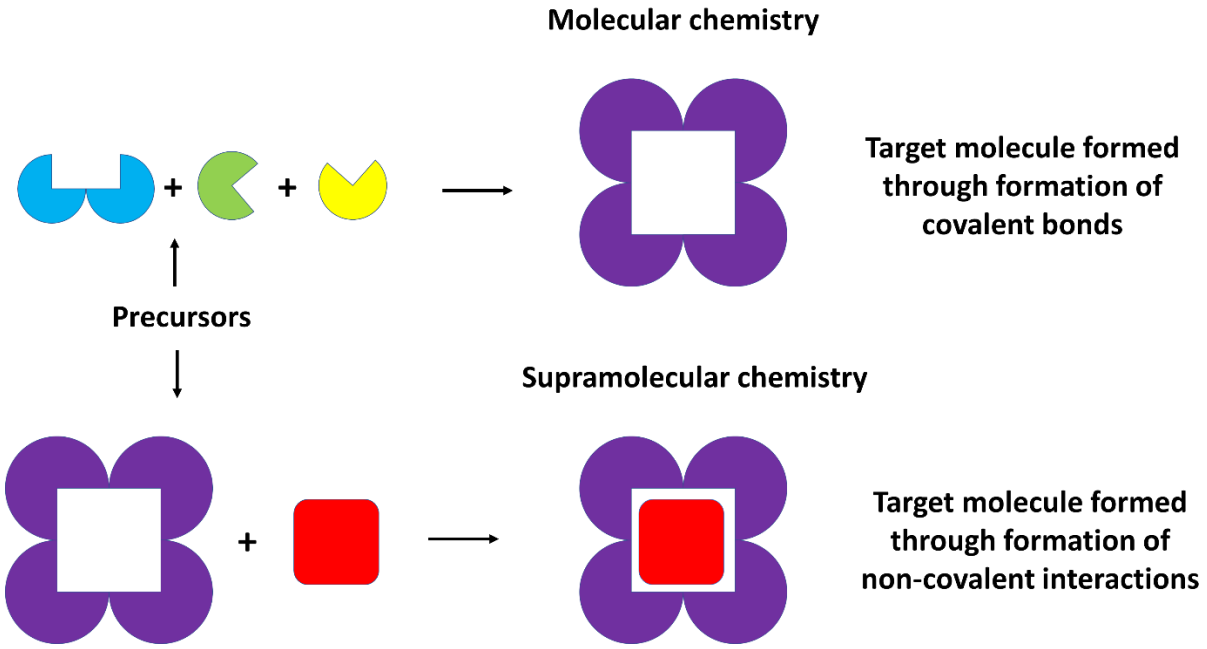

Figure 1.1 Supramolecular synthesis vs molecular synthesis.

1.2 Crystal engineering

The brief history of the origin of the term crystal engineering was given by Braga in his paper entitled 'Crystal engineering, Where from? Where to?'[4] The term crystal engineering was first recorded in the proceedings of the American Physical Society Meeting held in Mexico City in August 1955, where an abstract by Pepinsky entitled 'Crystal Engineering: a new concept in crystallography' appeared.[5] In 1962, von Hippel went on to pronounce the underlying principles of crystal engineering under the heading 'molecular engineering'.[6] Then in 1971, Schmidt redefined crystal engineering as *"…*to *'engineer' crystal structures having intermolecular contact geometries appropriate for chemical reaction*…".[7] This explanation was the basis for the current definition of crystal engineering by Desiraju, as "the understanding of intermolecular interactions in the context of crystal packing and in the utilisation of such understanding in the design of new solids with desired physical and chemical properties".[8] And so, the main interest areas of this field include: the study of intermolecular interactions, the study of packing modes with the aim of defining a design strategy, and the study of crystal properties and how they can be manipulated deliberately by varying the crystal packing.[9] As such, crystal engineering covers a wide array of scientific disciplines from the synthesis of smart materials,[10] statistical data analysis of structural information, gas storage,[11] organocatalysis,[12] to pharmaceutics.[13] Most relevant to the work presented here is the research in pharmaceutics. With the significant increase in understanding of the intricate processes involved in the assembly of molecules into a crystalline lattice, researchers are drawing nearer to the age of designing solid state forms of active pharmaceutical ingredients with predetermined properties.

1.3 Multicomponent crystals

Generally crystalline materials built from more than one different chemical entity have been referred to as cocrystals. There have been various definitions of the term 'cocrystal'; this is a consequence of the lack of consensus about the various parameters such as molecular charge or state of the constituents making up the crystal. For example, Stahly described a cocrystal as a molecular complex that contains two or more different molecules in the same crystal lattice.[14] Aakeröy gave a stricter description of a cocrystal as structurally homogeneous

crystalline material constructed from two or more discrete neutral molecular species in definite stoichiometric amounts that are solids at ambient conditions; i.e. crystals containing ions are excluded.[15] The difference between these two definitions is that Stahly does not consider the charge of the constituents of a cocrystal to be a separating factor, but Aakeröy specifies that a cocrystal must have neutrally charged constituents only. Thus, to avoid any ambiguity, the term multicomponent crystal is commonly used to describe crystalline solids built from more than one chemical entity. In this project, the term cocrystal will be used to refer to the crystals whose components are solids at ambient conditions, and that the interactions holding the components together are non-ionic. The different forms of multicomponent crystalline materials such as salts, cocrystals, solvates and polymorphs, are depicted in Figure 1.2.

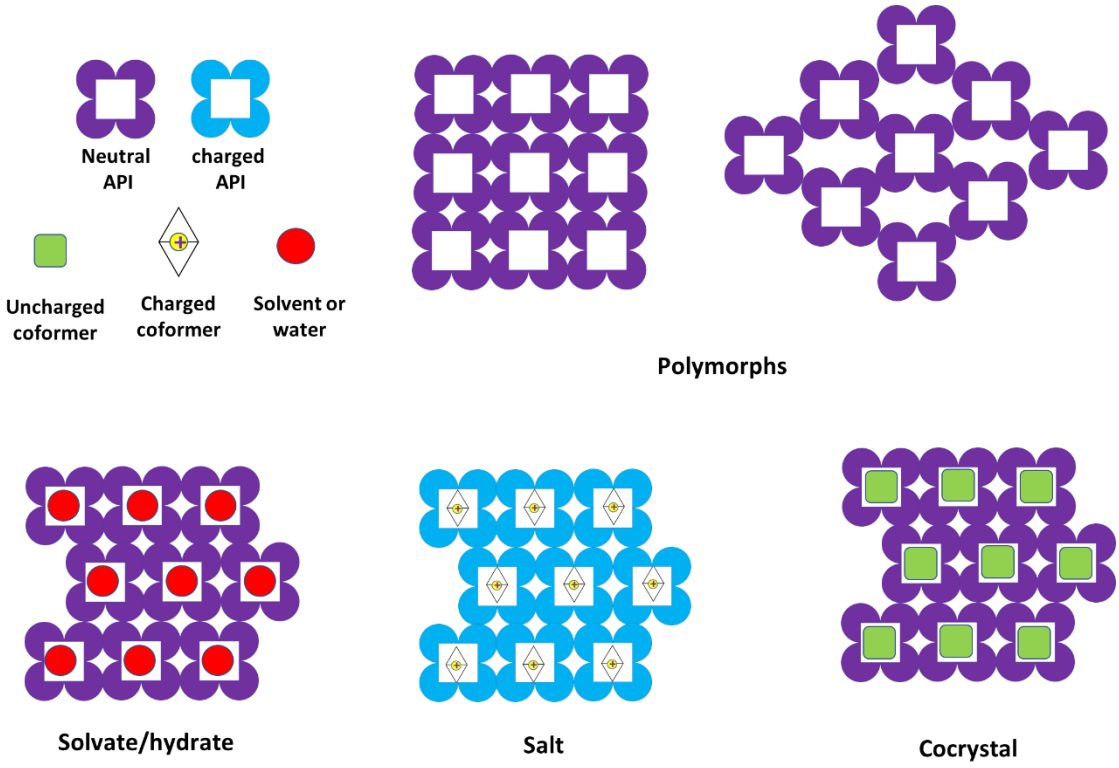

Figure 1.2 Comparative composition of a cocrystal, polymorph, solvate/hydrate and salt.

1.3.1 Cocrystals

In short, the components which make up a cocrystal must be solids at ambient conditions and interactions holding the components together are non-ionic. If one of the components of a cocrystal is an active pharmaceutical ingredient (API), the product is referred to as a pharmaceutical cocrystal. These pharmaceutical cocrystals have attracted attention because of their potential applicability to alter the physical and chemical properties of APIs without altering their biological action.[16] Furthermore, cocrystals can be made for nonionizable drugs, which are unable to from salts.[17] The resulting novel solid forms may have enhanced properties and thus can be marketed as a new solid form of the API. The physical properties, which are targeted for improvement include solubility, dissolution, hygroscopicity, stability, particle size distribution, density, taste, etc.[18]

1.3.2 Salts

The modification of the physical properties of APIs by adding a second component into the crystal lattice has been applied regularly within the pharmaceutical industry through the formation of salts.[19] More than half of marketed drugs are administered as salts.[20, 21] A salt is a multicomponent system where there is complete or partial transfer of an acidic hydrogen from one molecule to another, and as a result charged molecules, i.e. ions, are formed.[18]

1.3.3 Polymorphs

Polymorphism is the ability of a solid material to exist in more than one crystal form while retaining the same chemical composition.[22] There are two main types of polymorphism that can be observed in organic compounds, namely packing and conformational polymorphism. In packing polymorphism molecules are typically rigid, thus their conformation is very similar in the polymorphs, but they are arranged differently in the crystals. In conformational polymorphs molecules are more flexible and exist as distinctly different conformers. In practice, mixed types of polymorphs are often encountered.[23]

1.3.4 Solvates and hydrates

During crystallization, if the solvent is incorporated into the crystal structure the crystal is referred to as a solvate, and it is called a hydrate in case of inclusion of water. An estimated 33% of organic compounds have the ability to form hydrates, whereas about 10% of them are able to form solvates with organic solvents.[24] Solvate and hydrate formation has many implications in the pharmaceutical industry, because it affects the physicochemical properties of materials such as the solubility, dissolution rate, solid state stability, and bioavailability of APIs.[25] In addition, mechanical properties and deformation mechanisms such as tableting, grinding/milling can also vary upon hydration or solvation.[26]

1.4 Drug-drug multicomponent crystals

Fixed-dose combinations, or combination drugs, are a physical mixture of multiple active pharmaceutical ingredients formulated into a single tablet. Combination drugs have proved advantageous because of reasons such as increased patient compliance, reduction in number of prescriptions and greater therapeutic effects.[27,28] Despite their advantages, drug combinations pose some challenges during the formulation stages, such as instability, chemical interactions or solubility differences of the constituent APIs,[29] hence the need for alternative methods that address these challenges. Subsequently, multicomponent crystals formed between two selected APIs have been explored as an alternative approach for the synthesis of combination drugs.[30-35] The resulting API-API multicomponent crystal structure is distinctly different from the parent API structures, which may potentially translate into enhanced physicochemical properties compared to their fixed-dose combination. These properties may include improved solubility and dissolution.

1.5 Intermolecular interactions

The constituents of crystalline materials are held together in a three-dimensional structure by many forms of non-covalent interactions; either repulsive or attractive in nature. Some of the more important interactions are summarised in Figure 1.3. In the gas phase, the energy and geometry of the interactions between isolated molecules can be calculated. In contrast,

in the solid phase the close packed nature of the crystalline material makes the calculation of the interaction energies increasingly difficult.[36] As such, to get a better understanding of the stability of crystal structures, it is essential that solid state chemists and computational chemists study both long range and short range intermolecular interactions.

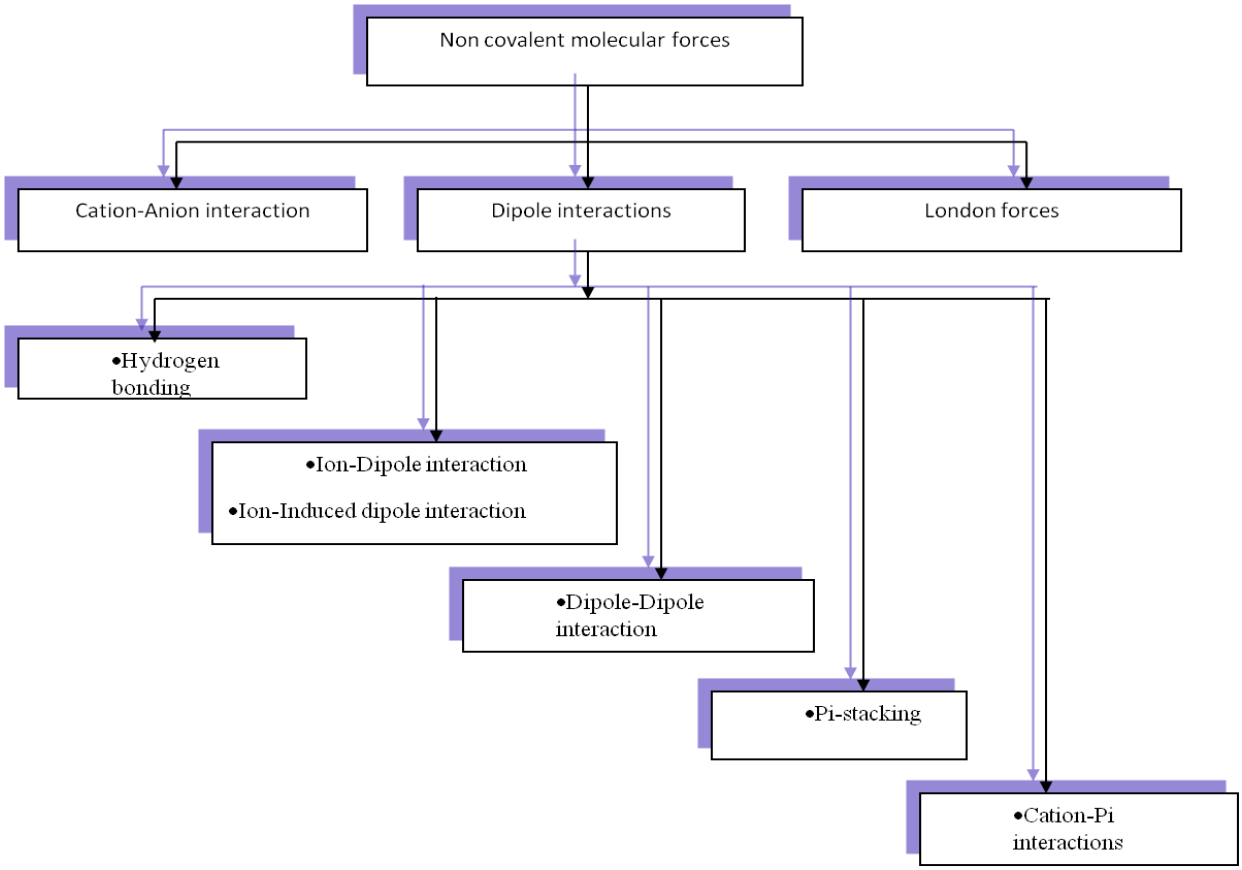

Figure 1.3 Summary of non-covalent interactions.

The non-covalent molecular forces (intermolecular interactions) are mainly electrostatic in nature. Their general properties are dependent on strength (Table 1.1), direction and distance. Intermolecular interactions can be sub-divided into cation-anion interactions (ion-ion), dipole interactions (ion-dipole, dipole-dipole, hydrogen bonding, cation-π, π- π stacking) and London forces (*van der Waals* interactions). Ion-ion interactions are the strongest and they are non-directional, while the strength of the ion-dipole and the dipole-dipole interactions is maximised when the geometry is optimal. Hydrogen bonds are directional and vary in strength. Similarly, the strength of the π-type interactions (cation-π, π-π stacking) also

vary. The strength of the *van der Waals* interactions heavily depends on the polarizability of the species and their distance from each other, they are also non-directional and thus their use in design of crystalline phases is limited.

Table 1.1 Summary of interaction energies.[37]

Interactions	Strength (kJ mol^{-1})
Ion-ion	200-300
Ion-dipole	50-200
Dipole-dipole	5-50
Hydrogen bonding	4-120
Cation-π	5-80
π-π	0-50
van der Waals	<5

1.5.1 Hydrogen bonds

The most important interaction in crystal engineering is the hydrogen bond (H-bond), which can be regarded as type of dipole-dipole interaction. The importance of the H-bond stems from its role in molecular associations. H-bonds in supramolecular chemistry control and direct the structure of molecular associations, a function ascribed to their strength and directionality. The term 'hydrogen bond' was first used by Pauling in 1935,[38] and its detailed explanation was given in 1939. Pauling's definition articulates that "under certain conditions an atom of hydrogen is attracted by rather strong forces to two atoms, instead of only one, so that it may be considered to be acting as a bond between them".[39] The current working definition of a hydrogen bond by the IUPAC describes it as an interaction in which a hydrogen atom attached to an electronegative atom (electron withdrawing group) is attracted to a neighbouring dipole on an adjacent molecule or functional group.[40] Hydrogen bonds are described by both geometric and energy parameters.

Hydrogen bonds are depicted as D-H···A; where D is for donor, H for hydrogen, and A for acceptor. The geometry of the H-bond is described by the distances D-H (r), H···A (d) and D-A (D), and in addition by the angle D-H···A (θ). Since H-bonds are long range interactions, the hydrogen can interact with more than one acceptor resulting in furcation; thus, there are several hydrogen bond geometries. Figure 1.4 portrays the definitions of the geometric parameters and Figure 1.5 shows the various types of hydrogen bond geometries.

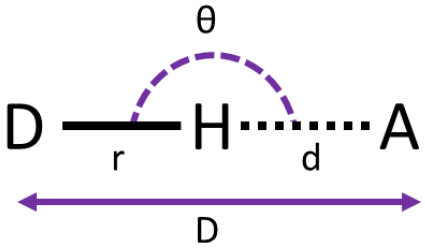

Figure 1.4 Definition of the H-bond geometric parameters.

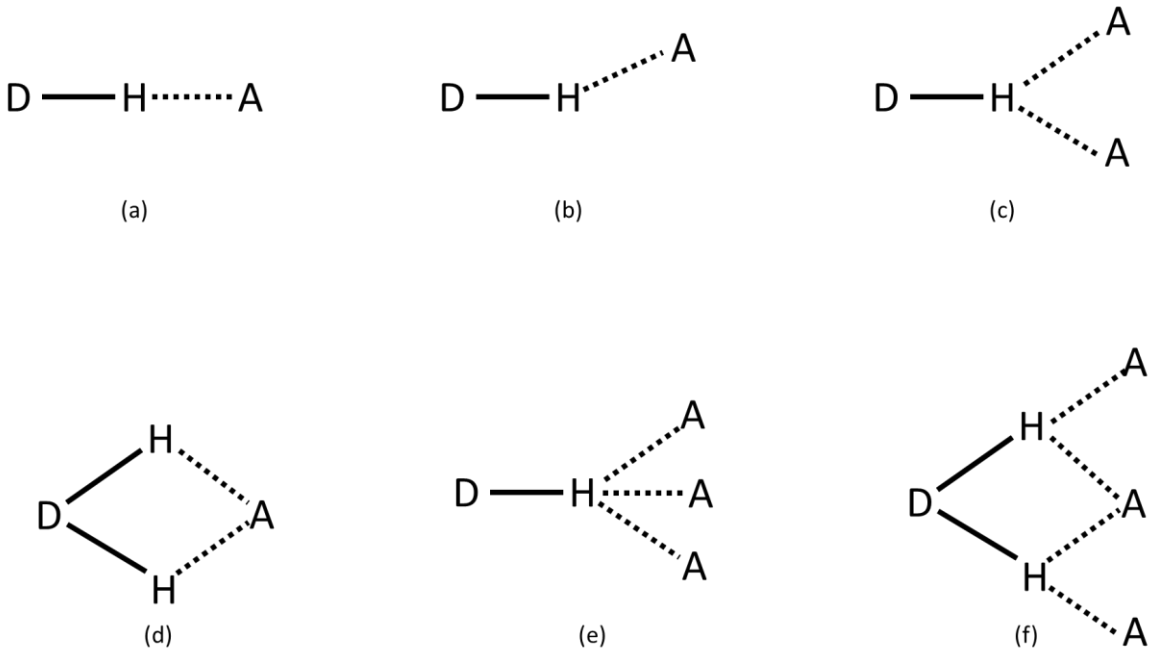

Figure 1.5 Types of hydrogen bonding geometries; (a) linear (b) bent (c) donating bifurcated (d) accepting bifurcated (e) donating trifurcated and (f) three centre bifurcated.

The combination of geometric and energy values enables the classification of hydrogen bonds into three categories: strong, moderate and weak. Table 1.2 shows the parameters of these hydrogen bonds.[1] Strong hydrogen bonds are characterized by a D···A of between 2.2-2.5 Å, an angle (θ) close to 180° (linear) and they have bond energies in the range of 60-120 KJ mol^{-1}. Moderate hydrogen bonds are the most common type; with D···A from 2.6-3.1 Å, θ range between 135 to 180° and bond energies ranging from 16-60 kJ mol^{-1}. They are formed between neutral donor and neutral acceptor groups via lone pair electrons, for example O-H···O-H. Weak hydrogen bond interactions can be found between poor donors, such as C-H moieties, and poor acceptors, like π-electron clouds. D···A is longer (3.2–4.0 Å) and the θ values cover a wider range (110-180°).[37]

Table 1.2 Properties of hydrogen bonding interactions.[1]

	Strong	Moderate	Weak
Bond energy (kJ.mol^{-1})	60–120	16–60	<12
Bond lengths (Å)			
H···A	1.2–1.5	1.5–2.2	2.2–3.2
D–A	2.2–2.5	2.5–3.2	3.2–4.0
D–H···A bond angle(°)	175–180	130–180	90–150
Examples	[F–H–F]$^-$	O–H···O–H	C–H···O
		O–H···N–H	
		N–H···O=C	
		N–H···O–H	
		N–H···N–H	

1.6 Supramolecular synthons

To correlate molecular structures with crystal structures, different models have been put forward by crystal engineers in an attempt to give plausible explanations. For instance, Kitaigorodskii proposed a model based solely on 'close packing' of the building blocks of the crystal structure (geometric model).[41] However, such a model or models proposed based only on interaction hierarchy (chemical model) would fail to propose a realistic picture of the crystal structure.[42] And so, the concept of supramolecular synthons was introduced; a model that combines both the chemical elements of molecular recognition and geometrical requirements of crystal packing. Supramolecular synthons were defined by Desiraju as "structural units within supermolecules which can be formed and/or assembled by known or conceivable synthetic operations involving intermolecular interactions".[43] These synthons are recurring and transferable interactions that can be used to logically guide the aggregation of molecules into a crystal structure.

Supramolecular synthons have significantly aided in the design of multicomponent crystal synthesis.[44-46] Supramolecular synthons may be classified in two categories: homosynthons and heterosynthons. The homosynthon is formed between identical functional groups, while the heterosynthon is built from different functional groups or complementary donor and acceptor groups.[47] Figure 1.6 shows some examples of supramolecular synthons. It is worthwhile to note that heterosynthons, i.e. interaction of different functional groups, are highly robust and transferable and thus play a crucial role in cocrystal synthesis.[48]

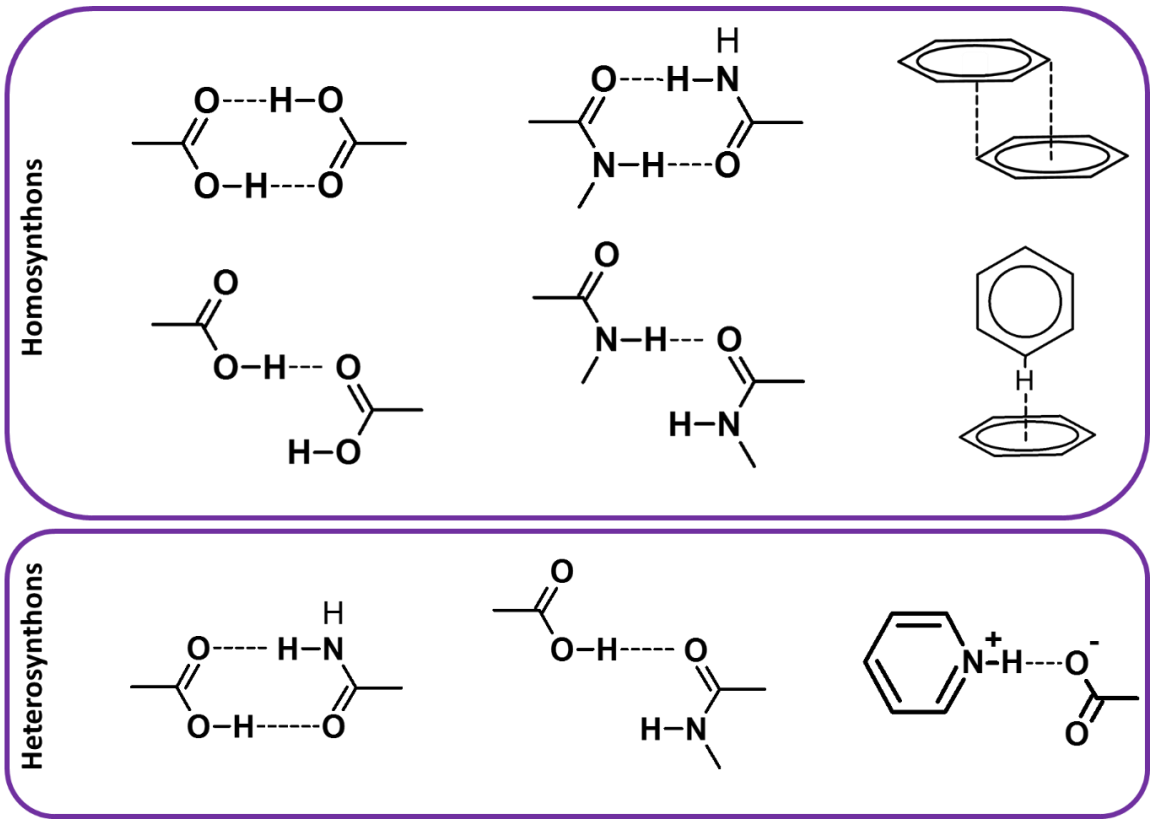

Figure 1.6 Examples of supramolecular synthons.

1.7 Physicochemical properties

There are several physicochemical properties of a drug which include solubility, permeability, chemical stability, etc; however, of interest to this project are solubility and dissolution rate. Sometimes, dissolution, dissolution rate, intrinsic dissolution rate and solubility have been used interchangeably, which gives the impression that they describe the same properties. However, each of them represent a disparate property.

1.7.1 Drug dissolution

Drug dissolution refers to the mechanism by which a solid drug dissolves into a liquid medium at a specified temperature. Many theories have been put forward to delineate the process of dissolution, but the diffusion layer model has proved to be the most sufficient for pharmaceutical applications. The model presumes the presence of a thin stagnant diffusion layer separating the solid liquid interface and the bulk solution. The process of dissolution would involve the movement of the solid from the solid-liquid interface into the stagnant diffusion layer, and then into the bulk solution down a concentration gradient (Figure 1.7).[49]

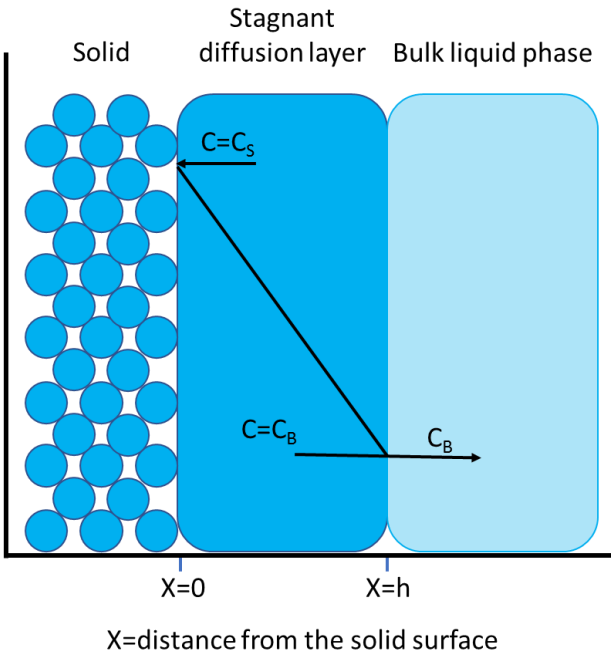

Figure 1.7 Diffusion by the diffusion layer model.[49]

1.7.2 Drug dissolution rate

The rate at which the solid moves from the solid-liquid interface into bulk solution is referred to as the dissolution rate, or the kinetics of dissolution. The rate of dissolution is expressed as equation 1; the Nernst-Bruner diffusion layer model of the Noyes-Whitney equation.[50]

$$\frac{dW}{dt} = \frac{DA}{h}(C_S - C_B) \qquad (eq.\ 1)$$

where $\frac{dW}{dt}$ is the rate of mass transfer of dissolved solute across the diffusion layer per unit time from a unit surface area (A), C_B is the concentration of the drug in the bulk solution, and C_S is the saturation solubility of the solute in the diffusion layer. It can be inferred from equation 1 that the dissolution is governed by the difference between the saturation solubility in the diffusion layer and the concentration of the drug in the bulk solution; $(C_S - C_B)$.[19] This observation has two implications. Firstly, if the rate of absorption of the drug from the bulk solution is less than the dissolution rate, C_B increases and approaches C_S, thereby limiting any further dissolution. Secondly, if the rate of absorption of the drug from the bulk solution is greater than the rate of dissolution, $(C_S - C_B)$ approaches C_S and thus the rate of absorption is limited by the dissolution rate. The latter of the two scenarios is typical of poorly soluble drugs; hence, change in the rate of dissolution of an active pharmaceutical ingredient has a direct impact of the rate of absorption, which in turn affects the bioavailability.

1.7.3 Solubility

Solubility is the equilibrium state of dissolution, were the drug that is in the solid phase is in equilibrium with the drug in the solution phase in a saturated solution. The IUPAC definition of solubility is "the analytical composition of a saturated solution expressed as a proportion of a designated solute in a designated solvent".[51] In simpler terms, the solubility is the amount of a solid substance that goes into a given solution until a point of supersaturation is achieved. The solubility of a substance depends on the solvent used, temperature and pressure. Solubility is generally expressed as a concentration, either by mass (g of solute per kg of solvent, g per L of solvent, molarity, molality, mole fraction) or other units of concentration. Moreover, solubility can also be expressed in terms of maximum volume or mass of a solvent. (Table 1.3)

Table 1.3 Solubility terms given by the United States Pharmacopeia and National Formulary.

Descriptive term	Parts of solvent required for 1 part of solute
Highly soluble	≤ 1
Freely soluble	1 to 10
Soluble	10 to 30
Sparingly soluble	30 to 100
Slightly soluble	100 to 1000
Very slightly soluble	1000 to 10000
Practically insoluble, or insoluble	≥10000

Several terms describing solubility have been used, each term based on a different method used to measure the solubility. These terms include: apparent solubility, apparent equilibrium solubility, kinetic solubility, precipitation solubility, thermodynamic solubility and equilibrium solubility. In the pharmaceutical industry, the most important methods for solubility determination are kinetic and equilibrium solubility. Kinetic solubility is the concentration of a given compound in a solution when the precipitate appears.[52] Measurement is generally conducted through nephelometric or turbidimetric methods, which have the advantage of being fast. However, they over-predict the solubility values and so are mostly used to place solubility in a hierarchy during high-throughput screening.

Equilibrium solubility is the saturation solubility of the solute in equilibrium with the excess undissolved solute and usually the shake-flask method is used for its determination. Equilibrium solubility more accurately represents the true solubility, but like every other solubility determination, it is dependent on several factors, such as solute purity, time, particle size, solvent, pH, temperature, methodology, etc.

The Biopharmaceutics classification system is a framework for categorising drugs into four classes according to their aqueous solubility and permeability.[53] The classification is as follows: (i) high solubility and high permeability drugs which are designated as BCS class I drugs; (ii) low solubility and high permeability drugs as BCS class II; (iii) high solubility and low permeability drugs are classified as BCS class III, and lastly (iv) those with low solubility and low permeability are categorised as BCS class IV drugs. The approximate percentage of pharmaceutical compounds, for both marketed drugs and drug candidates, that fall into each category is given in Figure 1.8.[54] Poorly soluble molecules constitute approximately 40% of approved drugs and nearly 90% of developmental pipeline drugs.[55]

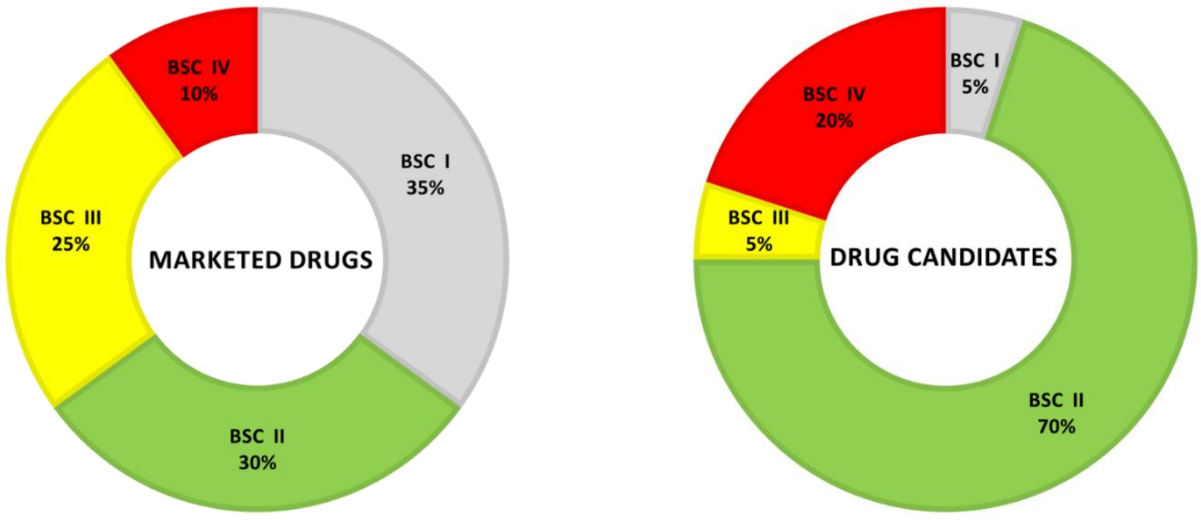

Figure 1.8 BCS classification of marketed drugs and drug candidates.

1.8 Mechanochemistry

Mechanochemistry is essentially the use of mechanochemical reactions to perform synthesis. The official definition of a mechanochemical reaction by IUPAC is: 'a chemical reaction that is induced by mechanical energy'.[56] Mechanochemistry can be traced back to the eighteenth century, when Faraday recorded a reaction in 1820 in which AgCl was reduced to Ag by grinding AgCl and Zn together using a mortar and pestle.[57, 58] Over the years, there have been several fields in which mechanochemistry has been successfully utilised. These fields include catalysis, organic synthesis, metal organic frameworks, supramolecular chemistry, etc. The role of mechanochemistry in the development of pharmaceuticals was described by Delori *et al* and it was highlighted how mechanochemistry has been successfully used to screen and synthesize metal organic pharmaceutical derivatives.[59]

Multicomponent crystals (polymorphs, solvates, salts and cocrystals) are usually synthesized using solution methods. However, the use of solvents introduces challenges in the synthesis of pharmaceutical multicomponent crystals, and these problems include added cost to production, environmental pollution, solubility issues, unwanted solvate or hydrate formation and solvolysis.[59] Considering these challenges, mechanochemistry presents itself as an attractive alternative. Several groups have demonstrated how multicomponent pharmaceutical compounds can be formed mechanochemically through neat grinding.[60-62] In addition, liquid assisted grinding (LAG), addition of small volume of solvent when grinding- provides a significant improvement in kinetics of formation without portraying the same disadvantages as solution methods.[63]

1.9 Research objectives

The probability that a pharmaceutical compound successfully goes through all drug trials is very small. It is estimated that from a group of more than 10000 promising drug candidates only one compound will eventually become a marketed drug.[64] In addition, there are some drugs which are on the market but do not work at 100% efficiency. The main reason, for both these cases, being that these APIs exhibit some poor biopharmaceutical properties (Figure 1.9).[65] The development of a drug candidate needs significant amount of invested capital, thus it is understandable that much research has been put into improving the physical properties of drug candidates in the development phase.

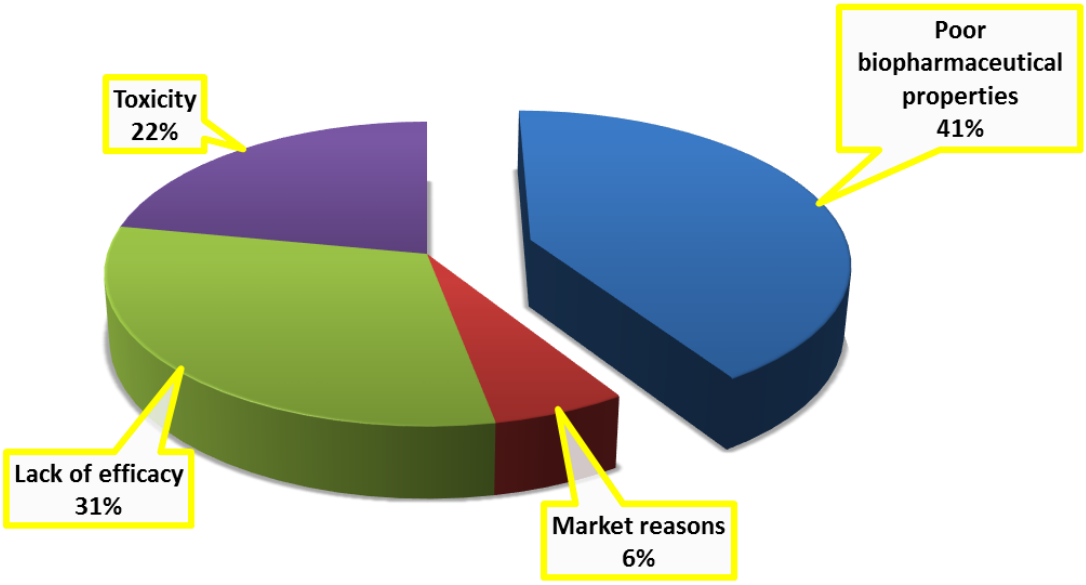

Figure 1.9 Reasons why prospective drug candidates fail during development.

In most cases the identified API has low aqueous solubility whilst in some cases exhibits extremely high solubility. In instances where the solubility is high, it might be necessary to reduce it. The drugs that characteristically have high solubility are employed in immediate release formulations. The challenge is that immediate release formulations must be consumed frequently, which may cause side effects in patients. And so, extended release formulations, that are taken less frequently, are usually developed as an alternative.

It is assumed that the physical properties of a solid can be explained from the long range ordered arrangement of its constituent molecules. And so, manipulation of this long range ordered arrangement, using crystal engineering, will subsequently result in the modification of the physical properties.[66-68] One way of achieving this effect is by introducing a second molecule into the solid's crystalline lattice. The product formed on introduction of a second molecule is one of the multicomponent crystal forms. Parallel to our research, Spinelli *et al* employed this same strategy to synthesize new solid forms of venlafaxine; an antidepressant marketed as a hydrochloride that has high solubility in water. They managed to obtain a coumarate salt that had reduced dissolution rate and so might present a new extended release formulation.[69] While cocrystal/salt formation is a well-accepted method for improving

solubility of poorly soluble drug candidates, there are very few examples that can be found in literature where crystal engineering has been fruitfully employed to control the rate of release of very soluble drugs.[70, 71]

Salicylic acid (2-hydroxybenzoic acid, SA) was employed as a model, highly soluble API. SA has anti-inflammatory, analgesic and antipyretic properties, but is mainly used as keratolytic agent in topical formulations.[72] Several studies on the controlled release of SA have been conducted, mainly by incorporating it into poly(anhydrideesters),[73,74] dendrimers,[75] biopolymers,[76] micelles,[77] polyurethanes,[78] and its release directed by the nature and degradation of the polymer.[79]

As an alternative, the objective of this contribution is to systematically influence the rate of dissolution of highly soluble active pharmaceutical compounds by using the crystal engineering approach. Salicylic acid (SA) was employed to form a series of multicomponent crystals with selected cinchona alkaloids, namely quinine (QUIN), quinidine (QUID), cinchonine (CINC), cinchonidine (CIND), N-benzylquininium chloride (NBQUIN), N-benzylcinchonidinium chloride (NBCIND) and N-benzylcinchoninium chloride (NBCINC).

The experimental design strategy was as depicted in Figure 1.10. SA was chosen because of its relatively high solubility of 4.14 g/L at 40°C and 2.48 g/L at 25°C,[80] and so it served as a good target for our experiments designed to investigate the dissolution control of a highly soluble compound. The cinchona alkaloids were used for their ability to form O-H···N, O-H···$^{+}$N or N^{+}-H···O^{-} heterosynthons with carboxylic acids; furthermore, the N-benzyl substituted cinchona alkaloids were utilised to investigate the effect of increased hydrophobicity of the coformer on the rate of dissolution. Crystal structures are discussed in addition to the observed rate of dissolution. Additionally, structure property relations were investigated using Hirshfeld surface analysis.

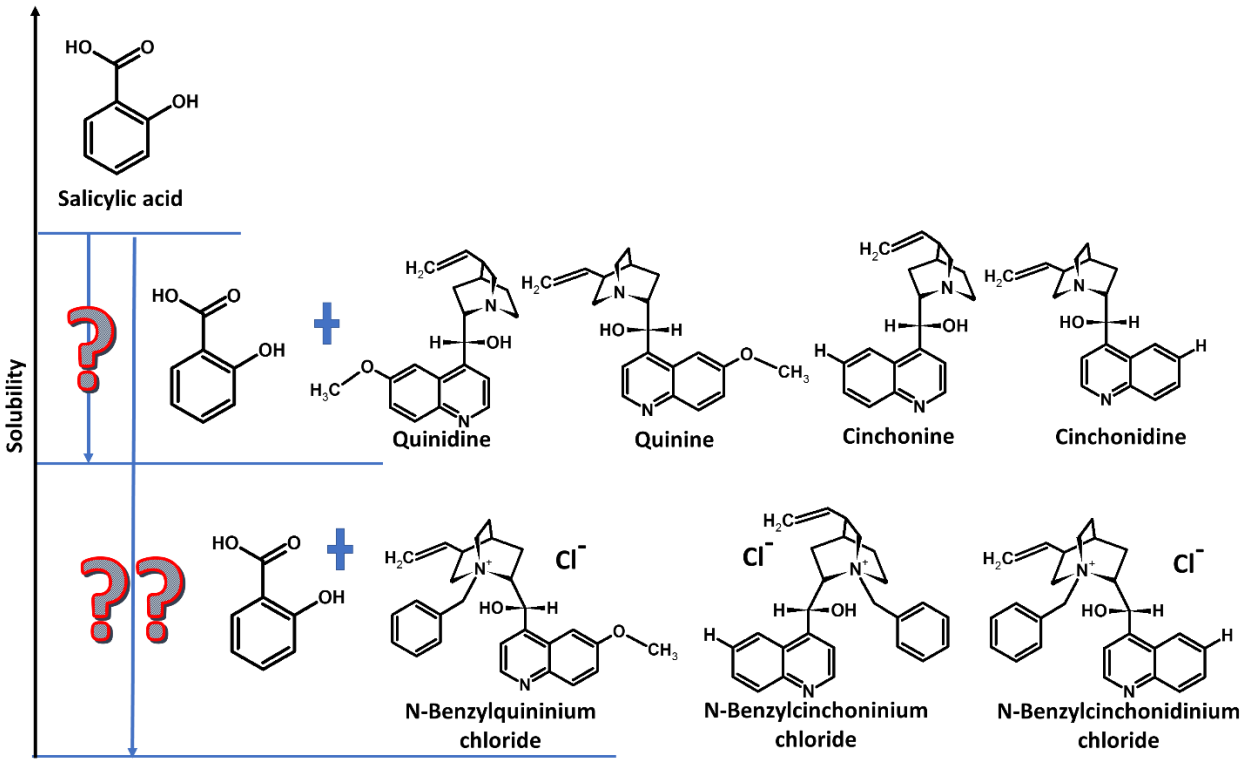

Figure 1.10 Design strategy for the modification of the rate of dissolution.

In the second section, we used acetylsalicylic acid (aspirin, ASA) as a more complex drug and attempted to form new multicomponent crystals with the aforementioned cinchona alkaloids; also with the aim of controlling the rate of dissolution.

ASA is an analgesic, non-steroidal anti-inflammatory and antipyretic drug.[81] In addition, ASA is employed as an antithrombotic agent, its antiplatelet activity makes it a popular prescription for combating heart attacks and strokes.[82] Quinine is a cinchona alkaloid that belongs to the aryl amino alcohol group of drugs. It acts schizonticidally against intra-erythrocytic malaria parasites, and gametocytocidal for *Plasmodium vivax* and *Plasmodium malariae*. Furthermore, quinine has analgesic properties.[83] Both quinine and aspirin are on the WHO model list of essential medicines.[84].

We investigated the applicability of cocrystallisation for the development of a multicomponent combination drug of quinine and aspirin. The multicomponent crystal with properties conferred from each API could solve the poor biopharmaceutical properties associated with quinine and aspirin. For instance, quinine is a BCS II drug and is practically insoluble in water (0.53 g/L);[85] in contrast, aspirin is a BCS III drug and is highly soluble in water

(3.33 g/L).[86] The combination of these two drugs may present the opportunity to simultaneously increase the solubility of quinine and reduce the solubility of aspirin. In addition, quinine has a low therapeutic index, and so has substantial adverse effects associated with its use;[87] such as headaches and abdominal pain.[88] Thus a cocrystal of quinine with an analgesic and non-steroidal anti-inflammatory drug, such as ASA, would provide pain relief from these adverse effects.

Furthermore, ASA decomposes in high humidity environments to form salicylic acid and acetic acid, which reduces the shelf life of its formulations. For this reason, we also aimed to stabilise aspirin toward hydrolysis. This goal poses a major challenge with the screening of multicomponent crystals of ASA; primarily because the usual solution methods used for cocrystallisation make use of solvent media in which water is inherently found. To circumvent the problems associated with hydrolysis of aspirin, we employed mechanochemistry to screen for new solid forms of aspirin. The single crystal structures and rate of dissolution were analysed.

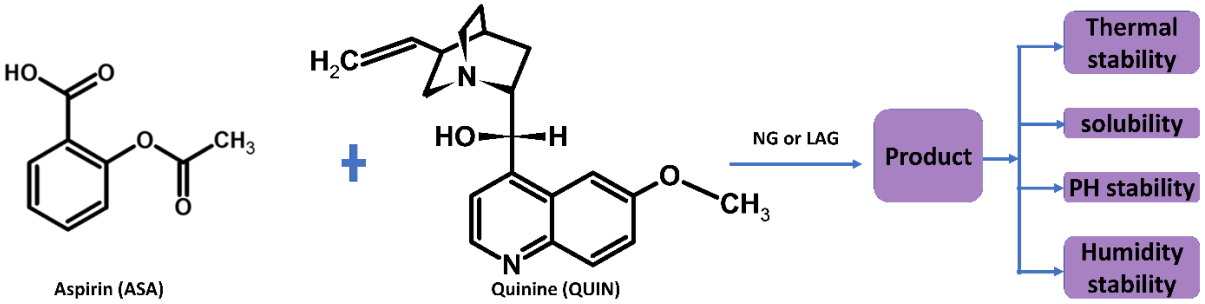

Figure 1.11 Design strategy for the synthesis of an API-API multicomponent crystal of aspirin and quinine.

In summary, the objectives of this research are three-fold. Firstly, we aimed to systematically influence the rate of dissolution of SA and ASA. Secondly, we were investigating the possibility of forming drug-drug multicomponent crystals with enhanced properties relative to the parent APIs. Lastly, we investigated the advantages of mechanochemistry for the synthesis of multicomponent crystals that are difficult to attain using solution methods.

1.10 References

1. J. W. Steed and J. L. Atwood, *Supramolecular Chemistry*, Wiley, 2013.
2. J.-M. Lehn, *Angewandte Chemie International Edition in English*, 1988, **27**, 89-112.
3. J. D. Dunitz, in *Perspectives in Supramolecular Chemistry*, John Wiley & Sons, Ltd., 2007, pp. 1-30.
4. D. Braga, *Chemical Communications*, 2003, 2751-2754.
5. Anonymous, *Physical Review*, 1955, **100**, 952-953.
6. A. R. von Hippel, *Science, guided by molecular understanding, takes up the challenge to create materials for the future*, 1962, **138**, 91-108.
7. G. M. J. Schmidt, *Journal*, 1971, **27**, 647.
8. G. R. Desiraju, *Crystal engineering: the design of organic solids*, Elsevier, 1989.
9. G. R. Desiraju, *Angewandte Chemie International Edition*, 2007, **46**, 8342-8356.
10. C. Zhang, Y. Yan, L. Sun, Z. Liang and J. Li, *CrystEngComm*, 2016, **18**, 4102-4108.
11. P. Sozzani, S. Bracco, A. Comotti, L. Ferretti and R. Simonutti, *Angewandte Chemie International Edition*, 2005, **44**, 1816-1820.
12. J. V. Alegre-Requena, E. Marques-Lopez, R. P. Herrera and D. D. Diaz, *CrystEngComm*, 2016, **18**, 3985-3995.
13. M. Khan, V. Enkelmann and G. Brunklaus, *Journal of the American Chemical Society*, 2010, **132**, 5254-5263.
14. G. P. Stahly, *Crystal Growth & Design*, 2007, **7**, 1007-1026.
15. C. B. Aakeroy and D. J. Salmon, *CrystEngComm*, 2005, **7**, 439-448.
16. J. Kos, M. Pentakova, Z. Oktabec, L. Krejcik, Z. Mandelova, P. Harokova, J. Hruskova, T. Pekarek, O. Dammer and M. Tkadlecova, *Molecules*, 2011, **16**, 3740-3760.
17. D. J. Good and N. Rodríguez-Hornedo, *Crystal Growth & Design*, 2009, **9**, 2252-2264.
18. N. Schultheiss and A. Newman, *Crystal Growth & Design*, 2009, **9**, 2950-2967.
19. S. M. Berge, L. D. Bighley and D. C. Monkhouse, *Journal of Pharmaceutical Sciences*, 1977, **66**, 1-19.
20. P. H. Stahl and C. G. Wermuth, *Chemistry International*, 2002, **24**, 21.
21. J. K. Guillory, *Journal of Medicinal Chemistry*, 2003, **46**, 1277-1277.
22. J. W. Mullin, *Crystallization*, Butterworth-Heinemann, 2001.
23. A. J. Cruz-Cabeza and J. Bernstein, *Chemical Reviews*, 2014, **114**, 2170-2191.
24. H. D. Clarke, K. K. Arora, H. Bass, P. Kavuru, T. T. Ong, T. Pujari, L. Wojtas and M. J. Zaworotko, *Crystal Growth & Design*, 2010, **10**, 2152-2167.
25. S. R. Vippagunta, H. G. Brittain and D. J. W. Grant, *Advanced Drug Delivery Reviews*, 2001, **48**, 3-26.
26. R. K. Khankari and D. J. W. Grant, *Thermochimica Acta*, 1995, **248**, 61-79.
27. A. I. Wertheimer and A. Morrison, *Pharmacology & Therapeutics*, 2002, **27**, 44-49.
28. F. Simon, *Nature Reviews Drug Discovery*, 2006, **5**, 881-883.
29. D. Desai, J. Wang, H. Wen, X. Li and P. Timmins, *Pharmaceutical development and technology*, 2013, **18**, 1265-1276.
30. C. Almansa, R. Mercè, N. Tesson, J. Farran, J. Tomàs and C. R. Plata-Salamán, *Crystal Growth & Design*, 2017, **17**, 1884-1892.
31. S. Aitipamula, P. S. Chow and R. B. H. Tan, *CrystEngComm*, 2009, **11**, 1823-1827.
32. P. Grobelny, A. Mukherjee and G. R. Desiraju, *CrystEngComm*, 2011, **13**, 4358-4364.
33. O. D. Putra, T. Furuishi, E. Yonemochi, K. Terada and H. Uekusa, *Crystal Growth & Design*, 2016, **16**, 3577-3581.
34. J.-R. Wang, Q. Yu, W. Dai and X. Mei, *Chemical Communications*, 2016, **52**, 3572-3575.
35. S. P. Gopi, S. Ganguly and G. R. Desiraju, *Molecular pharmaceutics*, 2016, **13**, 3590-3594.
36. D. J. Berry and J. W. Steed, *Advanced Drug Delivery Reviews*, 2017, **117**, 3-24

37. J. W. Steed, D. R. Turner and K. Wallace, *Core Concepts in Supramolecular Chemistry and Nanochemistry*, Wiley, 2007.
38. L. Pauling, *Journal of the American Chemical Society*, 1935, **57**, 2680-2684.
39. L. Pauling, *CorneUUniv. Press, Ithsea, NY*, 1939, 131.
40. E. Arunan, R. Desiraju Gautam, A. Klein Roger, J. Sadlej, S. Scheiner, I. Alkorta, C. Clary David, H. Crabtree Robert, J. Dannenberg Joseph, P. Hobza, G. Kjaergaard Henrik, C. Legon Anthony, B. Mennucci and J. Nesbitt David, *Pure Appl. Chem*, 2011, **83**, 1619.
41. A. I. Kitaĭgorodskiĭ, *Molecular crystals and molecules*, Academic Press, 1973.
42. A. Mukherjee, *Crystal Growth & Design*, 2015, **15**, 3076-3085.
43. G. R. Desiraju, *Angewandte Chemie International Edition in English*, 1995, **34**, 2311-2327.
44. B. Swapna, D. Maddileti and A. Nangia, *Crystal Growth & Design*, 2014, **14**, 5991-6005.
45. P. Vishweshwar, J. A. McMahon, M. L. Peterson, M. B. Hickey, T. R. Shattock and M. J. Zaworotko, *Chemical Communications*, 2005, 4601-4603.
46. D. P. McNamara, S. L. Childs, J. Giordano, A. Iarriccio, J. Cassidy, M. S. Shet, R. Mannion, E. O'Donnell and A. Park, *Pharmaceutical research*, 2006, **23**, 1888-1897.
47. J. W. Steed and P. A. Gale, *Supramolecular Chemistry, 8 Volume Set: From Molecules to Nanomaterials*, Wiley, 2012.
48. O. Almarsson and M. J. Zaworotko, *Chemical Communications*, 2004, 1889-1896.
49. P. H. Stahl and C. G. Wermuth, *Handbook of Pharmaceutical Salts Properties, Selection, and Use*, Wiley, 2008.
50. A. A. Noyes and W. R. Whitney, *Journal of the American Chemical Society*, 1897, **19**, 930-934.
51. IUPAC. Compendium of Chemical Terminology, *2nd ed. (the "Gold Book")*. Compiled by A. D. McNaught and A. Wilkinson. Blackwell Scientific Publications, Oxford (1997). XML on-line corrected version: http://goldbook.iupac.org (2006-) created by M. Nic, J. Jirat, B. Kosata; updates compiled by A. Jenkins. ISBN 0-9678550-9-8. https://doi.org/10.1351/goldbook.
52. M. Stuart and K. Box, *Analytical Chemistry*, 2005, **77**, 983-990.
53. G. L. Amidon, H. Lennernäs, V. P. Shah and J. R. Crison, *Pharmaceutical Research*, 1995, **12**, 413-420.
54. A. M. Thayer, *Chemical & Engineering News Archive*, 2010, **88**, 13-18.
55. S. Kalepu and V. Nekkanti, *Acta Pharmaceutica Sinica. B*, 2015, **5**, 442-453.
56. A. D. McNaught, *Compendium of chemical terminology*, Blackwell Science Oxford, 1997.
57. M. Faraday, *Chemical manipulation: being instructions to students in chemistry, on the methods of performing experiments of demonstration or of research, with accuracy and success*, Murray, 1830.
58. L. Takacs, *Journal of Thermal Analysis and Calorimetry*, 2007, **90**, 81-84.
59. A. Delori, T. Friščić and W. Jones, *CrystEngComm*, 2012, **14**, 2350-2362.
60. A. V. Trask and W. Jones, in *Organic Solid State Reactions: -/-*, ed. F. Toda, Springer Berlin Heidelberg, Berlin, Heidelberg, 2005, pp. 41-70.
61. T. Friščić, A. V. Trask, W. Jones and W. Motherwell, *Angewandte Chemie*, 2006, **118**, 7708-7712.
62. D.-K. Bucar, G. M. Day, I. Halasz, G. G. Z. Zhang, J. R. G. Sander, D. G. Reid, L. R. MacGillivray, M. J. Duer and W. Jones, *Chemical Science*, 2013, **4**, 4417-4425.
63. N. Shan, F. Toda and W. Jones, *Chemical Communications*, 2002, 2372-2373.
64. S. M. Paul, D. S. Mytelka, C. T. Dunwiddie, C. C. Persinger, B. H. Munos, S. R. Lindborg and A. L. Schacht, *Nature reviews. Drug discovery*, 2010, **9**, 203.
65. H. van de Waterbeemd, D. A. Smith, K. Beaumont and D. K. Walker, *Journal of Medicinal Chemistry*, 2001, **44**, 1313-1333.
66. K. R. Seddon and M. Zaworotko, *Crystal Engineering: The Design and Application of Functional Solids*, Springer, 1999.
67. S. Datta and D. J. Grant, *Nature reviews. Drug discovery*, 2004, **3**, 42.

68. D. Braga and F. Grepioni, *Making Crystals by Design: Methods, Techniques and Applications*, Wiley, 2007.
69. F. Spinelli, E. Dichiarante, M. Curzi, S. L. Giaffreda, M. R. Chierotti, R. Gobetto, F. Rossi, L. Chelazzi, D. Braga and F. Grepioni, *Crystal Growth & Design*, 2017, **17**, 4270-4279.
70. J.-M. Chen, S. Li and T.-B. Lu, *Crystal Growth & Design*, 2014, **14**, 6399-6408.
71. D. Stepanovs, M. Jure, M. Gosteva, J. Popelis, G. Kiselovs and A. Mishnev, *CrystEngComm*, 2016, **18**, 1235-1241.
72. E. Robertson, in *xPharm: The Comprehensive Pharmacology Reference*, Elsevier, New York, 2007, pp. 1-7.
73. L. Erdmann, B. Macedo and K. Uhrich, *Biomaterials*, 2000, **21**, 2507-2512.
74. K. Whitaker-Brothers and K. Uhrich, *Journal of biomedical materials research Part A*, 2006, **76**, 470-479.
75. S. Tang, S. M. June, B. A. Howell and M. Chai, *Tetrahedron letters*, 2006, **47**, 7671-7675.
76. J. Ji, S. Hao, D. Wu, R. Huang and Y. Xu, *Carbohydrate polymers*, 2011, **85**, 803-808.
77. M. Meng, Y. Feng, W. Guan, Y. Liu, Y. Xi and Y. Yan, *Journal of Industrial and Engineering Chemistry*, 2014, **20**, 3975-3983.
78. P. J. Nowatzki, R. R. Koepsel, P. Stoodley, K. Min, A. Harper, H. Murata, J. Donfack, E. R. Hortelano, G. D. Ehrlich and A. J. Russell, *Acta biomaterialia*, 2012, **8**, 1869-1880.
79. R. C. Mundargi, V. R. Babu, V. Rangaswamy, P. Patel and T. M. Aminabhavi, *Journal of Controlled Release*, 2008, **125**, 193-209.
80. H. Matsuda, K. Kaburagi, S. Matsumoto, K. Kurihara, K. Tochigi and K. Tomono, *Journal of Chemical & Engineering Data*, 2009, **54**, 480-484.
81. J. R. Vane, *Nat New Biol*, 1971, **231**, 232-235.
82. D. Pawar, S. Shahani and S. Maroli, *Hong Kong Med J*, 1998, **4**, 415-418.
83. J. Achan, A. O. Talisuna, A. Erhart, A. Yeka, J. K. Tibenderana, F. N. Baliraine, P. J. Rosenthal and U. D'Alessandro, *Malaria Journal*, 2011, **10**, 144-144.
84. WHO, WHO model list of essential medicines: 18th list, April 2013. **2013**
85. Provisional BCS Classification, http://www.tsrlinc.net/search.cfm, (accessed 10/01, 2017).
86. N. A. Kasim, M. Whitehouse, C. Ramachandran, M. Bermejo, H. Lennernas, A. S. Hussain, H. E. Junginger, S. A. Stavchansky, K. K. Midha, V. P. Shah and G. L. Amidon, *Mol Pharm*, 2004, **1**, 85-96.
87. WHO, *Transactions of the Royal Society of Tropical Medicine and Hygiene*, 2000, **94**, 1-90.
88. K. K. Karlsson, U. Hellgren, G. Alván and L. Rombo, *Transactions of the Royal Society of Tropical Medicine and Hygiene*, 1990, **84**, 765-767.

Chapter 2

Experimental methods and materials

2.1 Experiment design

Coformer selection for co-crystallisation experiments was based on visual inspection of the possible hydrogen bond acceptors and donors present in the API structures. Since the targeted APIs (aspirin and salicylic acid) are carboxylic acids, the cinchona alkaloids were selected because of their amine and hydroxyl functionality, of which both are exceptionally good hydrogen bond acceptors. A Cambridge Structural Database (CSD)[1] search was carried out to determine the frequency of occurrence of the predicted interaction between the API and the coformer.

To speculate the possible outcome of the co-crystallisation, the quantitated pK_a rule by Cruz-Cabeza was employed.[2] The quantitated pK_a rule states that when the pK_a difference (ΔpK_a = pK_a [protonated base] – pK_a [acid]) between the co-crystallizing acid and base is greater than 4 a salt is usually formed. When the ΔpK_a is below -1, a cocrystal is formed. In the ΔpK_a region of -1 to 4 either a salt or a cocrystal may be formed.

2.2 Compounds

2.2.1 Pharmaceutical compounds

Aspirin and salicylic acid were purchased from Sigma-Aldrich and Merck & Co. The molecular line diagrams of the two APIs are illustrated in Figure 2.1; and their physical properties, chemical formulae and molecular weights are given in Table 2.1.

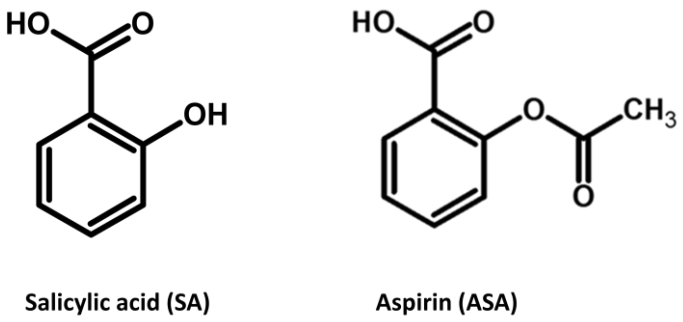

Figure 2.1 Structural line diagrams of the pharmaceutical compounds.

Table 2.1 Physical properties and formulas of the host compounds. (pK_a calculated using Marvin)[3]

API	Formula	Mr (g.mol^{-1})	MP (°C)	pK_a
Aspirin (ASA)	$C_8H_8O_4$	180.16	140	3.41
Salicylic acid (SA)	$C_7H_6O_3$	138.12	159	2.79

2.2.2 Coformers

The coformers (cinchona alkaloids) were purchased from Sigma-Aldrich and Merck & Co. The structures of the coformers are illustrated in Figure 2.2 with their line diagrams and their physical properties, chemical formulae and molecular weights are given in Table 2.2. The melting points summarised in Table 2.2 are literature values. The Cinchona alkaloids are naturally occurring compounds that are extracted from the bark of *Cinchona ledgeriana* trees.[4] The most significant use of cinchona alkaloids is to treat malaria[5] and cardiac arrhythmias.[6] In addition, They have been used as flavours in food and drinks,[7] as homogeneous and heterogeneous catalysts[8-11] and as chiral resolving agents.[12] Evidently the cinchona alkaloids have been utilised in a number of applications, which makes them suitable multicomponent crystal coformers.

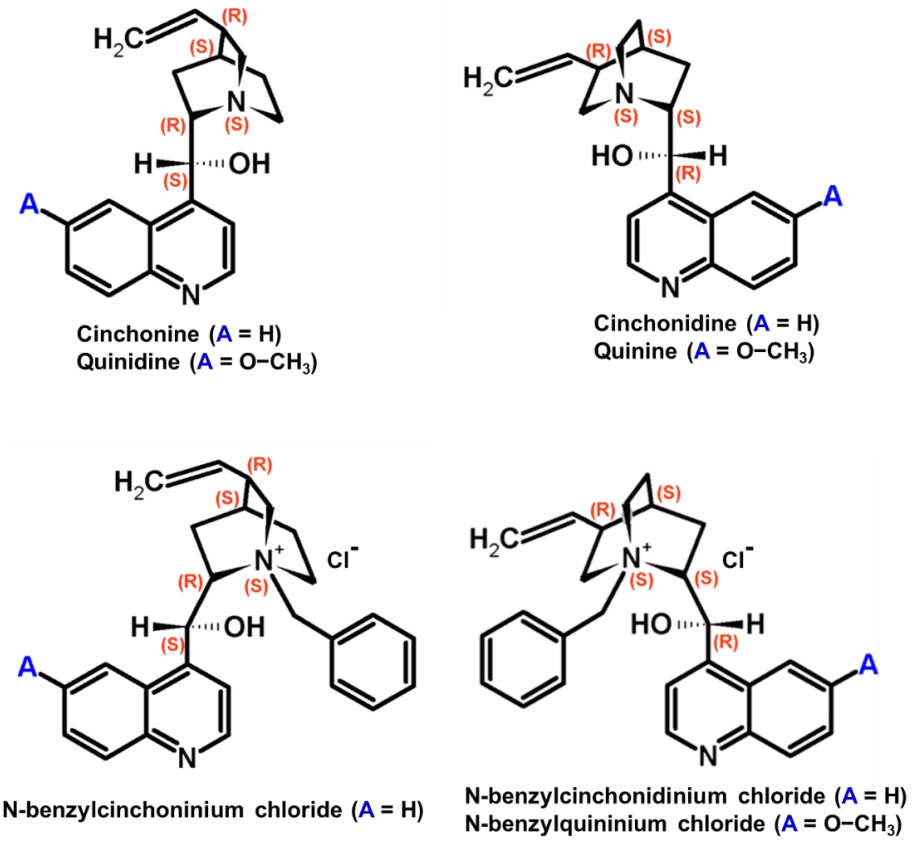

Figure 2.2 Chemical structures of the cinchona alkaloids, highlighting the stereo centres.

Table 2.2 Physical properties and formulas of the guest compounds. (pK_a calculated using Marvin)[3]

Coformer	Formula	Mr (g.mol^{-1})	MP (^{o}C)	pK_{a1}	pK_{a2}
Quinine (QUIN)	$C_{20}H_{24}N_2O_2$	324.4	177	9.69	6.19
Quinidine (QUID)	$C_{20}H_{24}N_2O_2$	324.4	168-172	9.69	6.19
Cinchonine (CINC)	$C_{19}H_{22}N_2O$	294.4	264	9.69	6.28
Cinchonidine (CIND)	$C_{19}H_{22}N_2O$	294.4	205-210	9.69	6.28
N-benzylquininium chloride (NBQUIN)	$[C_{27}H_{31}N_2O]^+$ Cl^-	451.0	200-205	5.83	
N-benzylcinchoninium chloride (NBCINC)	$[C_{26}H_{29}N_2O]^+$ Cl^-	420.9	256	5.88	
N-benzylcinchonidinium chloride (NBCIND)	$[C_{26}H_{29}N_2O]^+$ Cl^-	465.5	190	5.88	

2.3 Crystal formation

Solvent evaporation method was used to grow single crystals. The principle behind the solvent evaporation method is to achieve crystal growth through nucleation. The process of nucleation is only possible if the free energy used to form a new solid-liquid interface is recovered through the formation of the new bulk crystalline material. Once nucleation has occurred and has produced large enough clusters of molecules, crystal growth proceeds. The crystals formed through this method are usually the thermodynamically favoured product.

Multicomponent crystals were obtained by dissolving a 1:1 mixture aspirin or salicylic acid and the base in a solvent by stirring and heating on a hot plate until clear; the solutions were then left to evaporate at room temperature. The solvents with differing polarity indices and dielectric constants employed are summarised in Table 2.3.

Table 2.3 Polarity index and dielectric constant of solvents.[13]

Solvent	Polarity index (P')	Dielectric constant (ε)
Acetone	5.1	20.7
Acetonitrile	5.8	37.5
Butyl acetate	4.0	5.1
Ethanol	5.2	24.5
Ethyl acetate	4.4	6.02
Isopropanol	3.9	17.9
Methanol	5.1	32.7
Water	9.0	80.1

Another method of crystal formation, which was employed in this study, is liquid assisted grinding (LAG). As highlighted earlier, this method is usually employed because of the significant improvements in the kinetics of cocrystal formation achieved when a small quantity of the solvent is added when grinding the API and the coformer. In addition, it is also used because it is a green chemistry technique. The one-to-one mixtures of aspirin or salicylic acid and the coformer were ground using a ball mill grinder, designed in house.

2.4 Thermal analysis

Thermal analysis methods are defined as techniques in which a specific property of a sample is investigated under a temperature program (cooling or heating).[14] The results are obtained in the form of a thermal analysis curves, and the curve is usually named after the specific method. Two thermal analysis methods were used, namely; thermogravimetric analysis (TGA) and differential scanning calorimetry (DSC).

2.4.1 Differential scanning calorimetry (DSC)

During a DSC measurement the difference in the heat flow through the sample and the reference is measured against time or temperature.[15] The sample and the reference are held in a furnace where there are two identical sensors used, one to monitor the sample and the other the reference. The signal output is dependent on the difference in the response of the two sensors.

A Perkin Elmer Pyris DSC 6000 heat flux differential scanning calorimeter was used in the screening of the new solid forms. DSC results are influenced by the sample size, purge gas flow rate and sample heating rate.[15] Therefore, samples were always dried on filter paper and ground before analysis was conducted and a mass of 2-3 mg was used. In addition, sample heating rate and purge gas flow rate were kept constant throughout all experiments. The instrument was operated using nitrogen as a purge gas at a flow rate 20 ml min^{-1}. The temperature program was set from 30 ^{o}C to 300 ^{o}C at a ramp rate of 10 ^{o}C min^{-1}.

2.4.2 Thermogravimetric analysis (TGA)

Thermogravimetric analysis is a technique that has been defined as the measurement of mass change of a sample, as a function of time or temperature, in a temperature- and atmosphere-controlled environment.[16] The changes in the sample mass are monitored using a thermobalance. The components of a thermobalance include: a microbalance with a furnace, a temperature programmer and a computer.[17] These components collectively allow for the simultaneous monitoring of the mass, and heating or cooling in a controlled manner. The results are obtained in the form of thermogravimetric curves, which are also referred to as mass loss curves. Since the response measured in TGA is due to a mass change, it makes this technique only suitable for analysis of reactions that are accompanied by mass change, such as evaporation, decomposition, gas absorption, desorption and desolvation.[17]

For this project, TGA was used to prove the presence or absence of solvent inclusion in the obtained multicomponent crystals. A Perkin Elmer Pyris 6 thermogravimetric analyser was used. Each sample was dried on a filter paper and a sample mass of 3-5 mg was used for each analysis. The instrument was operated using nitrogen as a purge gas at a flow rate 20 ml min^{-1}. The temperature program was set from 30 ^{o}C to 350 ^{o}C at a ramp rate of 10 $^{o}C\ min^{-1}$. As in DSC, TGA results are influenced by the sample size, purge gas flow rate and sample heating rate; samples were always ground before analysis was conducted. In addition, sample heating rate and purge gas flow rate were kept constant throughout all experiments.

2.5 Single crystal X-ray diffraction

Single crystal X-ray diffraction (SCXRD) is a non-destructive analytical technique which provides detailed information about the internal lattice of crystalline substances, including unit cell dimensions, bond lengths, bond angles, and details of site-ordering. Structure determination using SCXRD is based on the fact that X-ray wavelengths are in the same order of magnitude as the interatomic distances in crystalline material;[18] therefore, because of this interaction with the crystalline material, X-ray diffraction results can be translated into a crystal structure.

Diffraction data for all multicomponent crystals was collected on a Bruker APEX II diffractometer using graphite-monochromated MoK$_\alpha$ radiation (λ = 0.71073 Å), and at low temperatures of 173 K achieved by using an Oxford Cryostream 700 cooler. SAINT was used for unit cell refinement and data reduction. The Lorentz factor, a measure of the time that a reciprocal lattice point remains on the reflection sphere during measurement, was corrected using SADABS.[19] XPREP[20] was used to determine the unit cells from the cell parameters specified by SAINT[21], and from the collected X-ray intensity data. X-seed[22] was used as the graphical user interface to run the following programs: SHELXS-97,[23] SHELXL,[24] LAZY PULVERIX,[25] POV-Ray,[26] LAYER.[27]

Structures were solved by direct methods using SHELXS-97. The crystal structure obtained from SHELXS is an approximate or partial structure. An accurate and complete structure is then obtained through refinement. Structure refinement was carried out using SHELXL by employing full matrix least squares refinement, which is the minimization of the sum of the squares of the difference (D) between the observed (F_o) and calculated (F_c) intensities (equation 2).

$$D = \sum w\,(F_o^2 - kF_c^2)^2 \qquad \text{(eq. 2)}$$

The accuracy of the model is monitored through the residual index *R*. The agreement of the measured structure factors (F_o) to the calculated structure factors (F_c) for the refinement against *F* is expressed as the residual index R_1 (equation 3). The agreement between structure factors for the refinement against F^2 is given by the residual index R_2 (equation 4).

$$R_1 = \frac{\sum \| F_o | - | F_c \|}{\sum | F_o |} \qquad \text{(eq. 3)}$$

$$wR_2 = \sqrt{\frac{\sum w\,(F_o^2 - kF_c^2)^2}{\sum w\,(F_o^2)^2}} \qquad \text{(eq. 4)}$$

F_o and F_c are the observed and calculated structure factors respectively, and *w* is the weighting scheme. The weighting scheme is determined using equation 5 and was refined for each structure at the end of the structure refinement where P is given by equation 6.

$$w = \frac{1}{\sigma^2(F_o^2) + (aP)^2 + bP} \qquad \text{(eq. 5)}$$

$$P = \frac{\max(0, F_o^2) + 2F_c^2}{3} \qquad \text{(eq. 6)}$$

The extent of agreement between the model based on refinement against F^2 and the structure based on refinement against F is given as the Goodness-of-fit (S); (equation 7), where n is the number of reflections and p is the total number of parameters refined.

$$S = \left(\frac{\sum w\,(F_o^2 - kF_c^2)^2}{n - p}\right)^{\frac{1}{2}} \qquad \text{(eq. 7)}$$

The hydrogen atoms bound to carbon atoms were placed at idealized positions and refined as riding atoms with U_{iso} (H) = 1.2 U_{eq} (Ar-H, CH_2) or 1.5 U_{eq} (CH_3) of the atom to which the H is bound. Hydrogen atoms bonded to the carboxylic acid, amine or hydroxyl groups were located on the difference electron density map and their coordinates refined freely but their isotropic displacement parameters were fixed (U_{iso} (H) = 1.2 U_{eq}(O) or U_{eq}(N)) if it was necessary.

2.6 Powder X-ray diffraction

Powder X-ray diffraction (PXRD) has the same principle as single crystal diffraction, but PXRD is a much more convenient and quicker method for obtaining diffraction data. The results are obtained in the form of peaks which represent the unique 2D diffraction pattern of the sample; therefore PXRD can be used as a fingerprint technique for the identification of materials.[18]

A monochromatic X-ray beam is shone onto the PXRD sample, which is usually composed of randomly oriented microcrystals. Therefore, for any set of planes there are bound to be some crystals oriented such that the Bragg condition is met, which will give rise to diffraction effects that satisfy they Bragg equation (equation 8):

$n\lambda=2d\sin\theta$ where n = a positive integer (eq. 8)

d = distance between atomic layers

λ = wavelength of the incident X-ray beam

θ = glancing angle

For our purposes, PXRD was used to prove that the results obtained by SCXRD are representative of the bulk material obtained from crystallization. The Bruker D2 Phaser diffractometer equipped with a graphite-monochromated Cu Kα radiation (λ= 1.5418 Å) was used to collect diffraction data for all materials at room temperature.

2.7 Solubility and dissolution

Both solubility and rate of dissolution require the measurement of concentration; equilibrium concentration for solubility and change in concentration with time for dissolution. High performance liquid chromatography was used to measure the rate of change of concentration of the APIs (salicylic acid and acetylsalicylic acid) from the multicomponent crystals in water.

The rate of dissolution of the multicomponent crystals of salicylic acid was determined by stirring an equal mass of each respective multicomponent crystal in a constant volume of water, and samples were drawn at set time intervals. HPLC assay of the samples was carried out on an Agilent 6230 liquid chromatographic system coupled to a mass spectrometer (LC-MS). The LC-MS was equipped with a binary solvent pump, an autosampler injector, diode array detector (DAD) and a time of flight (TOF) mass spectrometer. The analysis was performed using a reversed-phase column (C8, 5 µm) and an isocratic mobile phase (70:30, methanol-water, v/v, with 0.1% formic acid). The flow rate of the mobile phase was 0.3 ml min^{-1}. The MS was operated in the negative ion mode at 3000 eV and 500 ^{o}C.

2.8 Analysis programs

Cambridge Structural Database (CSD) is a collection of over 800 000 crystal structures solved by X-ray or neutron diffraction techniques. This database contains crystal structures of all organic and metal-organic small-molecules that have been published, and it summarises the chemical, experimental, crystallographic, and bibliographic information of these structures.[28]

ConQuest is an interface used for searching and retrieving data from the Cambridge Structural Database. Its main function is to build a search query. In addition, many search queries built from different search parameters can be combined to search for structures with multiple variables.[29]

Siemens Area Detector Absorption Corrections (SADABS) is an application in the APEX suite used to scale and correct data for absorption collected on a Bruker AXS area detector.[19] The program is designed to exploit data redundancy, corrects for errors resulting from the variation in the volume of the crystal, absorption by the crystal support and crystal decay during the measurement.

XPREP: This program determines the space group, reads the raw data file (.raw) and the parameter file (.p4p) written by the diffractometer control program, also generates the instruction file (.ins) and reflection data file (.hkl).

X-Seed[22] is a graphical user interface employed to run the SHELX suit, LAZY PULVERIX, LAYER and SECTION. In addition, X-seed is used to generate high resolution molecular packing images with the aid of POV-Ray.

LAYER is a Microsoft windows based program. It displays simulated precession photographs of the reciprocal lattice levels using the intensity data.[27] The program was utilized to test systematic absences and space group symmetry.

LAZY PULVERIX is a program that calculates theoretical X-ray powder diffraction patterns from single crystal data.[25] X-ray powder patterns calculated using LAZY PULVERIX were compared to experimental powder patterns from crystallization during bulk analysis.

POV-Ray is an acronym for Persistence of Vision Ray-tracer and is designed to produce high quality computer graphics. POV-Ray models 3D, photo realistic images using a method called ray-tracing. It translates the file describing the object and scene lighting into an image. This program was used to generate crystal packing diagrams.[26]

POV-Label is a component of X-Seed. The program enables the user to control the atom labels on an image rendered using POV-Ray.

Mercury offers a comprehensive range of tools for 3D structure visualization and the analysis of crystal packing.[29] Mercury can load structural data from a variety of formats which includes structures from the CSD or to read crystal structure in other common formats such as MOL2, PDB, CIF and MOL files. Mercury has many options to aid the analysis of crystal structures. The functions which are present include generation of packing diagrams, least-squares and simulated diffraction pattern calculation from displayed crystal structure; the ability to measure distances, angles and torsion angles. Mercury is also able to locate and display hydrogen bonds, short non-bonded contacts and user-specified contacts.[30]

Marvin[3] is a software used to calculate structure properties**.** Calculator Plugins were used for structure property prediction and calculation. The pKa prediction is done based on the partial charge distribution calculated for the atoms in the molecule and this method provides an efficient and robust way to locate the most acidic and basic sites.

Crystal Explorer[31] is a program used for the calculation and display of Hirshfeld surfaces and 2D fingerprint plots and allows the visualization and analysis of intermolecular interactions of molecules in a crystal structure. The Hirshfeld surface originated from trying to define the space occupied by a molecule in a crystal structure for the purpose of partioning the crystal electron density into molecular fragments.[32,33] Hirshfeld surfaces were named after F.L Hirshfeld who, in his work, gave a scheme for describing atoms in a molecule[34] by defining a weight function, $w_a(\mathrm{r})$, for each atom in a molecule as:

$$w_a(\mathrm{r}) = \rho_i^{at}(r) \,/ \sum_{i\epsilon\, molecule} \rho_i^{at}(r) \qquad (\mathrm{eq.}\,9)$$

where $\rho_i^{at}(r)$ are spherically averaged electron densities of the various atoms. Based on Hirshfeld's idea, Speakman and Byrom[35] adopted and extended this principle to define a weight function $(w_A(\mathrm{r}))$ for a molecule in a crystal as:

$$w_A(\mathrm{r}) = \sum_{i\epsilon\, molecule\ A} \rho_i^{at}(r) \,/ \sum_{i\epsilon\, crystal} \rho_i^{at}(r) \qquad (\mathrm{eq.}\,10)$$

$$= \rho_{promolecule}(r) \,/\, \rho_{procrystal}(r)$$

where $\rho_i^{at}(r)$ is a spherical atomic electron distribution located at the ith nucleus. The Hirshfeld surface is defined by an isosurface $w_A(\mathrm{r})$ of 0.5, and describes the volume of space

where the promolecule electron density exceeds that of all neighbouring molecules. The distance from the Hirshfeld surface to the nearest atom outside the surface is denoted as d_e and the distance from the surface to the nearest atom inside the surface as d_i. These distances can be mapped onto the Hirshfeld surface to provide a three-dimensional image of the intermolecular interactions in a crystal structure, however the use of d_i and d_e has limitations. Thus, a normalised contact distance, d_{norm}, is used to overcome these limitations.[36] The contact distance is normalised according to the formula:

$$d_{\mathrm{norm}} = \frac{d_i - r_i^{vdW}}{r_i^{vdW}} + \frac{d_e - r_e^{vdW}}{r_e^{vdW}} \qquad (\mathrm{eq.}\,11)$$

where r^{vdW} is the van der Waals radius of the specified atom inside or outside the surface, and d_i and d_e are the distances from the surface to the nearest atom inside and outside respectively. Since its inception, d_{norm} has been applied to investigate the intermolecular interactions in a crystal structure.[37-40] This is achieved by representing the 3D Hirshfield surface as 2D fingerprint plots, which give a breakdown of the intermolecular interactions as well as their contributions to the total Hirshfeld surface. The analysis of the shape of the 2D plots, in conjunction with the percentage contributions of the intermolecular interaction, have been employed to understand crystal packing.[41, 42] Here we apply the same principle to correlate the observed physical properties of the multicomponent crystals to the intermolecular interactions in the crystal structure.

2.9 References

1. F. Allen, *Acta Crystallographica Section B*, 2002, **58**, 380-388.
2. A. J. Cruz-Cabeza, *CrystEngComm*, 2012, **14**, 6362-6365.
3. ChemAxon, *Marvin 16.4.25*, 2016.
4. C. E. Song, *Cinchona Alkaloids in Synthesis and Catalysis: Ligands, Immobilization and Organocatalysis*, Wiley, 2009.
5. T. S. Kaufman and E. A. Rúveda, *Angewandte Chemie International Edition*, 2005, **44**, 854-885.
6. N. J. White, *The Lancet infectious diseases*, 2007, **7**, 549-558.
7. C. G. Meyer, F. Marks and J. May, *Tropical Medicine & International Health*, 2004, **9**, 1239-1240.
8. H. Wynberg, *Topics in stereochemistry*, 1986, **16**, 87-129.
9. K. Kacprzak and J. Gawroński, *Synthesis*, 2001, **2001**, 0961-0998.
10. T. Mallat, E. Orglmeister and A. Baiker, *Chemical Reviews*, 2007, **107**, 4863-4890.
11. Z. Ma and B. Moulton, *Crystal Growth & Design*, 2007, **7**, 196-198.
12. M. Laemmerhofer and W. Lindner, *Advances in chromatography*, 2007, **46**, 1-107.
13. A. J. Gordon and R. A. Ford, *The Chemist's Companion: A Handbook of Practical Data, Techniques, and References*, J. Wiley and sons, 1972.
14. T. Lever, P. Haines, J. Rouquerol, E. L. Charsley, P. Van Eckeren and D. J. Burlett, *Pure & Applied Chemistry*, 2014, **86**, 545-553.
15. M. Brown, *Introduction to Thermal Analysis*, Kluwer Academic Publishers, Grahamstown, 2001.
16. P. Haines, *Thermal Methods of Analysis* Blackie Academic & Professionals, New York, 1995.
17. M. E. Brown, *Introduction to Thermal Analysis: Techniques and Applications*, Springer Netherlands, 2006.
18. M. A. Wahab, *Essentials of Crystallography*, Narosa Publishing House, New Delhi, 2nd edn., 2014.
19. G. M. Sheldrick, *University of Göttingen, Germany*, 1996.
20. G. M. Sheldrick, *Bruker-Nonius AXS, Madison, Wisconsin*, 2003.
21. Bruker, *Bruker AXS Inc, Madison, Wisconsin, USA*, 2004.
22. L. J. Barbour, *Journal of Supramolecular Chemistry*, 2001, **1**, 189-191.
23. G. M. Sheldrick, *SHELXS-97*, 1997.
24. G. M. Sheldrick, *Acta Crystallographica Section C*, 2015, **71**, 3-8.
25. K. Yvon, W. Jeitschko and E. Parthe, *Journal of Applied Crystallography*, 1977, **10**, 73-74.
26. C. Cason, *POV-RAY*, 2004.
27. L. Barbour, *Journal of Applied Crystallography*, 1999, **32**, 351-352.
28. C. R. Groom, I. J. Bruno, M. P. Lightfoot and S. C. Ward, *Acta Crystallographica Section B*, 2016, **72**, 171-179.
29. I. J. Bruno, J. C. Cole, P. R. Edgington, M. Kessler, C. F. Macrae, P. McCabe, J. Pearson and R. Taylor, *Acta Crystallographica Section B*, 2002, **58**, 389-397.
30. C. F. Macrae, I. J. Bruno, J. A. Chisholm, P. R. Edgington, P. McCabe, E. Pidcock, L. Rodriguez-Monge, R. Taylor, J. v. Streek and P. A. Wood, *Journal of Applied Crystallography*, 2008, **41**, 466-470.
31. S. Wolff, D. Grimwood, J. McKinnon, M. Turner, D. Jayatilaka and M. Spackman, *University of Western Australia, Perth, Australia*, 2013.
32. M. A. Spackman and D. Jayatilaka, *CrystEngComm*, 2009, **11**, 19-32.
33. J. J. McKinnon, A. S. Mitchell and M. A. Spackman, *Chemistry-A European Journal*, 1998, **4**, 2136-2141.
34. F. L. Hirshfeld, *Theoretica chimica acta*, 1977, **44**, 129-138.
35. M. A. Spackman and P. G. Byrom, *Chemical Physics Letters*, 1997, **267**, 215-220.

36. J. J. McKinnon, D. Jayatilaka and M. A. Spackman, *Chemical Communications*, 2007, 3814-3816.
37. Y.-H. Luo and B.-W. Sun, *Crystal Growth & Design*, 2013, **13**, 2098-2106.
38. P. A. Wood, J. J. McKinnon, S. Parsons, E. Pidcock and M. A. Spackman, *CrystEngComm*, 2008, **10**, 368-376.
39. J. J. McKinnon, A. S. Mitchell and M. A. Spackman, *Chemical Communications*, 1998, 2071-2072.
40. E. Batisai, A. Ayamine, O. E. Y. Kilinkissa and N. B. Báthori, *CrystEngComm*, 2014, **16**, 9992-9998.
41. N. B. Báthori, L. R. Nassimbeni and C. L. Oliver, *Chemical Communications*, 2011, **47**, 2670-2672.
42. N. B. Báthori and O. E. Y. Kilinkissa, *CrystEngComm*, 2015, **17**, 8264-8272.

Chapter 3

Multicomponent crystals of salicylic acid: Controlled release of a highly soluble drug

3. Multicomponent crystals of salicylic acid (SA)

Seven multicomponent crystals of salicylic acid were formed with: quinidine [$QUID^+$][SA^-], quinine [$QUIN^+$][SA^-], cinchonine [$CINC^+$][SA^-], cinchonidine [$CIND^+$][SA^-], N-benzylquininium chloride [$NBQUIN^+$][SA^-], N-benzylcinchoninium chloride [$NBCINC^+$][SA^-], and N-benzylcinchonidinium chloride [$NBCIND^+$][SA^-].

To speculate the possible solid form outcome from the co-crystallisation, the quantitated pK_a rule by Cruz-Cabeza was employed.[1] The calculated pK_a difference between the cocrystallizing acid and bases (ΔpK_a = pK_a [protonated base] – pK_a [acid]) is greater than 4, thus we expected salts to be formed in all cases.

In all crystal structures obtained, the measured C-O bond lengths of the carboxylate group are almost equal (Table 3.1), indicating deprotonation. Simultaneously, a residual density peak was observed on N11 of the QUIN, QUID, CINC and CIND molecules, and was subsequently assigned as the transferred hydrogen atom. Therefore, all the multicomponent crystal systems were classified as salts.

Table 3.1 Measured C-O bond lengths of the carboxylate group.

	C46-047 (Å)	C46-048 (Å)	C46B-048B (Å)	C46B-048B (Å)
[$CINC^+$][SA^-]	1.253	1.266		
[$CIND^+$][SA^-]	1.252	1.272	1.251	1.271
[$QUIN^+$][SA^-]	1.245	1.282	1.259	1.279
[$QUID^+$][SA^-]	1.262	1.243		
[$NBCINC^+$][SA^-]	1.241	1.263		
[$NBCIND^+$][SA^-]	1.251	1.249		
[$NBQUIN^+$][SA^-]	1.251	1.257		

3.1 Cinchona alkaloid salicylates

Formation of [$QUIN^+$][SA^-] was achieved from an equimolar mixture of the coformer and API in ethanol. On the other hand, [$CINC^+$][SA^-] and [$QUID^+$][SA^-] were obtained from 1:1 solution of butyl acetate and ethanol, and [$CIND^+$][SA^-] from a 1:1 solution of butyl acetate and water. The crystallographic data and refinement parameters are summarised in Table 3.2.

Table 3.2 Crystallographic data for the unsubstituted cinchona alkaloid salicylate salts.

	[CINC$^+$][SA$^-$]	[CIND$^+$][SA$^-$]	[QUIN$^+$][SA$^-$]	[QUID$^+$][SA$^-$]
Formula	$C_{26}H_{28}N_2O_4$	$C_{26}H_{28}N_2O_4$	$C_{27}H_{30}N_2O_5$	$C_{27}H_{29}N_2O_5$
Mr (g.mol^{-1})	432.50	432.50	462.53	461.52
Crystal system	orthorhombic	monoclinic	monoclinic	orthorhombic
Space group	$P2_12_12$	$P2_1$	$C2$	$P2_12_12$
a/Å	29.020 (6)	6.4694 (7)	20.616 (4)	28.823 (3)
b/Å	7.3899 (15)	34.959 (4)	6.5926 (13)	7.4994 (7)
c/Å	10.474 (2)	10.2214 (11)	36.104 (7)	10.7876 (11)
α/°	90	90	90	90
β/°	90	104.996(2)	103.92(3)	90
γ/°	90	90	90	90
Volume/Å^3	2246.2 (8)	2233.0 (4)	4762.9 (17)	2331.8 (4)
Z	4	4	8	4
ρ (calc.)/ mg.m^{-3}	1.279	1.286	1.290	1.315
μ(MoKα)/ mm^{-1}	0.086	0.087	0.089	0.091
F(000)	920.0	920.0	1968.0	980.0
Crystal size (mm)	0.45×0.36×0.20	0.1×0.1×0.1	0.1×0.1×0.1	0.1×0.1×0.1
Temperature (K)	173 (2)	173 (2)	173 (2)	173 (2)
Radiation [Å]	0.71073	0.71073	0.71073	0.71073
Theta min-max [°]	1.944, 28.486	2.330, 28.433	1.743, 28.259	1.413, 28.354
Dataset (±h, ±k, ±l)	-38:38, -9:9,-14:14	-7:8, -46:46,-13:13	-27:24, -8:8,-47:47	-30:38, -10:7,-11:14
Final R indices [I>2.0 sigma (I)]	R1= 0.0433, wR2= 0.1082	R1= 0.0488, wR2= 0.1124	R1=0.0699, wR2=0.0901	R1= 0.0845, wR2= 0.2254
R indices (all data)	R1= 0.0524, wR2= 0.1144	R1= 0.0619, wR2= 0.1197	R1=0.0459, wR2=0.0901	R1= 0.1035, wR2= 0.2406
Tot., uniq. data, R (int)	5646, 4879, 0.0338	11128, 9249, 0.0294	11717, 8921, 0.0335	5826, 4551, 0.0248
N_{ref}, N_{par}	5646, 292	11128, 583	11717, 627	5826, 321
S	1.025	1.020	0.987	1.031
Max.and av. Shift/error	0.00, 0.00	0.00, 0.00	0.00, 0.00	0.00, 0.00
Min. and max. resd. dens. (Å)	-0.184, 0.486	-0.185, 0.259	-0.201, 0.188	-0.499, 0.824

3.1.1 Cinchoninium salicylate [CINC$^+$][SA$^-$]

The crystal structure of cinchoninium salicylate, [CINC$^+$][SA$^-$], was solved in the orthorhombic space group $P2_12_12$ (Z'=1). The asymmetric unit contains one cinchoninium ion and one salicylate ion held together by a N11-H11···O47 (2.66 Å, 175.2°) charge-assisted hydrogen bond. The labelling scheme and the interactions in the asymmetric unit are shown in Figure 3.1.

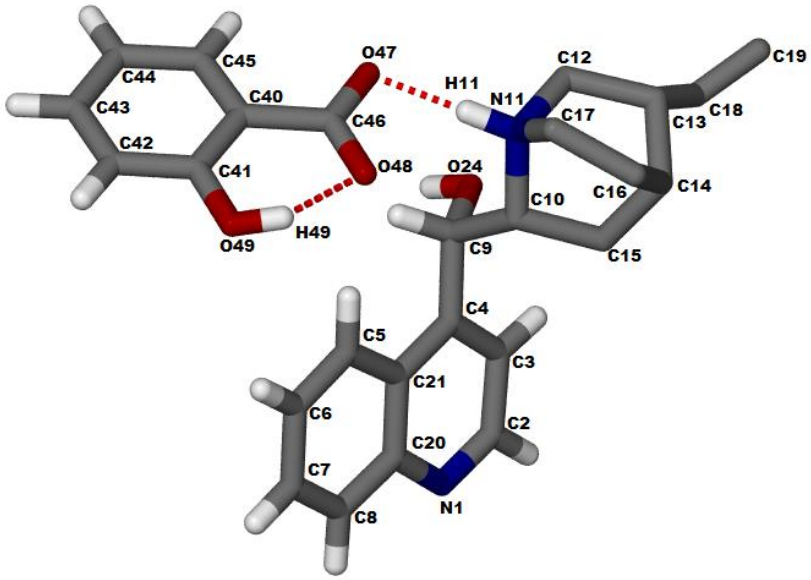

Figure 3.1 Asymmetric unit of [CINC$^+$][SA$^-$] with labels and the N$^+$-H···O$^-$ interaction between the cinchoninium and the salicylate ion (quinuclidine ring hydrogens are omitted for clarity).

The hydrogen bonding in the ion pair is described by the formation of N11-H11···O47 (2.66 Å, 175.2°), O24-H24···N1^i (2.96 Å, 158.4°, [-x, -y+2, z]) interactions (Table 3.3). Discrete four component assemblies are formed by two [CINC$^+$][SA$^-$] ion pairs related by a two-fold rotation axis via O24-H24···N1 (2.96 Å, 158.4°) H-bonds, that may be described by $R_2^2(14)$ graph set (Figure 3.2). The distance between the planes of the quinoline moieties in the ion pair dimers is 3.7 Å for the $\pi\cdots\pi$ stacking. The ion pair dimers adopt a brick layer packing (Figure 3.3a) and the salicylate ions sit in channels running down [010] (Figure 3.3b).

Table 3.3 Hydrogen bond and short contact metrics of [CINC$^+$][SA$^-$].

D-H···A	D-H (Å)	H···A (Å)	D···A (Å)	∠D-H···A (°)
N11-H11···O47	0.90	1.77	2.66	175.2
O24-H24···N1^{i}	0.84	2.16	2.96	158.4
O49-H49···O48	0.84	1.79	2.53	144.7
N11-H11···O48	0.90	2.49	3.08	123.0
C12-H12B···O24	0.99	2.28	2.99	127.8
C17-H17A···O48	0.99	2.58	3.23	123.0
C17-H17B···O47^{ii}	0.99	2.37	3.26	148.0
Symmetry codes	(i) [-x,-y+2,z] (ii) [-x+1/2,y-1/2,-z+1			

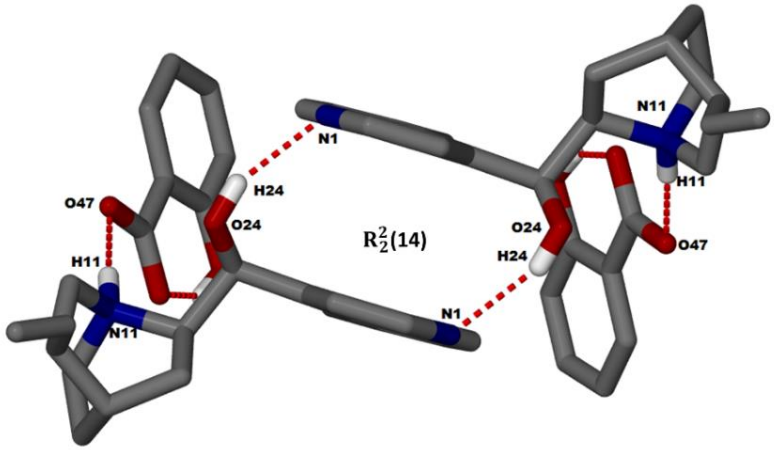

Figure 3.2 Discrete ion pair dimers related by a twofold rotation axis (non H-bonding hydrogens have been omitted for clarity).

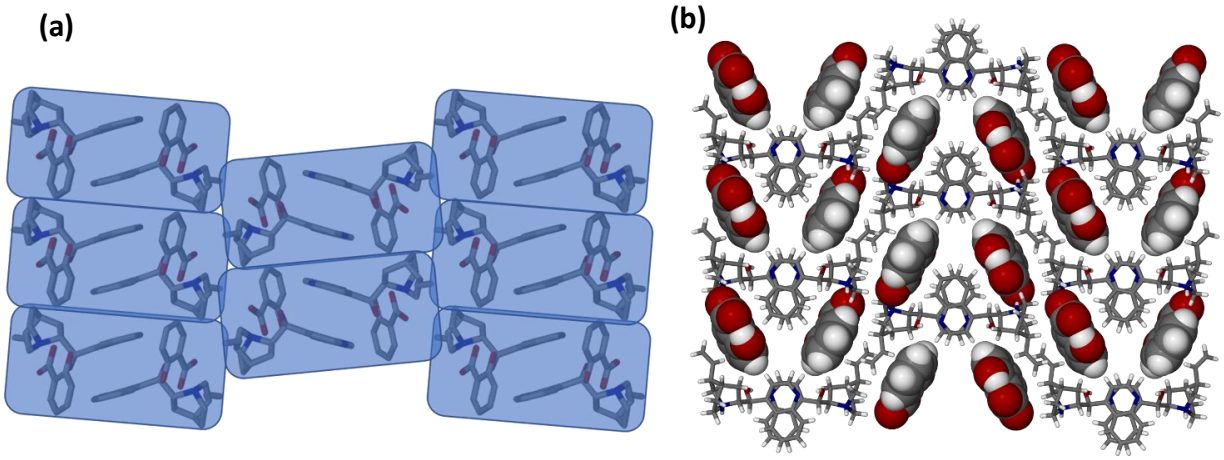

Figure 3.3 Packing in cinchoninium salicylate, (a) how ion pair dimers adopt a brick layer packing along [001], with (b) showing the salicylate ions sitting along channels along [010].

3.1.2 Cinchonidinium salicylate [CIND⁺][SA⁻]

Cinchonidinium salicylate, [CIND⁺][SA⁻], was solved in the monoclinic $P2_1$ chiral space group. The asymmetric unit contains two cinchonidinium ions and two salicylate ions (Figure 3.4). The crystal structure of [CINC⁺][SA⁻], differs significantly to that of [CIND⁺][SA⁻]. This may be a consequence of the difference in geometry of cinchonine (9S,10R) and cinchonidine (9R,10S), resulting in distinct orientations of the hydroxyl group and the quinuclidine ring. The rotation of the quinoline group ($\tau 1$: C3-C4-C9-024), and the swing motion of the quinuclidine moiety ($\tau 2$: 024-C9-C10-N11) are essentially the same for both the molecules of cinchonidine in [CIND⁺][SA⁻] (Table A1). However, a slight shift in the position of the vinyl group ($\tau 3$: C14-C13-C18-C19) is observed, from -116.6° in molecule A to -104.6° in molecule B.

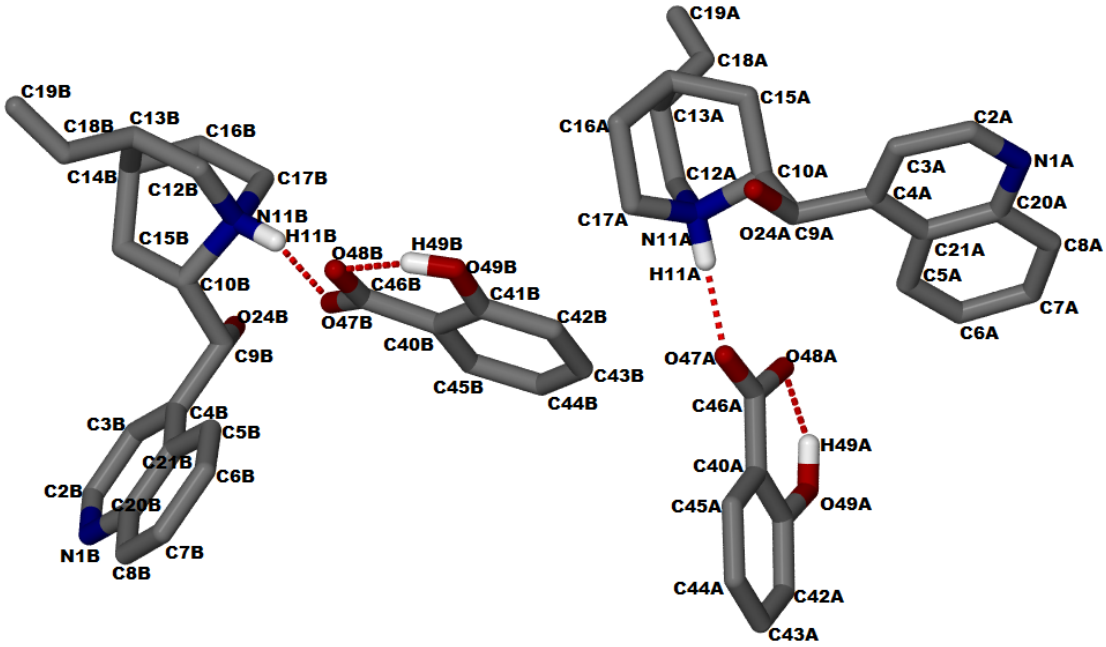

Figure 3.4 Asymmetric unit showing labelling scheme and N⁺-H···O⁻ interaction between the cinchonidinium ion and the salicylate ion (hydrogens are omitted for clarity).

The occurrence of two symmetry independent ion pairs resulted in two distinct hydrogen bonded chains of molecules. These hydrogen bonded systems form independent patterns that can be described by graph set notation.[2] The alternating cations and anions in one ion pair interact via N11A-H11A···O47A (2.70 Å, 170.9°) and O24A-H24A···O48A (2.61 Å, 170.2°) hydrogen bonds forming a 1D $C_2^2(9)$ infinite chain along [001]. Likewise, the second ion pair forms another $C_2^2(9)$ infinite chain along [001] by N11B-H11B···O47B (2.71 Å, 162.9°) and O24B-H24B···O48B (2.71 Å, 174.3°) hydrogen bonds (Figure 3.5). The main H-bonds and short contacts are summarised in Table 3.4.

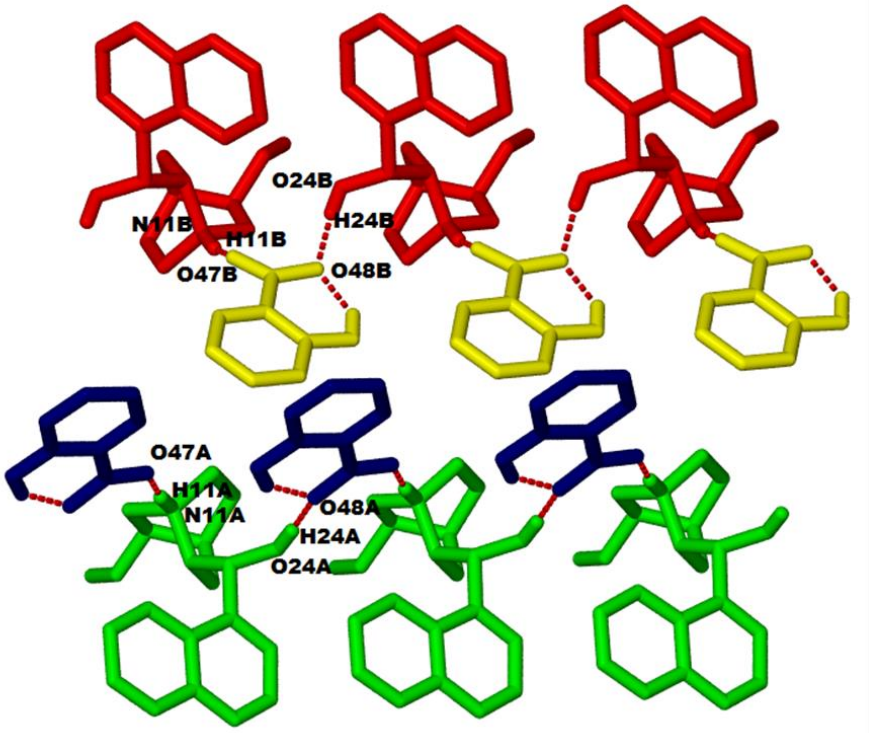

Figure 3.5 Interactions in the infinite chains of alternating cations and anions linked by hydrogen bonds down [001].

Table 3.4 Hydrogen bond and short contact metrics of [CIND$^+$][SA$^-$].

D-H···A	D-H (Å)	H···A (Å)	D···A (Å)	∠D-H···A (°)
N11A-H11A···O47A	0.88	1.82	2.70	170.9
O24A-H24A···O48A^{i}	0.84	1.78	2.61	170.2
O49A-H49A···O48A	0.84	1.77	2.52	146.8
C9A-H9A···O47A	1.00	2.62	3.42	136.8
C12A-H12A···O24A^{ii}	0.99	2.35	3.29	158.2
C13A-H13A···O49A^{iii}	1.00	2.64	3.62	164.6
N11B-H11B···O47B	0.95	1.79	2.71	162.9
O24B-H24B···O48B^{iv}	0.84	1.82	2.66	174.3
O49B-H49B···O48B	0.84	1.79	2.54	146.3
C9B-H9B···O47B	1.00	2.48	3.27	134.6
C12B-H12C···O24B^{v}	0.99	2.49	3.43	159.9
Symmetry codes	(i) [x-1,y,z] (ii) [x+1,y,z] (iii) [x,y,z+1] (iv) [x+1,y,z] (v) [x-1,y,z]			

The packing in cinchonidinium salicylate is shown in Figure 3.6. The main feature is the layers of salicylate ions arranged in a herringbone manner. Furthermore, the quinoline aromatic moieties associate via edge to face π interactions.

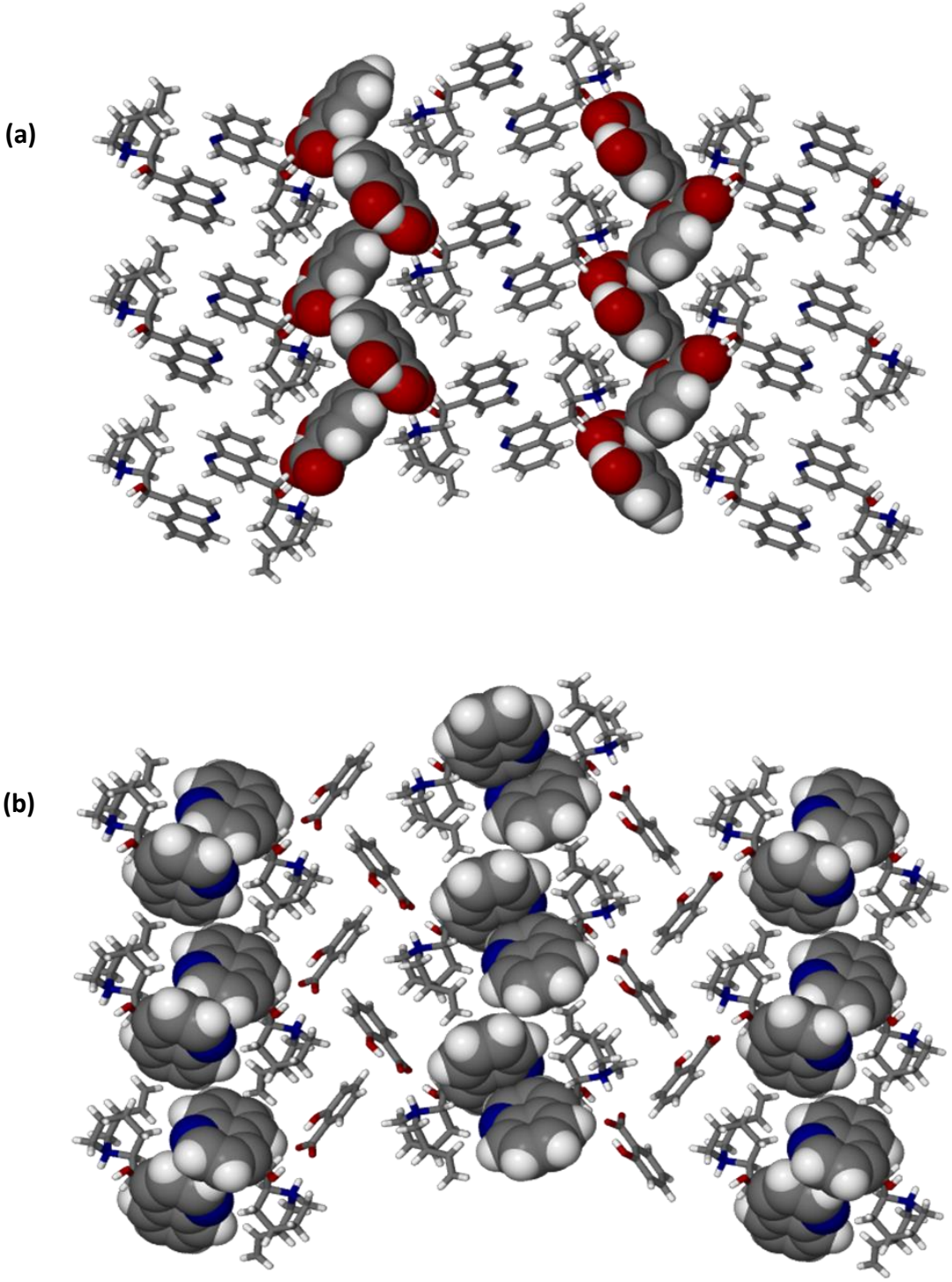

Figure 3.6 Packing of [CIND$^+$][SA$^-$]; (a) highlighting herringbone packing arrangement of salicylate (view down [100]), and (b) showing the edge-to-face packing of the quinoline aromatic moieties (view down [100]).

3.1.3 Quininium salicylate [QUIN$^+$][SA$^-$]

The quininium salicylate structure was solved in the monoclinic chiral, *C*2 space group (Z'=2), with two molecules each of quinine and salicylic acid in the asymmetric unit. The hydrogen bond interactions in the asymmetric unit are shown in Figure 3.7 (a) and the main H-bonds and short contacts are summarised in Table 3.5. The crystal structure of [QUIN$^+$][SA$^-$] is very similar to the structure of [CIND$^+$][SA$^-$]. The only structural difference between CINC and QUIN is the additional methoxy group attached to C6. Despite the extra functional group, similar chains of alternating cations and anions are observed (Figure 3.7b), which are formed through N11A-H11A···O48A (2.67 Å, 173.4°); O24A-H24A···O47A (2.63 Å, 174.7°), in one ion pair, and N11B-H11B···O47B (2.68 Å, 159.7°); O24B-H24B···O48B (2.73 Å, 176.2°) in the other. Moreover, the same herringbone packed layers of salicylic acid (Figure 3.8a) and the edge to face packed quinoline moieties (Figure 3.8b) are present. The three torsion angles $\tau 1$, $\tau 2$ and $\tau 3$ are almost equal for both molecules A and B in [QUIN$^+$][SA$^-$]; (Table A1).

The subtle difference in the packing between [QUIN$^+$][SA$^-$] and [CIND$^+$][SA$^-$] was investigated using the crystal packing similarity tool in Mercury CSD 3.9. The analysis was done by comparing a cluster of 20 molecules, with a tolerance error of 20% on the distances and torsion angles.[3, 4] 17 out of 20 molecules were similarly packed, with a root mean square deviation (RMSD) of 0.479. Despite this likeness the structures are not isostructural, the additional methoxy group on QUIN imparts different symmetry requirements, as such the structures crystallise in different space groups.

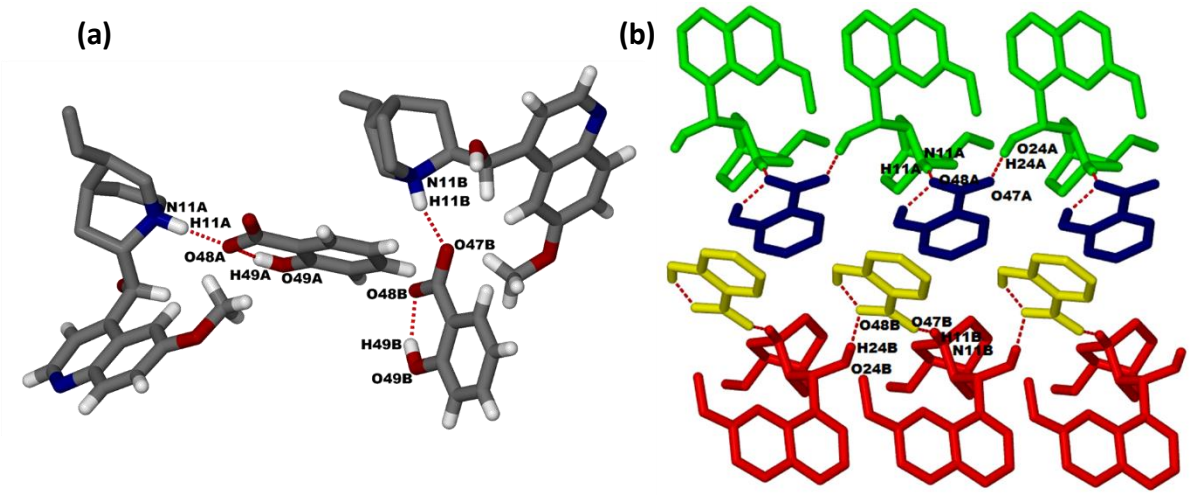

Figure 3.7 (a) Asymmetric unit (Z'=2) showing labelling scheme and N$^+$-H···O interaction between the quininium and the salicylate ion, and (b) chains of alternating cations and anions (view down [100]).

Table 3.5 Hydrogen bonds and short contacts in [QUIN$^+$][SA$^-$].

D-H···A	D-H (Å)	H···A (Å)	D···A (Å)	∠D-H···A (°)
N11A-H11A···O48A	0.96	1.72	2.67	173.4
O24A-H24A···O47A^{i}	0.84	1.79	2.63	174.7
O49A-H49A···O48A	0.84	1.82	2.56	146.1
C7A-H7A···O22A^{ii}	0.95	2.66	3.46	142.9
C12A-H12A···O24A^{iii}	0.99	2.42	3.22	136.5
N11B-H11B···O47B	0.92	1.80	2.68	159.7
O24B-H24B···O48B^{iii}	0.84	1.89	2.73	176.2
O49B-H49B···O48B	0.84	1.81	2.55	147.1
C5B-H5B···O47B	0.95	2.51	3.46	177.8
C9B-H9B···O47B	1.00	2.55	3.30	131.3
C12B-H12D···O24B^{i}	0.99	2.46	3.31	143.7
Symmetry codes	(i) [x,y+1,z] (ii) [-x+1,y,-z+1] (iii) [x,y-1,z]			

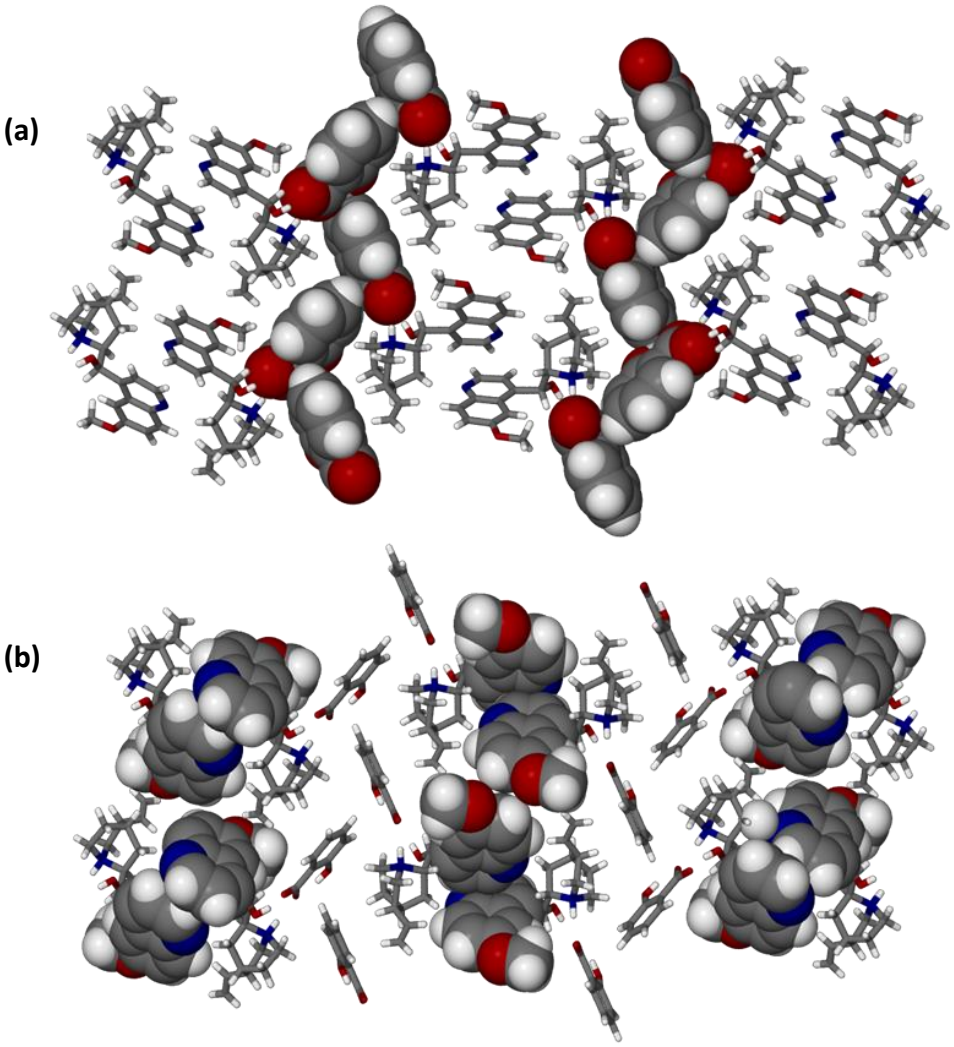

Figure 3.8 Packing of [QUIN$^+$][SA$^-$] viewed down [010]; (a) highlighting herringbone packing arrangement salicylate ions, and (b) showing the edge-to-face packing of the quinoline aromatic moieties.

3.1.4 Quinidinium salicylate [QUID$^+$][SA$^-$]

Quinidinium salicylate, [QUID$^+$][SA$^-$], was solved in the orthorhombic space group $P2_12_12$ and is isostructural with the previously discussed [CINC$^+$][SA$^-$] (Table 3.2). Yet again, the only difference between QUID and CINC is the presence of a methoxy group, which shows disorder in [QUID$^+$][SA$^-$]. The hydrogen bonding in [QUID$^+$][SA$^-$] salt pair is also very similar to [CINC$^+$][SA$^-$] and can be described by the formation of a N11-H11···O47 (2.66 Å, 174.2°) charge assisted hydrogen bond and the intramolecular interaction of O49-H49···O47 (2.45 Å, 150.4°). The hydrogen bonds and short contacts are summarised in Table 3.6. Additionally, analogous to [CINC$^+$][SA$^-$], we observe ion pair dimers (Figure 3.9b). However, these ion pair dimers stack with a slightly different orientation (Figure 3.10a). Packing similarity analysis of [QUID$^+$][SA$^-$] and [CINC$^+$][SA$^-$] gave 20 out of 20 molecules in common (Figure 3.11), with an RMSD of 0.407; confirming that the two salts are isostructural.

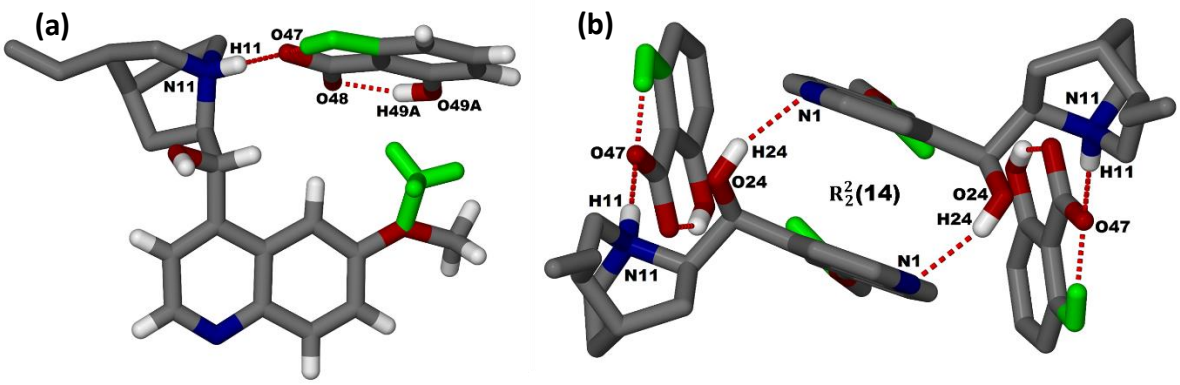

Figure 3.9 Asymmetric unit of [QUID$^+$][SA$^-$] with labelling and the N$^+$-H···O$^-$ interaction between the quinidinium and the salicylate ion (quinuclidine ring hydrogens are omitted for clarity and the minor disorders are highlighted green).

Table 3.6 Hydrogen bonds and short contacts in [QUID$^+$][SA$^-$].

D-H···A	D-H (Å)	H···A (Å)	D···A (Å)	∠D-H···A (°)
N11-H11···O47	0.96	1.71	2.66	174.2
O24-H24···N1^{i}	0.84	2.11	2.92	161.1
O49B-H49B···O47	0.84	1.68	2.45	150.4
O49A-H49A···O48	0.84	1.75	2.51	150.6
C17-H17A···O47^{iv}	0.99	2.49	3.34	143.9
C23B-H23F···O22^{v}	0.98	2.52	3.41	151.1
C23B-H23E···O48	0.98	2.31	3.26	161.9
C44-H44···O48	0.95	2.62	3.49	152.1
Symmetry codes:	(i) [-x,-y+1,z] (ii) [x,y-1,z] (iii) [-x+1/2,y-1/2,-z+1] (v) [-x,-y+1,z] (vi) [x,y+1,z]			

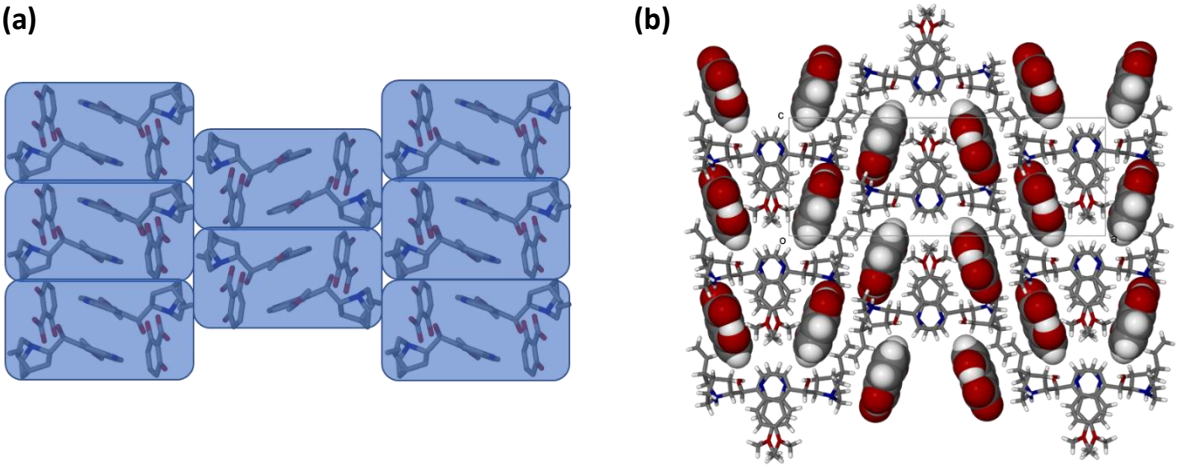

Figure 3.10 (a) Packing in quinidinium salicylate showing how the ion pair dimers adopt a brick layer packing, with (b) the salicylate ions sitting along channels down [010].

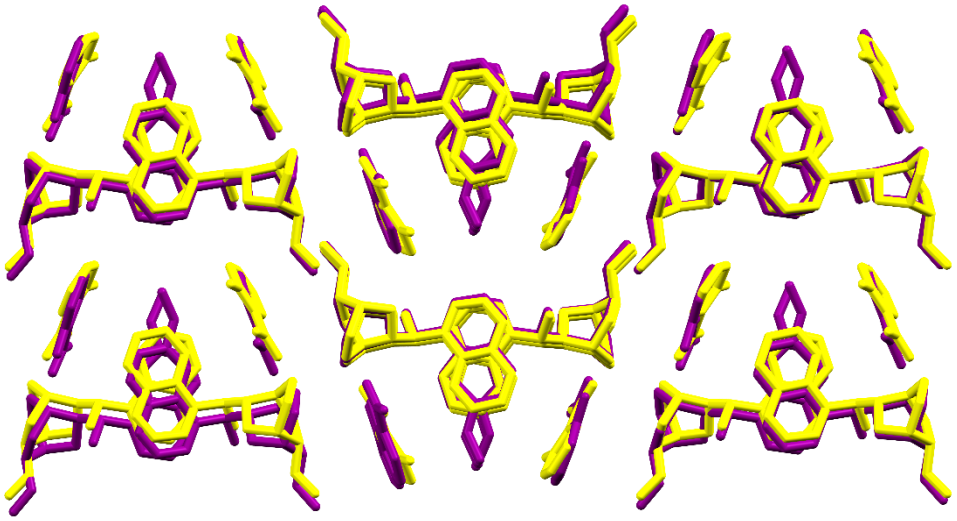

Figure 3.11 Isostructural packing cations and anions in cinchoninium (yellow) and quinidinium (purple) salicylate.

The methoxy group of the quininium moiety and the hydroxyl group of the salicylate are disordered over two positions with unequal site occupancy factors (SOF). The SOF for C23A is 0.53, C23B =0.47, 049A =0.37, and O49B =0.63. Disorder is a phenomenon which occasionally occurs during structure elucidation and it is the non-systematic arrangement of the contents of the asymmetric unit.[5] Essentially molecules are always undergoing vibrational motion, thus SCXRD gives a time averaged X-ray diffraction pattern. However, large amplitudes of vibration can sometimes occur. Substitutional disorder forms when the same position in different unit cells is occupied by different atoms. This crystal structure displays positional disorder.

3.2 N-benzylcinchona alkaloid salicylates

Equimolar co-crystallization of SA with NBQUIN, NBCINC and NBCIND from a 1:1 solution of ethyl acetate-water, resulted in crystalline molecular salts that are stabilized via O–H···$^{-}$O hydrogen bonds. The crystallographic data and refinement parameters are summarised in Table 3.7.

Table 3.7 Crystallographic data for the N-benzylcinchona alkaloid salicylates.

	[NBCINC^{+}][SA^{-}]	**[NBCIND^{+}][SA^{-}]**	**[NBQUIN^{+}][SA^{-}]**
Molecular formula	$C_{33}H_{34}N_2O_4$	$C_{33}H_{34}N_2O_4$	$C_{34}H_{36}N_2O_5$
Mr (g mol^{-1})	522.62	522.62	552.65
Crystal system	monoclinic	monoclinic	monoclinic
Space group	$P2_1$	$C2$	$C2$
a/Å	9.819(2)	19.560(4)	20.289(4)
b/Å	6.7945(14)	6.5720(13)	6.7165(13)
c/Å	20.130(4)	20.910(4)	21.025(4)
α/°	90	90	90
β/°	91.26(3)	93.79(3)	95.24(3)
γ/°	90	90	90
Volume/Å^3	1342.7(5)	2682.1(9)	2853.1(10)
Z, Z′	2	4	4
ρ (calc.)/ mg m^{-3}	1.293	1.294	1.287
μ(MoKα)/ mm^{-1}	0.085	0.085	0.086
F (000)	556.0	1112.0	1176.0
Crystal size (mm)	0.27×0.22×0.18	0.61×0.30×0.28	0.56×0.48×0.47
Temperature (K)	173 (2)	173 (2)	173 (2)
Radiation [Å]	0.71073	0.71073	0.71073
Theta min-max [°]	2.024, 27.975	1.952, 27.125	0.973, 27.934
Dataset	-11:12, -8:8, -26:26	-24:24, -8:8, -26:26	-26:26, -8:8, -27:27
Final R indices [I>2.0 sigma (I)]	R1=0.0442, wR2=0.0965	R1=0.0658, wR2=0.1828	R1= 0.0398, wR2= 0.1064
R indices (all data)	R1=0.0562, wR2=0.1025	R1=0.0786, wR2=0.1944	R1= 0.0429, wR2= 0.1092
Tot., uniq. data, R (int)	6440, 5378, 0.0314	5933, 4910, 0.0282	6808, 6362, 0.0278
N_{ref}, N_{par}	6440, 354	5933, 352	6808, 373
S	1.033	1.040	1.026
Max, av. Shift/error	0.00, 0.00	0.00, 0.00	0.00, 0.00
Min and max. resd. dens.(Å^3)	-0.195, 0.202	-0.385, 0.992	-0.221, 0.361

3.2.1 N-benzylcinchoninium salicylate [NBCINC$^+$][SA$^-$]

The crystal structure of N-benzylcinchoninium salicylate, [NBCINC$^+$][SA$^-$], crystallises in the monoclinic chiral space group $P2_1$. The asymmetric unit has a N-benzylquininium ion and a salicylate ion that associate through a O24-H24···O47 (2.73 Å, 173.0^o) hydrogen bond. The labelling scheme and the hydrogen bond interactions in the asymmetric unit are shown in Figure 3.12 and the H-bonds and short contacts are summarised in Table 3.8. The conformation of the quinoline, quinuclidine and vinyl groups of NBCINC differ to the conformations observed in the rest of the cinchona alkaloids. The recorded values of $\tau 1$, $\tau 2$ and $\tau 3$ are 11.6^o, 55.76^o and -13.2^o respectively. This unique orientation might be the reason why [NBCINC$^+$][SA$^-$] packs in the same way as [NBCIND$^+$][SA$^-$] and [NBQUIN$^+$][SA$^-$] despite having a different geometry. The main feature in the packing of N-benzylquininium salicylate, shown in Figure 3.13, is the tubular voids formed by NBCINC, which are stabilised purely by *van der Waals* forces. The voids are filled by salicylate ions which interact to the NBCINC ions through O24-H24···O47 hydrogen bonds (Figure 3.14). The quinoline aromatic moieties, akin to all structures discussed thus far, form an edge to face packing arrangement.

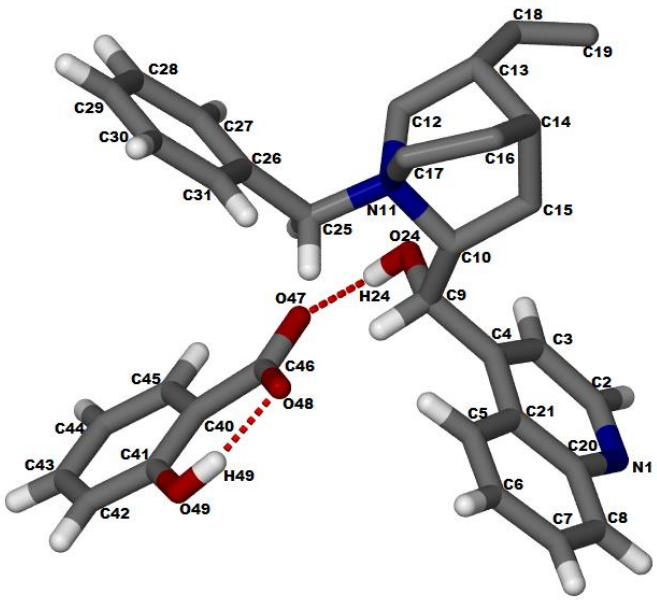

Figure 3.12 Asymmetric unit showing labelling scheme and O-H···O interaction between the N-benzylcinhoninium ion and the salicylate ion (quinuclidine hydrogens are omitted for clarity).

Table 3.8 Hydrogen bond and short contact metrics of [NBCINC$^+$][SA$^-$].

D-H···A	D-H (Å)	H···A (Å)	D···A (Å)	∠D-H···A (°)
O24-H24···O47	0.84	1.90	2.73	173.0
O49-H49···O48	0.84	1.74	2.49	147.4
O24-H24···O48	0.84	2.60	3.21	130.5
C9-H9···O48	1.00	2.34	3.11	132.6
C12-H12A···O24	0.99	2.34	3.03	126.2
C15-H15B···N1^{i}	0.99	2.55	3.51	161.7
C17-H17A···O47^{ii}	0.99	2.55	3.44	149.9
C25-H25B···O24	0.99	2.51	3.12	119.8
C25-H25A···O47^{iii}	0.99	2.55	3.41	145.1
Symmetry codes:	(i) [-x+1,y+1/2,-z] (ii) [x,y+1,z] (iii) [x,y+1,z]			

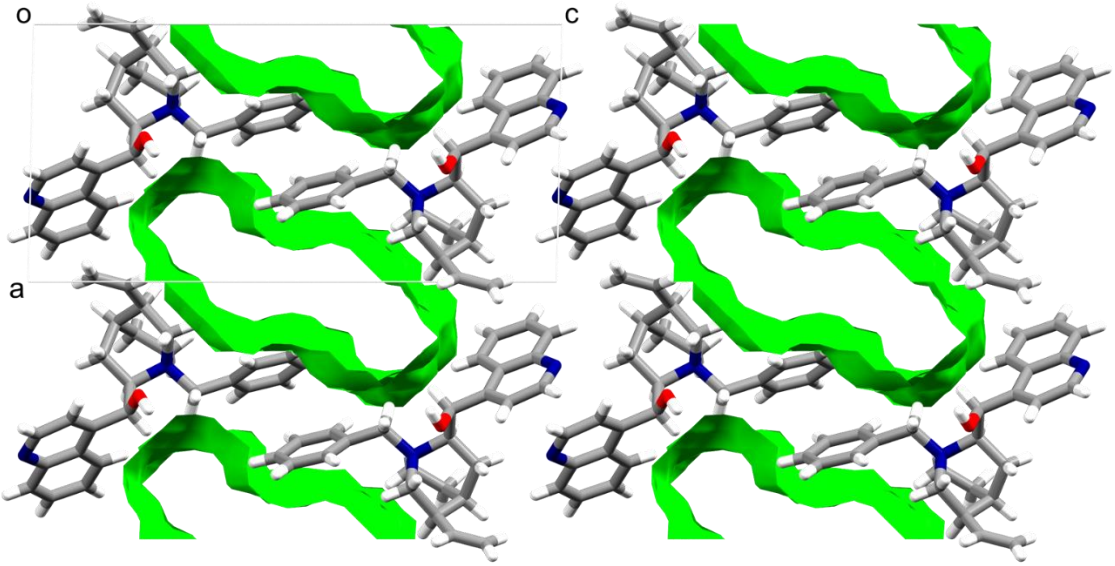

Figure 3.13 N-benzylcinchoninium salicylate packing highlighting the nanotubular voids formed by NBQUIN; contact surface calculated with 1.2 Å probe radius and 0.7 Å grid space.

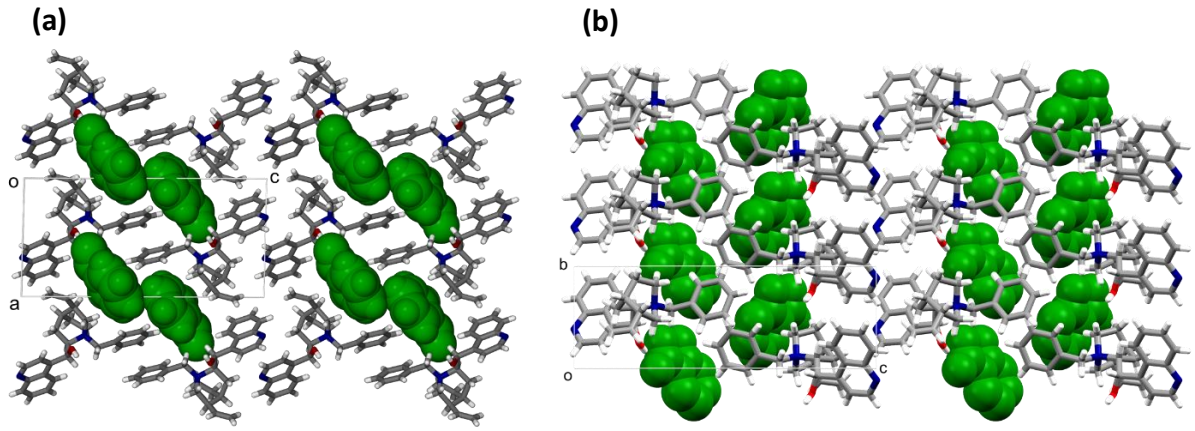

Figure 3.14 N-benzylcinchoninium salicylate packing showing how the voids are filled with salicylate.

3.2.2 N-Benzylcinchonidinium salicylate [NBCIND$^+$][SA$^-$]

N-Benzylcinchonidinium salicylate [NBCIND$^+$][SA$^-$] was solved in the monoclinic chiral space group *C*2, with a molecular formula of $C_{33}H_{34}N_2O_4$. The asymmetric unit has a N-benzylcinchonidinium ion and a salicylate ion. The hydrogen bond interactions can be described by N11-H11···O47 (2.73 Å, 173.0^o) and the intramolecular interaction O49-H49···O47 (2.73 Å, 173.0^o); (Figure 3.15). The H-bond and short contacts are summarised in Table 3.9. The carboxyl group of the salicylate ion is disordered and refined to 61:39 site occupancy. Contrary to the unsubstituted cinchona alkaloids, the change in geometry from NBCINC to NBCIND did not affect the overall packing. Therefore, comparable tubular voids (Figure 3.16) that are occupied by SA are observed (Figure 3.17).

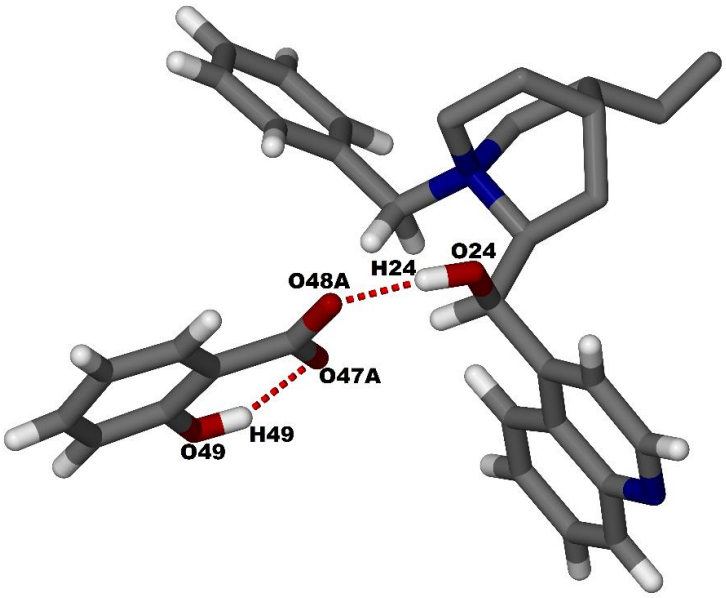

Figure 3.15 Asymmetric unit showing labelling scheme and O-H···O$^-$ interaction between the N-benzylcinhonidinium ion and the salicylate ion (only the major disorder of the carboxylate is shown and the quinuclidine ring hydrogens are omitted for clarity).

Table 3.9 Hydrogen bond and short contacts of [NBCIND$^+$][SA$^-$].

D-H···A	D-H (Å)	H···A (Å)	D···A (Å)	∠D-H···A (°)
O24-H24···O48A	0.84	1.75	2.58	174.0
O24-H24···O48B	0.84	1.80	2.60	158.7
O49-H49···O47A	0.84	1.77	2.51	147.9
O49-H49···O47B	0.84	1.87	2.53	134.6
C9-H9···O47A	1.00	2.26	3.14	146.0
C9-H9···O47B	1.00	2.48	3.31	139.6
C12-H12A···O49^{i}	0.99	2.61	3.39	135.3
C13-H13···O49^{ii}	1.00	2.65	3.42	133.9
C25-H25B···O48A^{iii}	0.99	2.30	3.22	153.6
C25-H25B···O48B^{iv}	0.99	2.15	3.09	158.7
C25-H25A···O47A	0.99	2.47	3.41	160.0
Symmetry codes:	(i) [x-1/2,y+1/2,z] (ii) [x-1/2,y+1/2,z] (iii) [x,y+1,z] (iv) [x,y+1,z]			

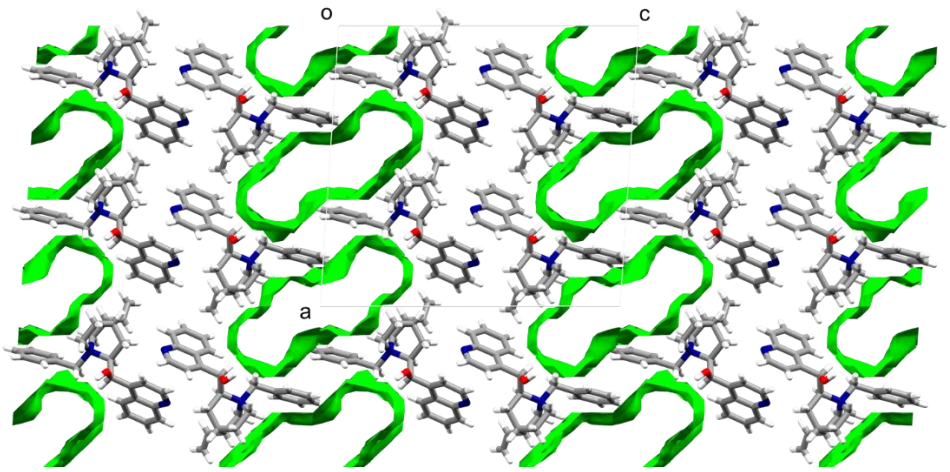

Figure 3.16 N-benzylcinchonidinium salicylate packing highlighting the nanotubular voids formed by NBCIND. contact surface calculated with 1.2 Å probe radius and 0.7 Å grid space.

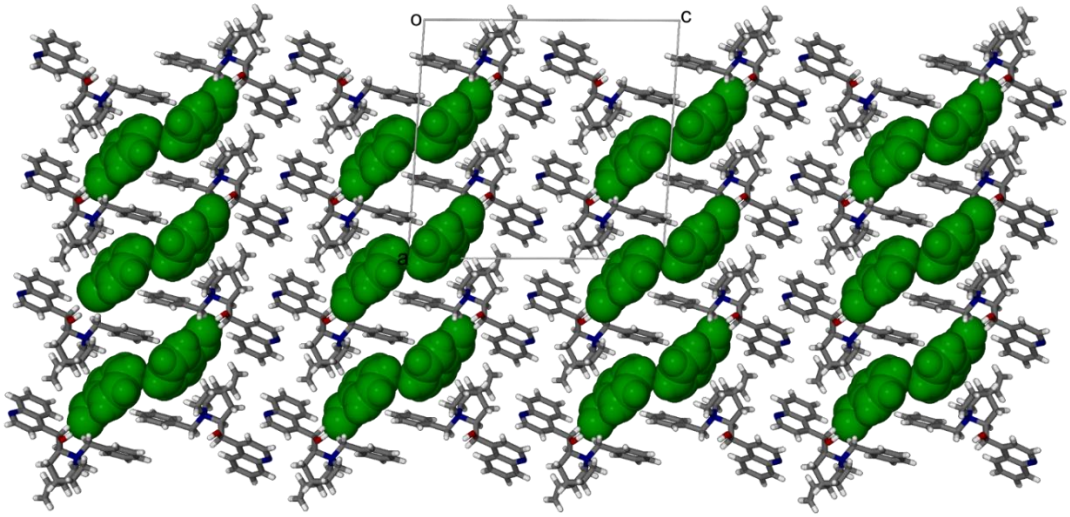

Figure 3.17 N-benzylcinchonidinium salicylate packing showing how the voids are filled with salicylate.

3.2.3 N-benzylquininium salicylate [NBQUIN$^+$][SA$^-$]

Quininium salicylate, [NBQUIN$^+$][SA$^-$], was solved in the monoclinic chiral space group *C*2. The components of the asymmetric unit form a discrete assembly via a O24-H24···O47 (2.60 Å, 170.2°) hydrogen bond, which is described by the $D_2^2(4)$ graph set. In addition, there is a O49-H49···O47 (2.55 Å, 143.2°) intramolecular hydrogen bond resulting in a $S_2^2(4)$ graph set. The H-bond and short contact matrices are summarised in Table 3.10. N-benzylquininium salicylate and N-benzylcinchonidinium salicylate are isostructural, with the corresponding tubular voids (Figure 3.19a) occupied by SA (Figure 3.19b). The similarity packing analysis found 20 out of 20 molecules in common (Figure 3.20), with an RSMD of 0.58. Also, the values of $\tau 1$, $\tau 2$ and $\tau 3$ in the structures of [NBQUIN$^+$][SA$^-$] and [NBCIND$^+$][SA$^-$]are essentially the same (Table A1).

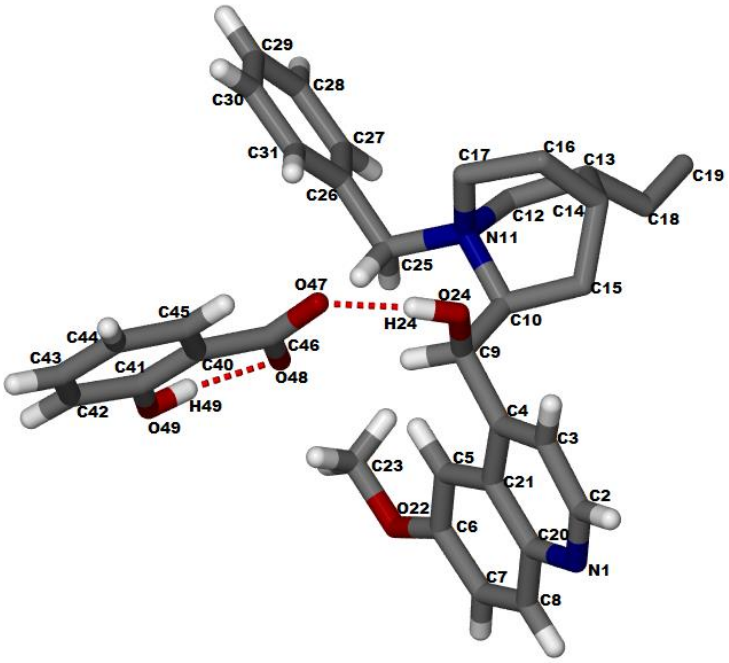

Figure 3.18 Asymmetric unit showing labelling scheme and O-H···O$^-$ interaction between the N-benzylquininium ion and the salicylate ion (quinuclidine ring hydrogens are omitted for clarity).

Table 3.10 Hydrogen bond and short contact matrices of [NBQUIN$^+$][SA$^-$].

D-H···A	D-H (Å)	H···A (Å)	D···A (Å)	∠D-H···A (°)
O24-H24···O47	0.84	1.76	2.60	170.2
O49-H49···O48	0.84	1.83	2.55	143.2
C9-H9···O48	1.00	2.38	3.32	154.9
C17-H17A···O24	0.99	2.40	2.97	116.3
C25-H25A···O48	0.99	2.35	3.31	161.8

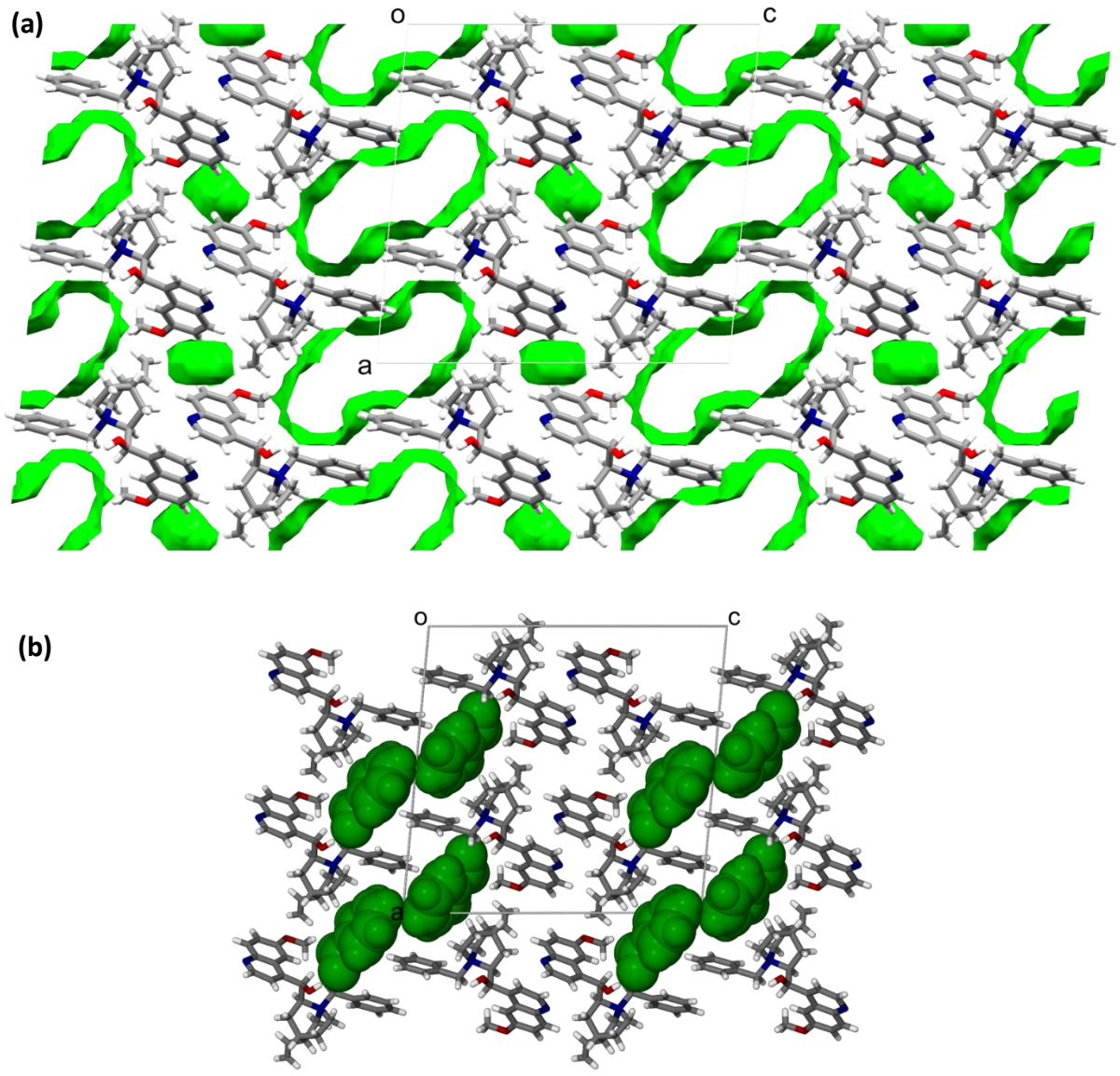

Figure 3.19 N-benzylquininium salicylate packing highlighting (a) the nanotubular voids formed by NBQUIN (contact surface calculated with 1.2 Å probe radius and 0.7 Å grid space), and (b) how voids are filled with salicylate.

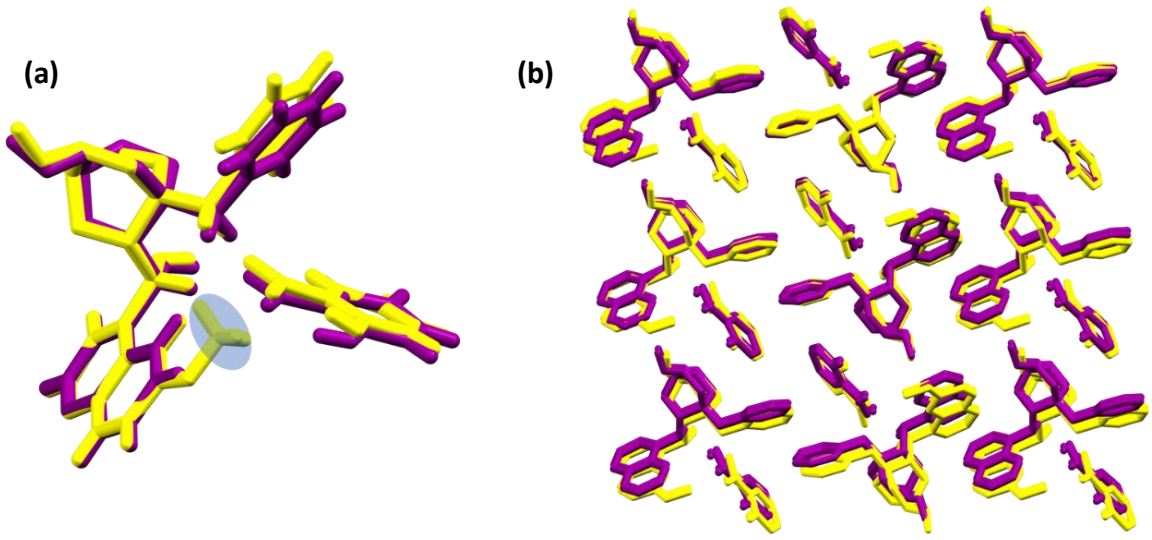

Figure 3.20 Isostructural packing cations and anions in [NBQUIN$^+$][SA$^-$] (yellow) and [NBCIND$^+$][SA$^-$] (purple). The additional methoxy group highlighted blue in (a) occupies space in voids.

3.3 Bulk property analysis (DSC, TGA and PXRD)

The change in melting point observed during multicomponent crystal screening is indicative of the formation of any new solid form. The DSC and TGA profiles were generated in the temperature range of 30 ^{o}C to 300 ^{o}C (Appendix Figure. A1-A7, summarized in Table 3.11). The DSCs are generally uneventful (i.e. no unexpected phase transitions are recorded) and show pure melting of the salts. In the case of [QUIN$^+$][SA$^-$] a small broad endotherm is noted around 65 ^{o}C but no related mass change is observed on the TGA curve. It is believed that the cause of this event is the existence of some solvent remains on the analysed crystals. Another unusual thermal event was observed when crystals of [CIND$^+$][SA$^-$] was analysed. A 'drop' in the DSC signal was observed around 145 ^{o}C and the TGA shows a 5 % mass loss in this temperature range. These observations would suggest possible solvent/water inclusion in the structure, but this is not supported by the analysis of the single crystal.

The single crystal structure is representative of the bulk material based on the very similar powder patterns. Thus, a possible explanation of the latent solvent inclusion is that the crystals were very fine and were difficult to dry before thermal analysis. It is believed that the observed events are the result of significant amount of surface solvent. It may be concluded that the cocrystallisation of SA with the selected cinchona alkaloids resulted in the formation of more thermally stable adducts. The melting endotherms of [CINC$^+$][SA$^-$], [NBQUIN$^+$][SA$^-$], [NBCINC$^+$][SA$^-$] and [NBCIND$^+$][SA$^-$] are between the melting point of salicylic acid and the

respective cinchona alkaloid, while the melting points of [QUIN$^+$][SA$^-$], [QUID$^+$][SA$^-$] and [CIND$^+$][SA$^-$] are higher than both of the starting materials. The TGA curves for all the structures (except for [CIND$^+$][SA$^-$] discussed previously) have only one thermal event, which corresponds to the melting and decomposition of the salt, thus the thermographs indicate that all multicomponent crystals are solvent-free.

Table 3.11 Summary of DSC results

	Melting (°C)	
	T_{on}	T_{peak}
CINC	260.7	262.3
CIND	203.9	205.2
QUIN	176.4	178.3
QUID	171.7	173.1
NBCINC	266.2	268.6
NBCIND	220.4	223.9
NBQUIN	230.0	232.1
[CINC$^+$][SA$^-$]	172.2	175.9
[CIND$^+$][SA$^-$]	207.8	211.3
[QUIN$^+$][SA$^-$]	202.2	204.6
[QUID$^+$][SA$^-$]	169.5	174.5
[NBCINC$^+$][SA$^-$]	207.5	210.7
[NBCIND$^+$][SA$^-$]	213.5	216.7
[NBQUIN$^+$][SA$^-$]	207.2	209.2

Powder X-ray diffraction was used to identify the formation of the new solid forms and to verify that the collected single crystal data is representative of the bulk material. The PXRD of pure SA, cinchona alkaloids, and their respective products obtained via slow evaporation are given in Appendix Figure A8-A14. All the experimental PXRD patterns of the bulk crystals are distinctively different from the starting material, indicating that new solid forms have been synthesised. Parallel to this, the simulated XRD patterns of the single crystal structures agree with the experimental patterns of the bulk material, proving that the collected single crystal is representative of the bulk. The only exception is [QUIN$^+$][SA$^-$], where the agreement between the experimental and the simulated pattern is partial. To clarify this observation, which is probably connected to the endothermic event observed around 65 °C on the DSC, further experiments will be conducted.

3.4 Dissolution of multicomponent crystals of salicylic acid

The rates of dissolution of SA and its multicomponent crystals in water were measured using high performance liquid chromatography coupled with a mass spectrometer (HPLC-MS). The calibration standards (Table A2), calibration curve (Figure A15) and typical chromatographs of the experimental HPLC-MS results (Figure A16-A23) are given in the appendix. The cumulative concentrations are summarised in Table A3 and the dissolution profiles are shown in Figure 3.21. The concentration of salicylic acid after an hour is 0.4651 mg mL^{-1}. This cumulative concentration decreases in the multicomponent crystals, to 0.2234 mg mL^{-1} in [CINC$^+$][SA$^-$], 0.2015 mg mL^{-1} in [CIND$^+$][SA$^-$], 0.1825 mg mL^{-1} in [QUID$^+$][SA$^-$] and 0.1654 mg mL^{-1} in [QUIN$^+$][SA$^-$], which translates to a 2.1-2.8 fold decrease in rate of dissolution. Upon cocrystallization with the N-benzyl-substituted cinchona alkaloids a further decrease is observed. The concentration of SA from [NBQUIN$^+$][SA$^-$] after the hour is 0.1143 mg mL^{-1} , and 0.1046 mg mL^{-1} in [NBCINC$^+$][SA$^-$] and 0.0786 mg mL^{-1} in [NBCIND$^+$][SA$^-$] which corresponds to a 4.1-5.9 fold decrease in the rate of dissolution. Thus, the novel crystal forms of SA present a systematic decrease in the dissolution rates and the results suggest that the benzyl substituted alkaloids are more effective in supressing the aqueous solubility of SA.

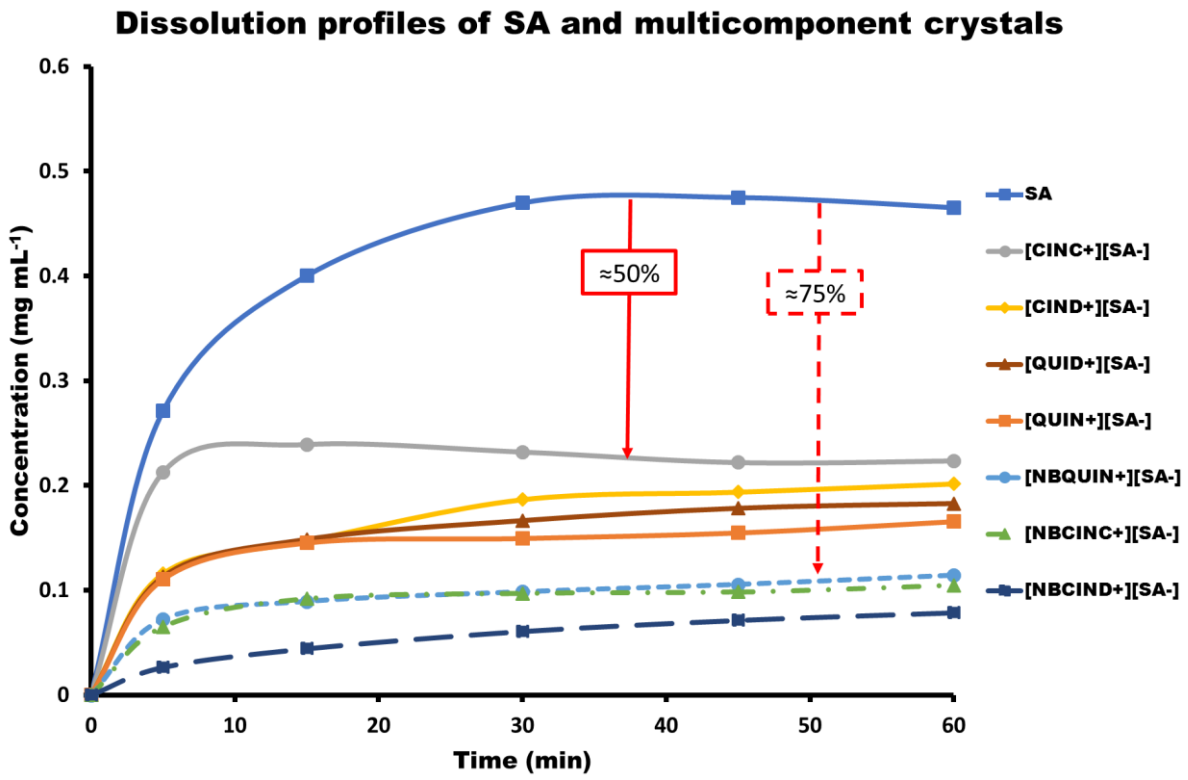

Figure 3.21 First hour dissolution profiles of SA and its multicomponent crystals in water.

3.5 Crystal surface analysis

There is a strong correlation between the changes in physicochemical properties and the molecular configuration at the surfaces of a material.[6] Putra *et al* investigated how direct observation during solubilisation can be used to rationalise structure-solubility relations. Using a microscope, they monitored the change in the crystal shape during solubilisation. They noticed that the crystal shape (change in transparency) occurred more significantly on the hydrophilic faces compared to the hydrophobic faces. This observation showed that a polar solvent penetrates the faces of the crystal that are hydrophilic to a larger extent and less on the sides that are hydrophobic. Hence, they concluded that given more model systems the change in solubility can be monitored by analysing the hydrophilic/hydrophobic nature of the crystal surfaces.[7]

Using this reasoning, we calculated the crystal morphologies of the novel multicomponent crystals and studied the hydrophobic/hydrophilic nature of the crystal faces and related the observations to the changes in solubility. Unfortunately, the face indexed data of the collected single crystals are not available anymore, thus from here on the discussed calculations are purely theoretical. Nonetheless, the analysis of the crystal structures with this recently reported method happened to be very useful when interpreting the solubility results.

The bulky cinchona alkaloids are largely hydrophobic; as such the pure compounds have relatively low aqueous solubility. In contrast, the much smaller salicylic acid is hydrophilic and hence the comparatively higher solubility. The depictions of the calculated crystal morphology (with the aid of Mercury BFDH morphology prediction)[8-10] and the packing along each crystal face (viewed down the unit cell axes) is given in Figures 3.22-3.28. The packing diagrams were created by defining the Miller planes according to the plane covering the morphology of the crystal. A slice of the crystal was constructed on either side of this plane with the depth, area and displacement set at 10, 20 and 0 respectively. The hydrophobic cinchona alkaloids are in space fill mode; and the hydrophilic salicylate ions are the stick models and are coloured yellow.

The packing in $[CINC^{+}][SA^{-}]$ is such that the solvent can access the hydrophilic SA from all the crystal faces, which supports the observation of the highest rate of dissolution (Figure 3.22). Although the crystal structure of $[QUID^{+}][SA^{-}]$ is very similar to that of the cinchoninium

salicylate, the rate of dissolution is lower than expected. A plausible explanation is the presence of disorder in the quinidinium salicylate structure, which translated into unexpected physicochemical properties. In the [QUIN$^+$][SA$^-$] and [CIND$^+$][SA$^-$] crystal structures, the dominant crystal faces, (001) and (020), are covered by hydrophobic cinchona alkaloid molecules and the solvent has no easy access to the hydrophilic SA molecules. However, the solvent still has access to SA from two of the faces and so the reduction of the rate of dissolution from that of [CINC$^+$][SA$^-$] is not significant. In contrast, the crystal structures of [NBQUIN$^+$][SA$^-$], [NBCINC$^+$][SA$^-$] and [NBCIND$^+$][SA$^-$] have two crystal faces (including the dominant face) that are completely covered by hydrophobic cinchona alkaloids. The solvent has access to the hydrophilic interior only through channels on one of the minor crystal surfaces of each of these structures. The clear disparity in rate of dissolution between the unsubstituted cinchona alkaloid salicylates and the N-benzyl substituted cinchona alkaloid salicylates can be attributed to the presence of more faces that are covered by hydrophobic molecules in the latter.

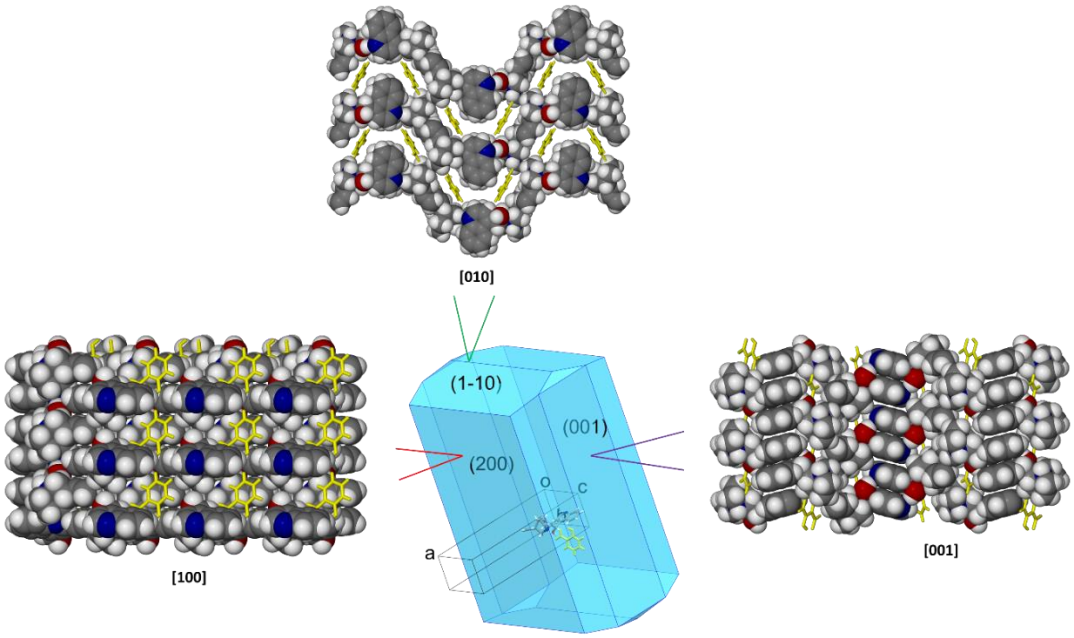

Figure 3.22 Calculated [CINC$^+$][SA$^-$] morphology and the packing along each face. The dominant crystal face viewed down [100] is hydrophilic, and the two minor faces viewed down [010] and [001] also show hydrophilic character.

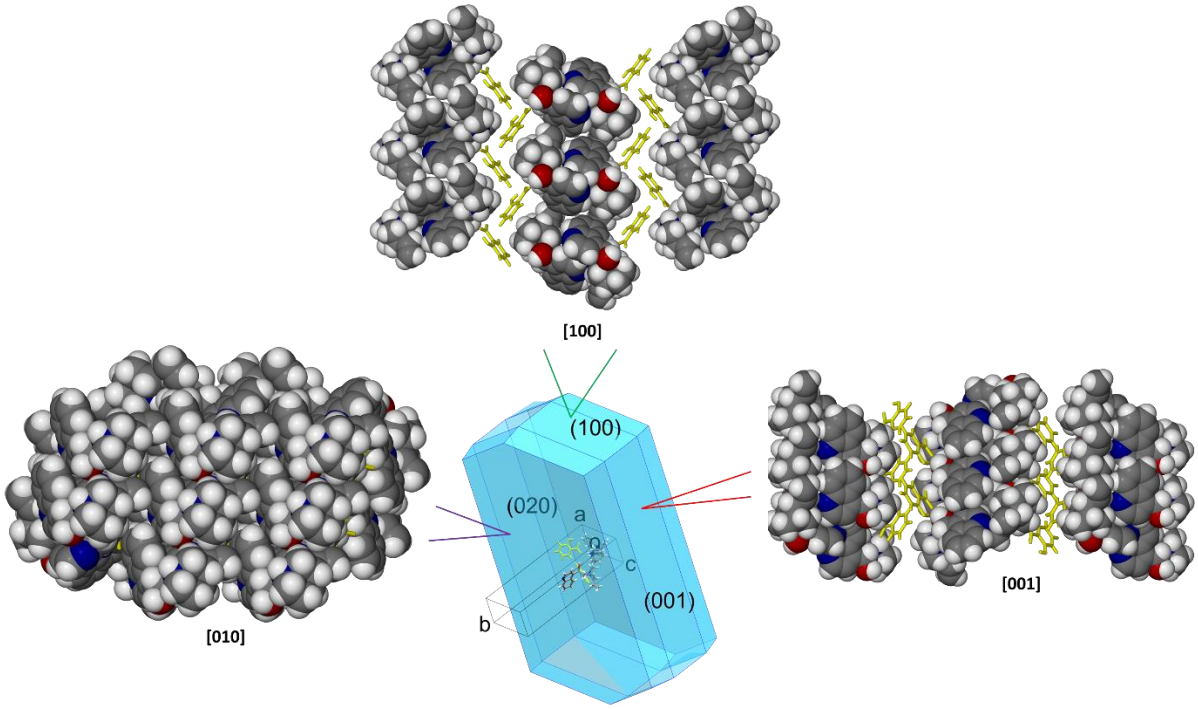

Figure 3.23 Calculated [CIND$^+$][SA$^-$] morphology and the packing along each face. The dominant crystal face viewed down [010] is hydrophobic; and the two minor faces (viewed down [001] and [100]) are hydrophilic.

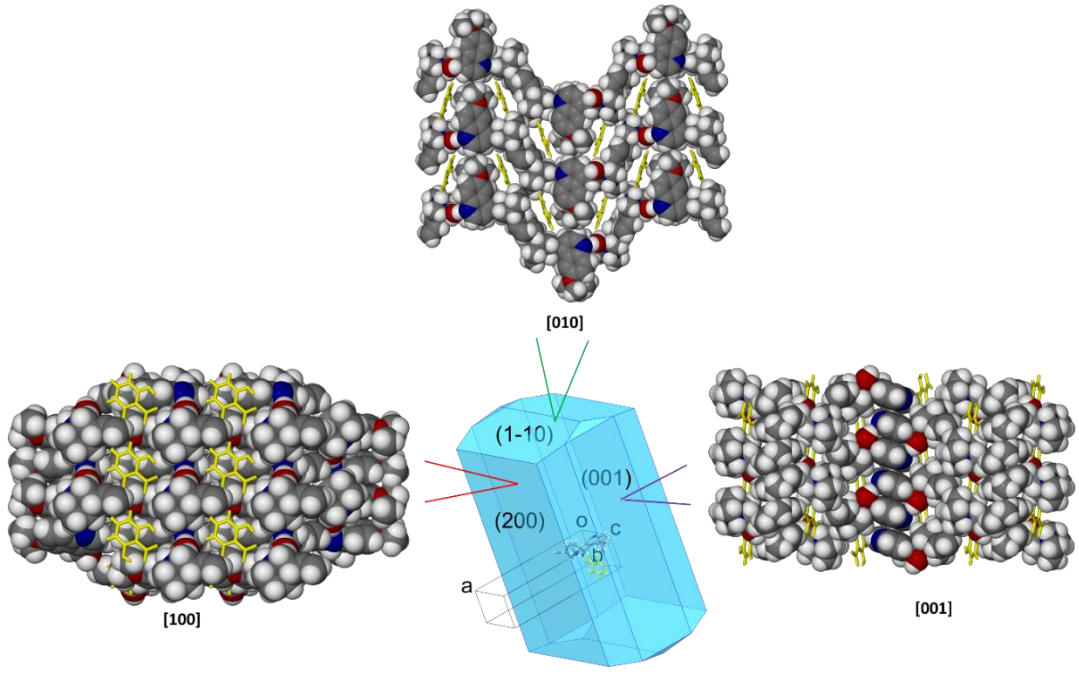

Figure 3.24 Calculated [QUID$^+$][SA$^-$] morphology and the packing along each face. The dominant crystal face viewed down [100] is hydrophilic, and the two minor faces viewed down [001] and [100] are also hydrophilic.

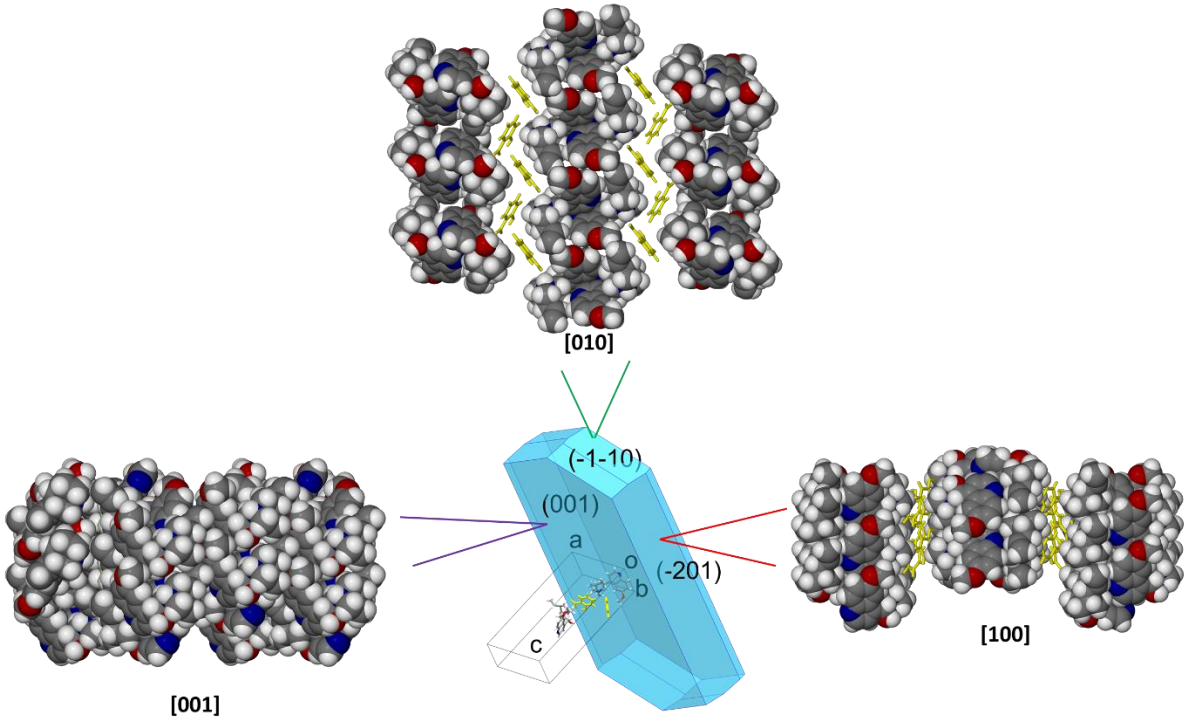

Figure 3.25 Calculated [QUIN$^+$][SA$^-$] morphology and the packing along each face. The dominant crystal face view down [001] is hydrophobic. The minor faces viewed down [100] and [010] are hydrophilic.

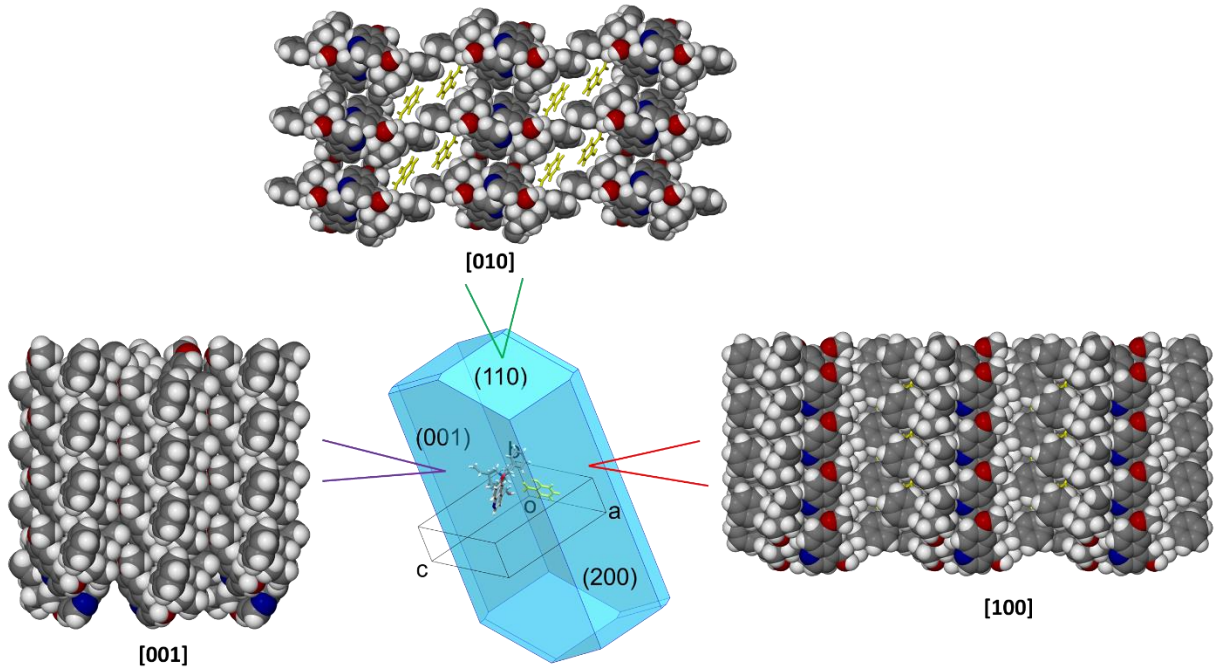

Figure 3.26 The calculated [NBQUIN$^+$][SA$^-$] morphology and the packing along each face. The dominant crystal face viewed down [001] and one minor face viewed down [100] are hydrophobic, whilst the minor face viewed down [010] is hydrophilic.

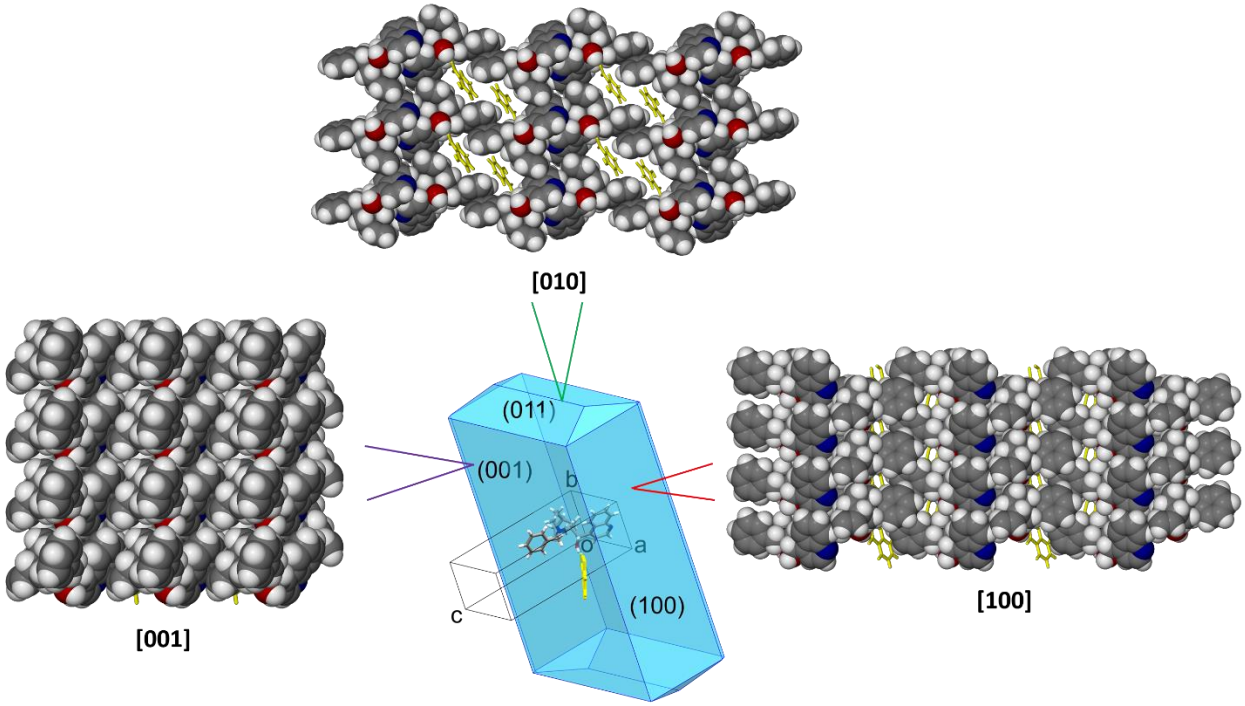

Figure 3.27 The calculated [NBCINC$^+$][SA$^-$] morphology and the packing along each face. The dominant crystal face viewed down [001] and one minor face viewed down [100] are hydrophobic, whilst the minor face viewed along [010] is hydrophilic.

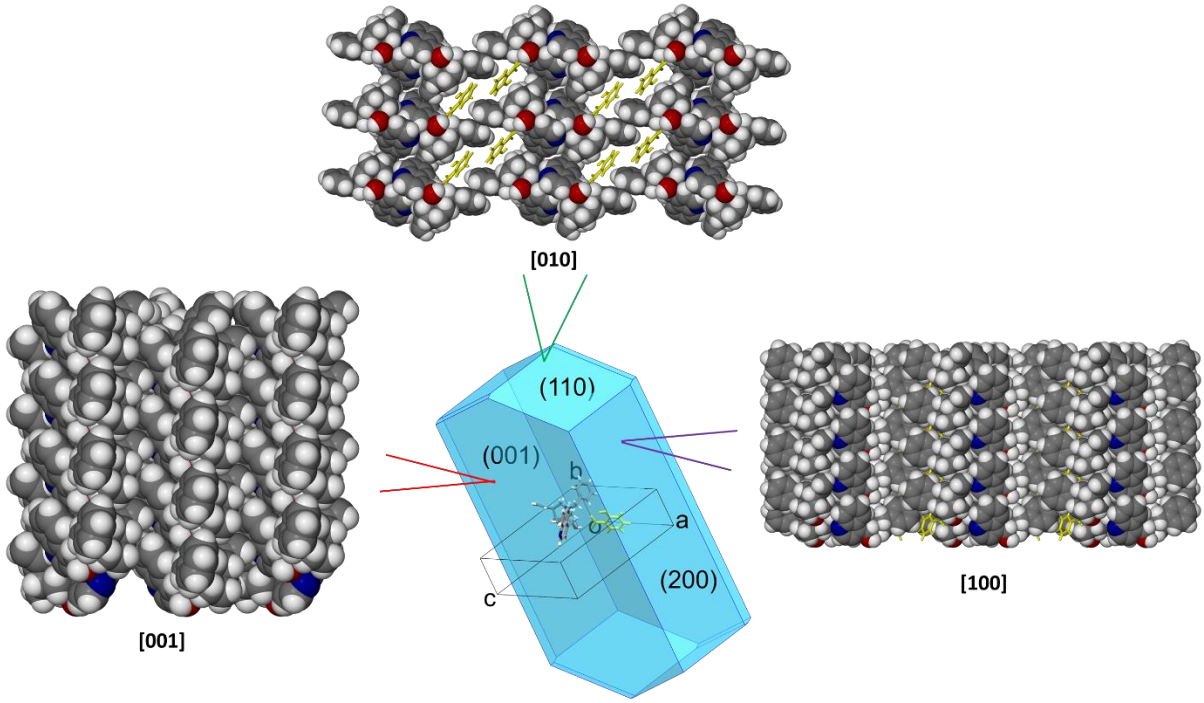

Figure 3.28 The calculated [NBCIND$^+$][SA$^-$] morphology and the packing along each face. The dominant crystal face viewed along [001] and the minor face viewed down [100] are hydrophobic, whilst the minor face along [010] is hydrophilic.

3.6 Structure-property relations

In addition to surface properties, some physicochemical properties of a crystalline material can be linked to the long-range ordered arrangements of their molecules. Therefore, manipulation of the ordered arrangement will result in the subsequent modification of the physical properties. The challenge is to carry out the manipulation in a tailored manner, ensuing intended physical properties.

The main force driving aggregation in the multicomponent crystals of salicylic acid and the cinchona alkaloids is charge assisted hydrogen bonds. At the same time, the weaker interactions also present a cumulative effect on physical properties of the crystals. Wood and co-workers[11] emphasized the importance of a visualisation tool to simultaneously visualise and analyse the intermolecular contacts in a crystal lattice. This has been achieved by the calculation of the Hirshfeld surfaces for the ion pairs, rather than for the SA or the alkaloid moiety. This decision was made based on observations of previous, related projects, when the existence of the ion pairs during dissolution was proven by ^{1}H NMR analysis.[12] This observation is also supported by the fact that the strong, charge assisted hydrogen bonds are formed only between the ions of the ion pairs, but not between the neighbouring ion pairs. Thus, the packing patterns were analysed by mapping d_{norm} onto the 3D Hirshfeld surfaces.

The contacts closer than the van de Waals separation are colour-coded red on the surfaces, and those greater than the van de Waals separation are coloured blue. The white regions are from contacts with the same separation as the van der Waals separation. The Hirshfeld surfaces mapped with d_{norm} for the cinchona alkaloid salicylate salts are shown in Figure 3.29.

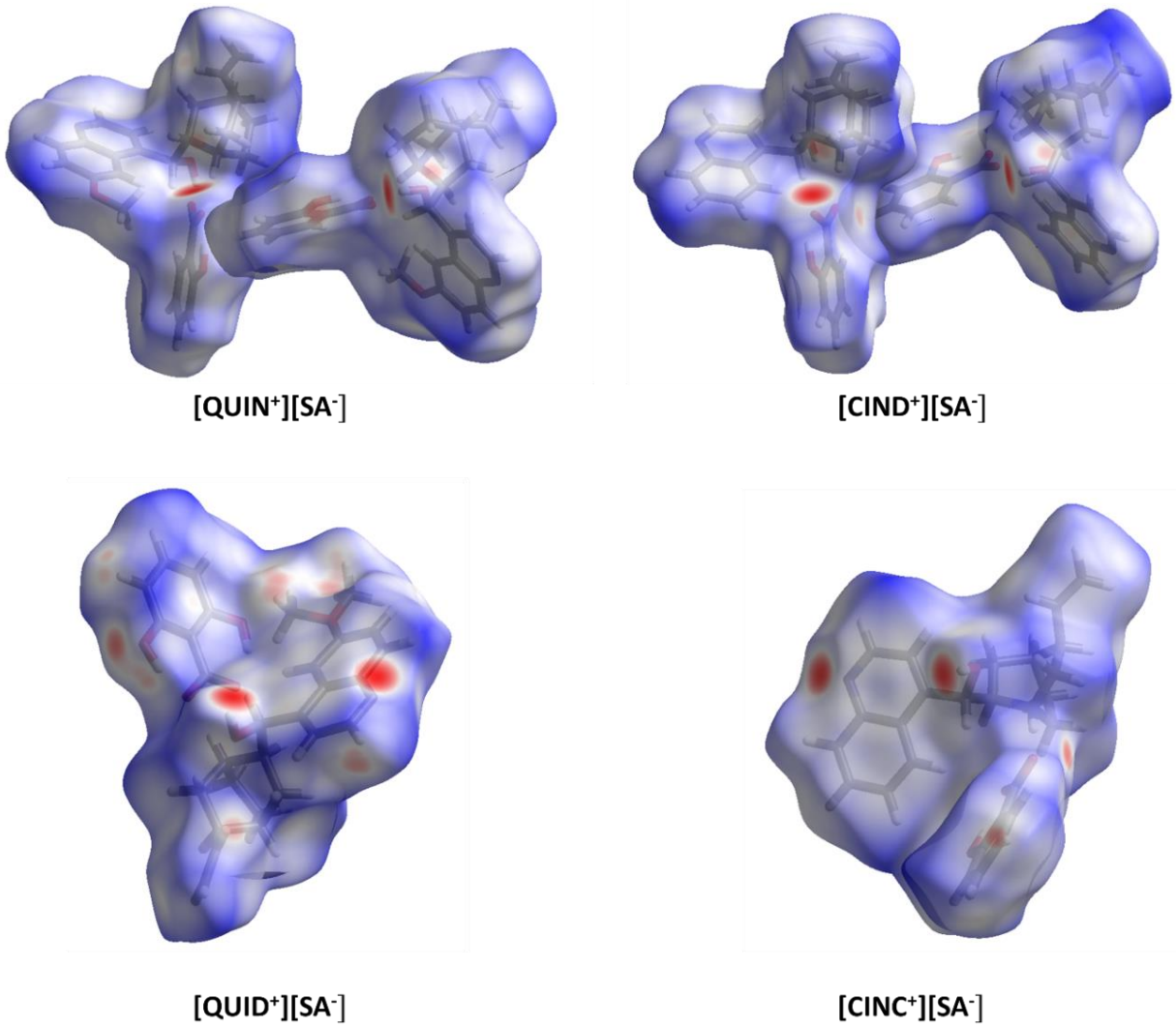

Figure 3.29 Hirshfeld surfaces mapped with d_{norm} for the cinchona alkaloid salicylates.

The Hirshfeld surfaces of the ion pairs in the salts with N-benzyl substituted cinchona alkaloids are shown in Figure 3.30. The effect of introducing a benzyl substituent on the crystal packing is not obvious from the visual analysis of the Hirshfeld surfaces. Thus, to get a better picture of the relationship between the observed physical properties (solubility and melting point) and the crystal structure, we analysed the intermolecular forces acting on the ion pairs in the crystal lattice. This was done by representing the complex 3D Hirshfeld surfaces as 2D fingerprint plots.

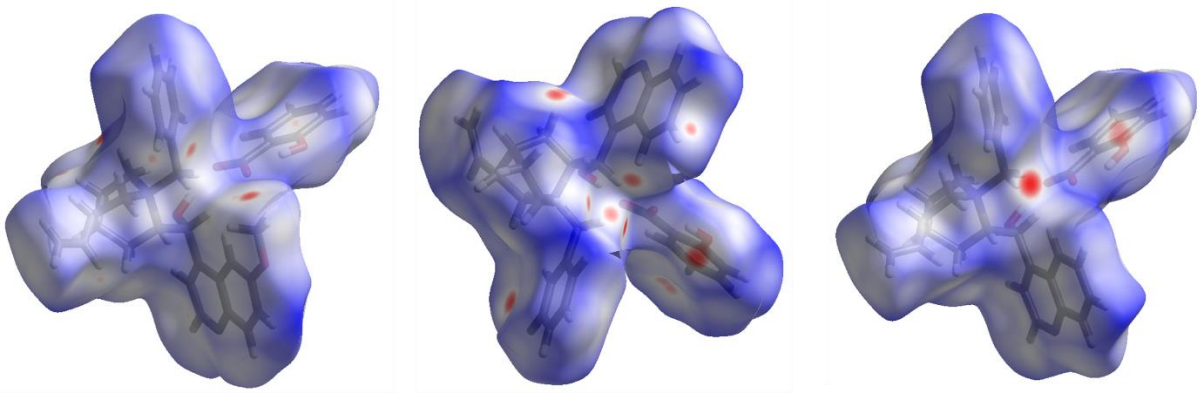

Figure 3.30 Hirshfeld surfaces mapped with d_{norm} for the N-benzylcinchona alkaloid salicylates.

3.6.1 Intermolecular interactions in unsubstituted cinchona alkaloid salicylates

The fingerprint plots of the ion pairs (i.e. *promolecule*) were generated to give an overview of their interactions with the crystal environment, or *procrystal* (Figure 3.31). Two plots were generated for [CIND$^+$][SA$^-$] and [QUIN$^+$][SA$^-$] for the two symmetry independent ion pairs in their asymmetric units. Spikes 1, 2, 3 and 4 represent H···H, O···H, C···H and N···H contacts, respectively. The comparable feature in all the fingerprint plots is the symmetrical shape, which is an indication of similar hydrogen bond donor and acceptor functions of the ion pairs.

The visual comparison of the fingerprint plots for the 6 ion pairs shows some significant differences. The least efficient packing is observed in [QUIN$^+$][SA$^-$], which is indicated by long-range H···H contacts (red circle in fingerprint plot). Similar effects can be seen on the plots of [CIND$^+$][SA$^-$] to a lesser extent. [QUID$^+$][SA$^-$] has a significant amount of short-range H···H contacts (spike 1), which can be interpreted as repulsive. The O···H (spike 2) and N···H (spike 4) interactions are due to stronger hydrogen bonds, and are considered as attractive. The prominent spike 2 in [CIND$^+$][SA$^-$] and [QUIN$^+$][SA$^-$], in the region 1.00 Å < (d_e + d_i) < 1.10 Å, is due to the O24-H24···O47 and O24-H24···O48 hydrogen bonds that hold the ion pairs together. In contrast, spike 4 in [CINC$^+$][SA$^-$] and [QUID$^+$][SA$^-$] with a d_e + d_i ≈1.2 corresponds to the O24-H24···N1 hydrogen bond between the ion pair dimers.

The wing feature present in all the 2D fingerprint plots, spike 3, indicates the presence of C···H interactions which correspond to C–H···π contacts. These contacts occur at much shorter distances in [CINC$^+$][SA$^-$] and [QUID$^+$][SA$^-$] with $d_e + d_i \leq 1.8$ than in [CIND$^+$][SA$^-$] and [QUIN$^+$][SA$^-$] ($d_e + d_i \geq 1.8$).

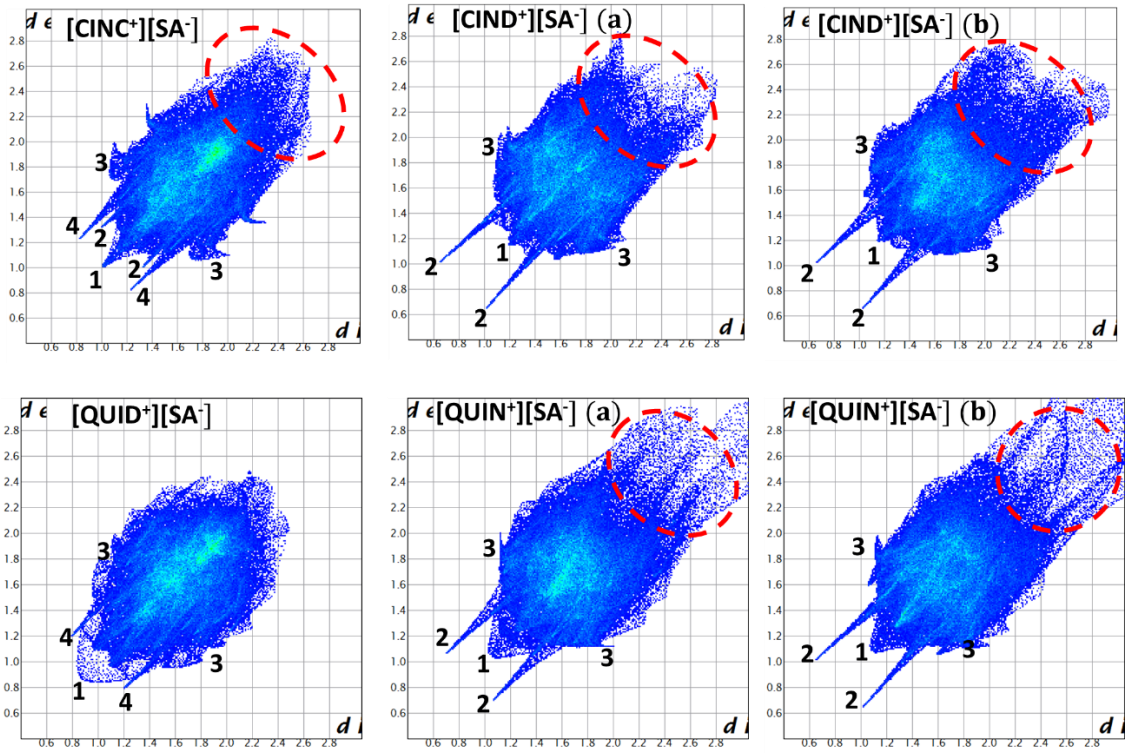

Figure 3.31 The 2D fingerprint plot representation of 3D Hirshfeld surface for unsubstituted cinchona alkaloid salicylates. Spikes 1, 2, 3 and 4 represent H···H, O···H, C···H and N···H contacts, respectively.

The percentage contributions of the H···H, O···H and C···H contacts to the Hirshfeld surface are summarised in Table 3.12 for the unsubstituted cinchona alkaloid salts. These percentage contributions were plotted together with the melting points and solubility (Figure 3.32). The solubility of the multicomponent crystals show dependence on the O···H interactions, with a correlation coefficient 91% (Figure A24). This observation supports the conclusion that the aqueous solubility of the salts is increasing with the % hydrophilic interactions formed by the ion pairs with their surroundings, and also agrees with the conclusion drawn from the morphology analysis in section 3.5.

Table 3.12 The percentage contributions of the H···H, O···H and C···H contacts to the Hirshfeld surface, and the melting points and solubility of the unsubstituted cinchona salicylate salts.

	[CINC$^+$][SA$^-$]	[CIND$^+$][SA$^-$]	[QUID$^+$][SA$^-$]	[QUIN$^+$][SA$^-$]
O···H (%)	10.9	13.3	13.4	14.8
H···H (%)	61.2	52.7	59.6	54.0
C···H (%)	17.0	27.4	17.0	22.6
N···H (%)	4.0	5.4	3.9	5.2
C···C (%)	5.9	0.8	5.0	1.1
Solubility(mg/mL)	0.2234	0.2015	0.1825	0.1654
MP (°C)	172.2	207.8	222.2	202.2

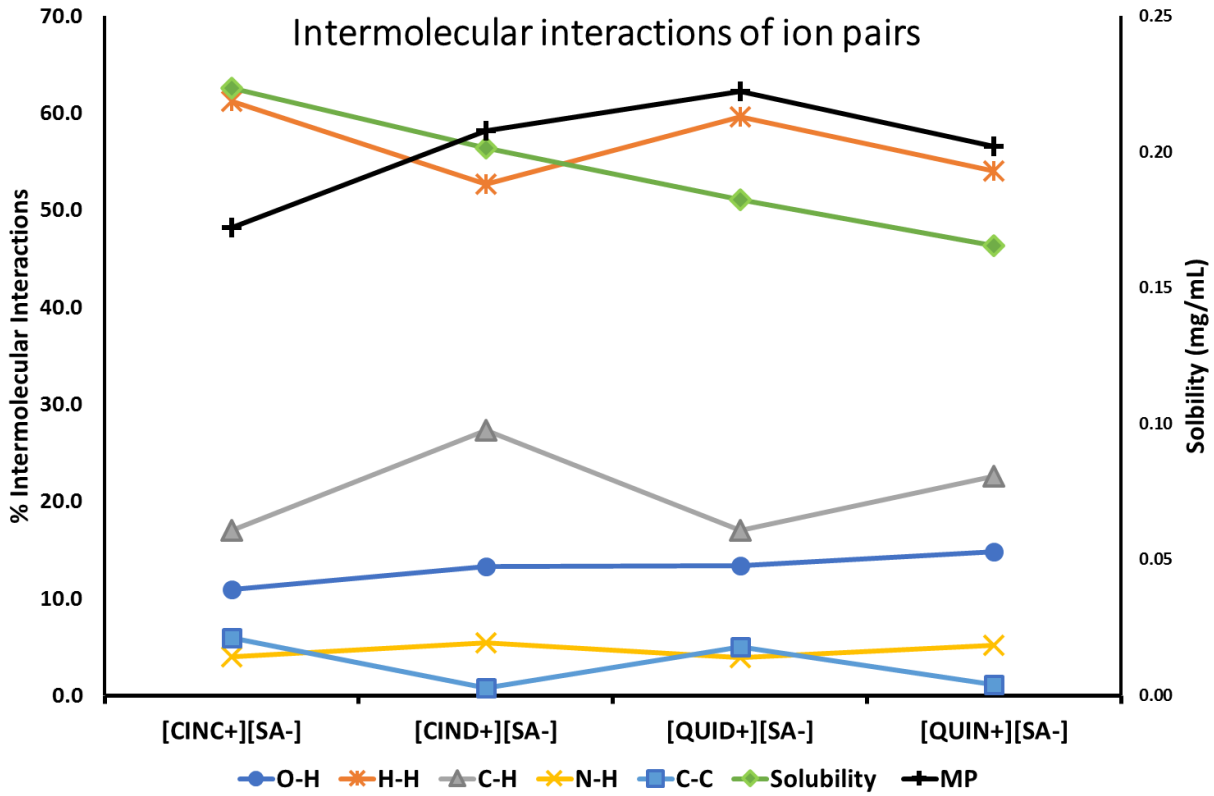

Figure 3.32 The percentage intermolecular interactions in the unsubstituted cinchona alkaloid salicylates plotted against solubility and melting point.

3.6.2 Intermolecular interactions in N-benzylcinchona cinchona alkaloid salicylates

On addition of a benzyl substituent to the cinchona alkaloids, the fingerprint plots of the resulting multicomponent crystals show significant differences to their unsubstituted counterparts (Figure 3.33). Similarly to the unsubstituted cinchona alkaloids fingerprint plots, the benzyl substituted cinchona alkaloid fingerprint plots are also very symmetrical. The obvious difference is the lack of formation of strong hydrogen bonds between these ion pairs. The [NBQUIN$^+$][SA$^-$] presents the highest solubility and is the most loosely packed, as indicated by long range H···H contacts (red circle in fingerprint plot). Subsequent reduction in solubility of [NBCINC$^+$][SA$^-$] and [NBCIND$^+$][SA$^-$] can be attributed to a more efficient packing, i.e. less long-range contacts on the fingerprint plots. The disparity in rate of dissolution between [NBCINC$^+$][SA$^-$] and [NBCIND$^+$][SA$^-$] can be attributed to the presence of O···H contacts (spike 2) at shorter distances ($d_e + d_i \approx 1.2$) in the latter structure.

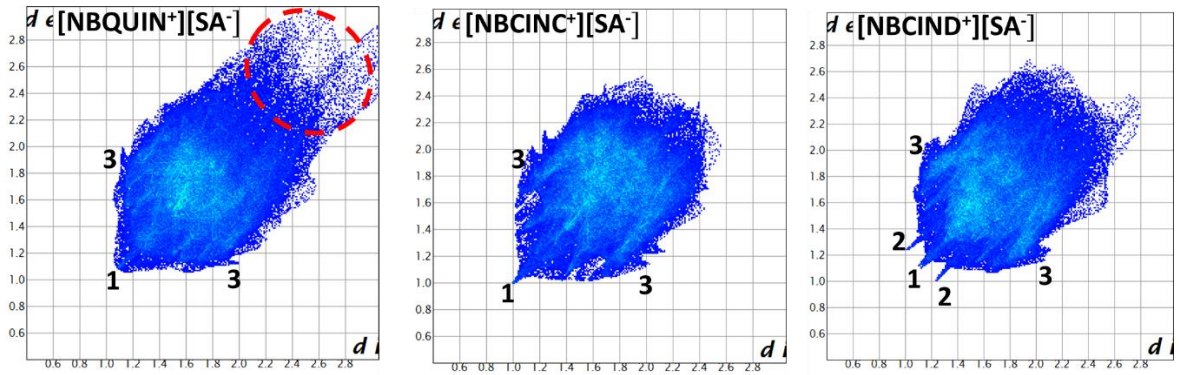

Figure 3.33 The 2D fingerprint plot representation of 3D Hirshfeld surface for the N-benzylcinchona alkaloid salicylates.

The percentage contributions of the H···H, O···H and C···H contacts to the Hirshfeld surface are summarised in Table 3.13 and the percentage contributions (with the melting points and solubility) are presented in Figure 3.34. In these crystals the solubility exhibits an inverse relationship to the C···H interactions with a correlation of 97% (Figure A25), while the O···H interactions do not correlate well with the change of the solubility. This diminished importance of the O···H interactions can be linked to the additional benzyl group that is blocking the polar section of the ion pair from forming further interactions with the procrystal. As a result of the additional benzyl group, the ion pairs became less polar and the solubility of the N-benzylcinchona alkaloid salicylates is governed by the hydrophobic interactions.

Table 3.13 The percentage contributions of the H···H, O···H and C···H contacts to the Hirshfeld surface, and the melting points and solubility of the benzyl substituted cinchona alkaloid salicylate salts.

	[NBQUIN$^+$][SA$^-$]	[NBCINC$^+$][SA$^-$]	[NBCIND$^+$][SA$^-$]
O···H (%)	11.6	12.1	11.1
H···H (%)	54.0	54.0	53.6
C···H (%)	26.4	27.8	29.9
N···H (%)	4.3	4.5	4.5
C···C (%)	0.6	1.6	0.6
Solubility(g/L)	0.1143	0.1046	0.0786
MP (°C)	207.2	207.5	213.5

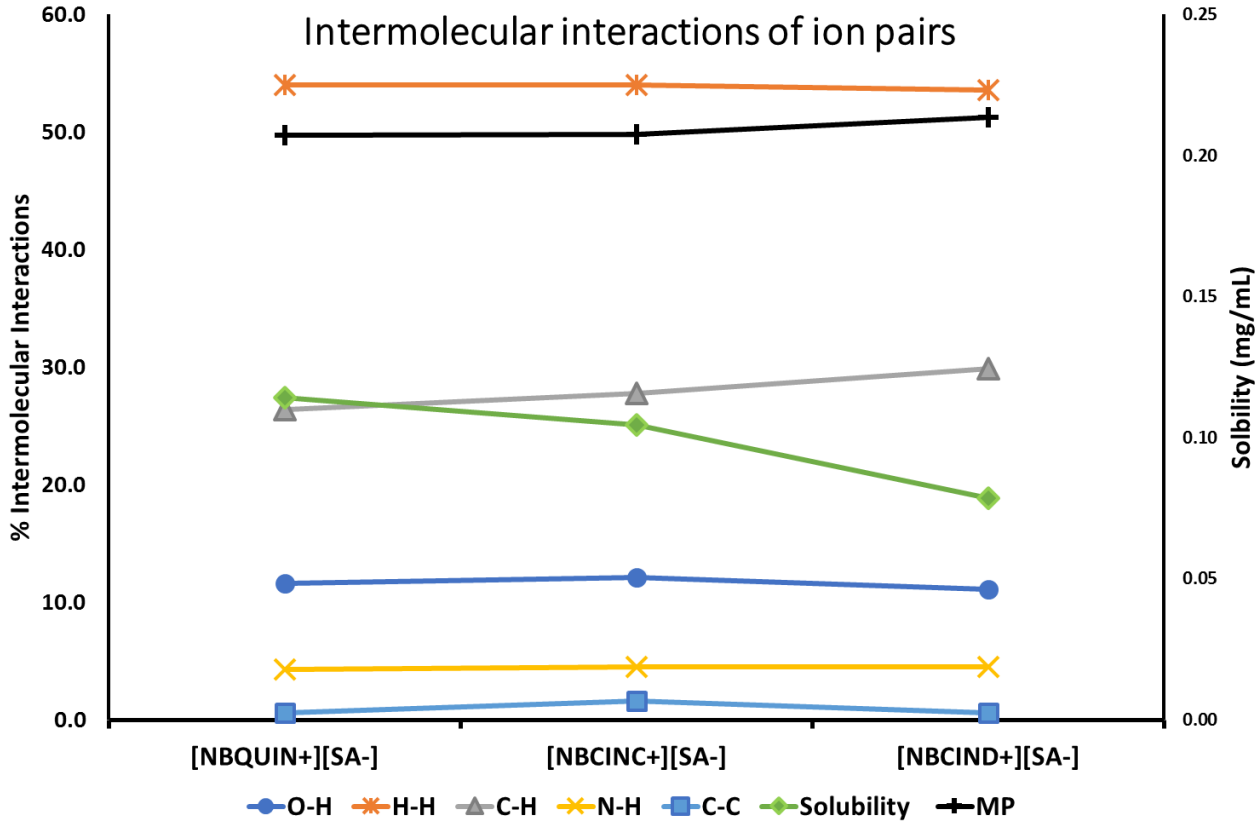

Figure 3.34 The percentage intermolecular interactions in the N-benzylcinchona alkaloid salicylates plotted against solubility and melting point.

3.7 References

1. A. J. Cruz-Cabeza, *CrystEngComm*, 2012, **14**, 6362-6365.
2. M. C. Etter, *Accounts of Chemical Research*, 1990, **23**, 120-126.
3. S. L. Childs, P. A. Wood, N. Rodríguez-Hornedo, L. S. Reddy and K. I. Hardcastle, *Crystal Growth & Design*, 2009, **9**, 1869-1888.
4. P. A. Wood, M. A. Oliveira, A. Zink and M. B. Hickey, *CrystEngComm*, 2012, **14**, 2413-2421.
5. W. Clegg, *Crystal Structure Analysis: Principles and Practice*, Oxford University Press, 2001.
6. S. Ghosh, M. K. Mishra, S. Ganguly and G. R. Desiraju, *Journal of the American Chemical Society*, 2015, **137**, 9912-9921.
7. O. D. Putra, T. Furuishi, E. Yonemochi, K. Terada and H. Uekusa, *Crystal Growth & Design*, 2016, **16**, 3577-3581.
8. A. Bravais, *Etudes cristallographiques*, Gauthier-Villars, 1866.
9. G. Friedel, *Bull. Soc. Fr. Mineral*, 1907, **30**, 326-455.
10. J. D. H. Donnay and D. Harker, *Am. Mineral*, 1937, **22**, 446-467.
11. P. A. Wood, J. J. McKinnon, S. Parsons, E. Pidcock and M. A. Spackman, *CrystEngComm*, 2008, **10**, 368-376.
12. N. B. Báthori, L. R. Nassimbeni and C. L. Oliver, *Chemical Communications*, 2011, **47**, 2670-2672.

Chapter 4

Quininium acetylsalicylate

4.1 Quininium acetylsalicylate [QUIN$^+$][ASA$^-$]

In the previous chapter it was shown that systematic modification of the solubility of salicylic acid is possible when the API is cocrystallized with a series of cinchona alkaloids. The solubility of the highly soluble drug was tuned via forming multicomponent crystals with less polar coformers. It was concluded that on the molecular level the flexible benzyl moiety of the substituted cinchona alkaloids is shielding the carboxylate moiety, and eventually causing the decrease of the polarity for the ion pair. This leads to the observed decrease of dissolution rate of the drug in an aqueous environment. After the successful application of SA in the systematic study, our interest turned to aspirin (acetylsalicylic acid, ASA), a SA analogue. Aspirin not only has high aqueous solubility but also gradually hydrolyses when in contact with moisture. This may cause difficulties during storage and decrease the shelf life of the product. Thus, stabilizing aspirin via multicomponent crystal formation was the aim of this section of the project.

Single crystals of [QUIN$^+$][ASA$^-$] were successfully grown using the solvent evaporation method (SE) from acetone. The crystallographic data and refinement parameters are summarised in Table 4.1. Thus far, further attempts to regrow these crystals in solution have failed; instead the hydrolytic product of ASA was captured in the form of quininium salicylate ([QUIN$^+$][SA$^-$]). Therefore, the mechanochemical method, specifically liquid assisted grinding (LAG), was used to synthesize the required solid form. The molecular structure of acetyl salicylic acid (API) and quinine (coformer) are given in Figure 4.1 and the crystal structure, green synthesis, thermal analysis and powder X-ray analysis of the multicomponent crystalline material will be discussed in this chapter.

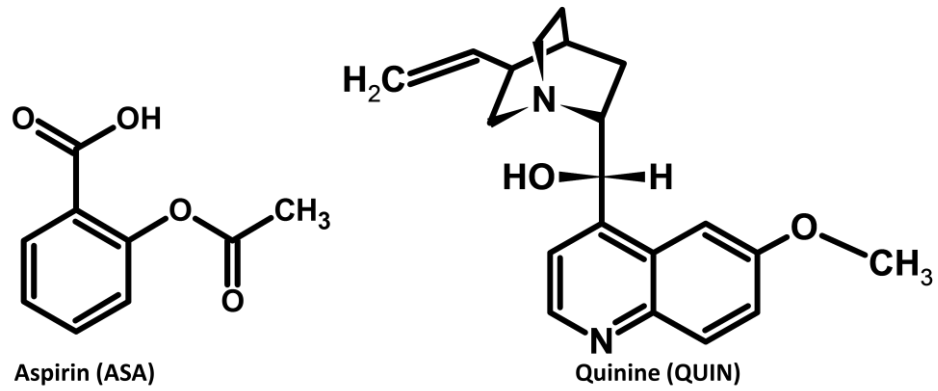

Figure 4.1 The molecular line diagram of acetylsalicylic acid (API) and quinine (coformer).

Table 4.1 Crystallographic data and refinement parameters for quininium acetylsalicylate.

	[QUIN$^+$][ASA$^-$]
Molecular formula	$C_{29}H_{32}N_2O_6$
Molecular weight (g mol^{-1})	504.57
Crystal system	orthorhombic
Space group	$P2_12_12_1$
a/Å	8.6571(3)
b/Å	9.6894(3)
c/Å	30.6794(11)
α/°	90
β/°	90
γ/°	90
Volume/Å^3	2573.45(15)
Z, Z′	4/1
ρ (calc.)/ mg m^{-3}	1.302
μ(MoKα)/ mm^{-1}	0.091
F(000)	1072.0
Crystal size (mm)	0.1×0.1×0.1
Temperature (K)	173(2)
Radiation [Å]	0.71073
Theta min-max [°]	2.204, 28.274
Dataset	-7:11, -12:12, -39:40
Final R indices [I> 2.0 sigma (I)]	R1= 0.0434, wR2= 0.0940
R indices (all data)	R1= 0.0613, wR2= 0.1020
Tot., uniq. data, R (int)	6391, 5090, 0.0416
N_{ref}, N_{par}	6391, 338
S	1.021
Max.and av. Shift/error	0.00, 0.00
Min. and max. resd. dens. (Å^3)	-0.170, 0.219

The quininium acetylsalicylate, [QUIN$^+$][ASA$^-$], structure was solved in the orthorhombic space group $P2_12_12$ with one quininium ion and one acetylsalicylate ion in the asymmetric unit. The hydrogen bond parameters are shown in Table 4.2. Based on bond length analysis and allocation of the hydrogen (H11) on the quinuclidine ring from the difference Fourier map, it was concluded that [QUIN$^+$][ASA$^-$] is a salt (Figure 4.2). Proton transfer was as expected because the calculated ΔpK_a was greater than 4 (pK_a QUIN (9.69)- pK_a ASA (3.41) = 6.28).

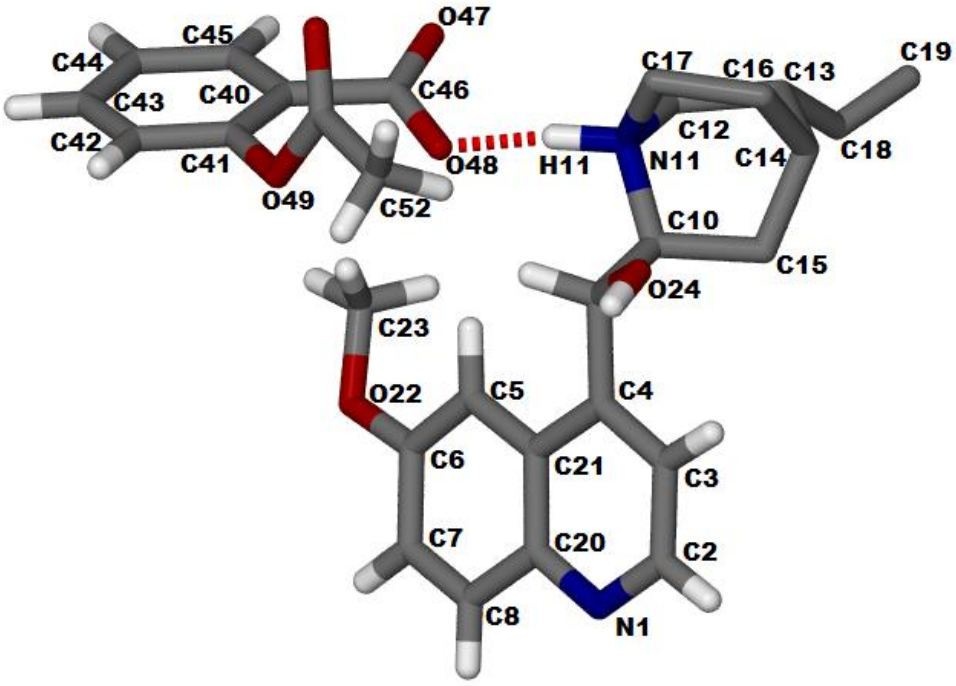

Figure 4.2 Asymmetric unit showing the labelled heavy atoms and the N$^+$-H···O$^-$ interaction between the quininium and the acetylsalicylate ion (quinuclidine ring hydrogens are omitted for clarity).

Table 4.2 Hydrogen bond and short contact matrices of [QUIN$^+$][ASA$^-$]

D-H···A	D-H (Å)	H···A (Å)	D···A (Å)	∠D-H···A (°)
N11-H11···O48	1.00	1.62	2.597	167.3
O24-H24···N1^{i}	0.84	2.01	2.840	167.4
N11-H11···O47	1.00	2.65	3.439	136.3
C9-H9···O48	1.00	2.48	3.273	135.7
C10-H10···O51^{ii}	1.00	2.59	3.470	147.5
C16-H16A···O47^{iii}	0.99	2.54	3.288	132.0
C23-H23B···O24i^{v}	0.98	2.60	3.493	152.3
Symmetry codes	(i) [x-1/2,-y+3/2,-z+1] (ii) [x+1,y,z] (iii) [-x,y+1/2,-z+1/2] (iv) [x,y-1 z]			

The crystal packing is characterised by chains which are mediated by intermolecular O24-H24···N1 (2.84 Å, 167.4°) hydrogen bonds forming $C_1^1(7)$ chains in a zigzag pattern along [100]; (Figure 4.3). The quinoline rings that form the backbone of the zigzag motif resemble a herringbone pattern. The acetylsalicylate ions intercalate between the trenches of the hydrogen bonded backbone via N11-H11···O48 (2.60 Å, 167.3°). The neighbouring zigzag chains interact via van der Waals interactions, forming seemingly rectangular voids, which are occupied by the acetylsalicylic acid ions, (Figure 4.4). The packing of the $QUIN^+$ ions are more compact when viewed down [100]; (Figure 4.5).

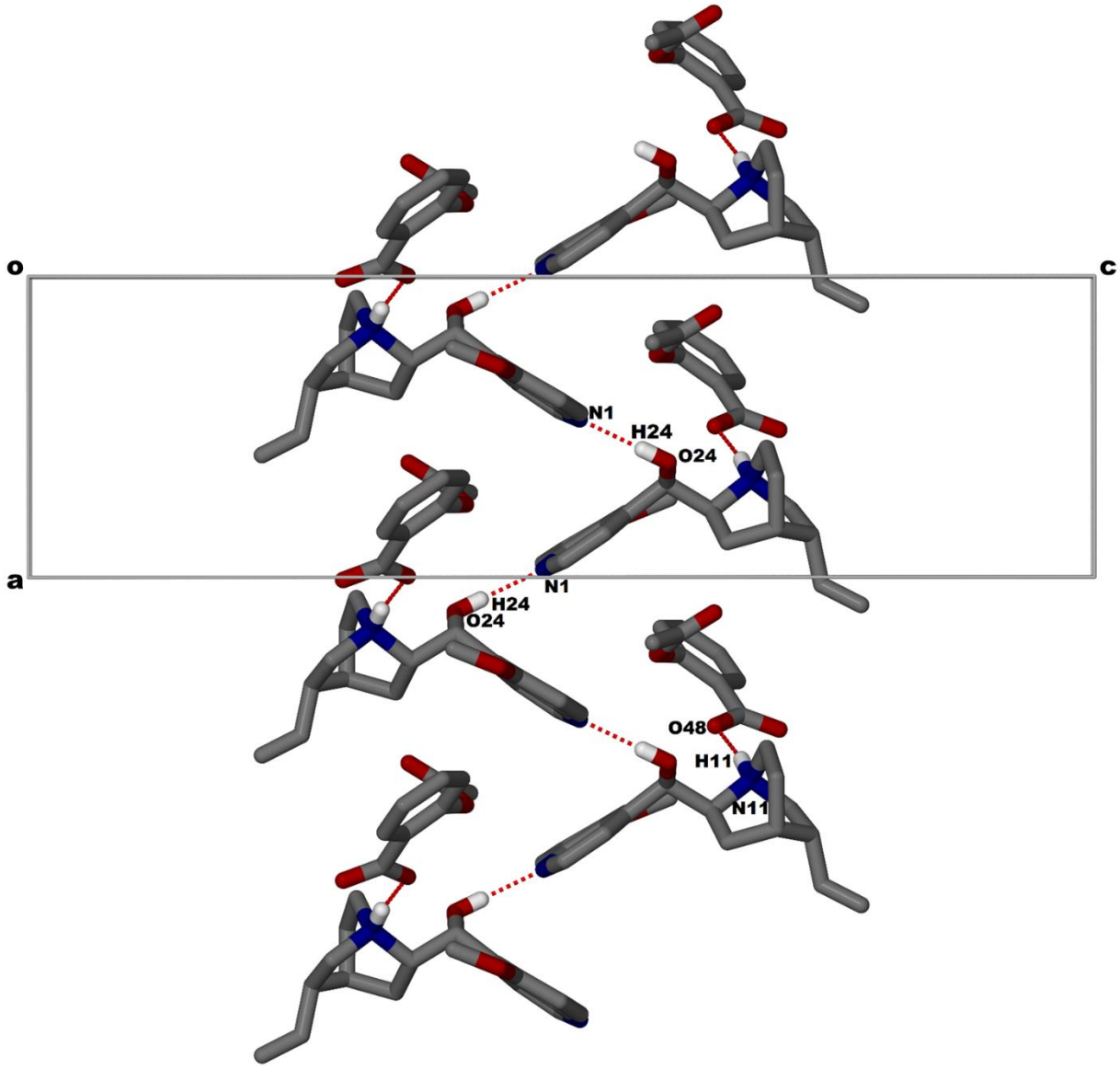

Figure 4.3 Hydrogen bond patterns in [$QUIN^+$][ASP^-] chains down [100] (hydrogens not participating in hydrogen bonding have been omitted for clarity).

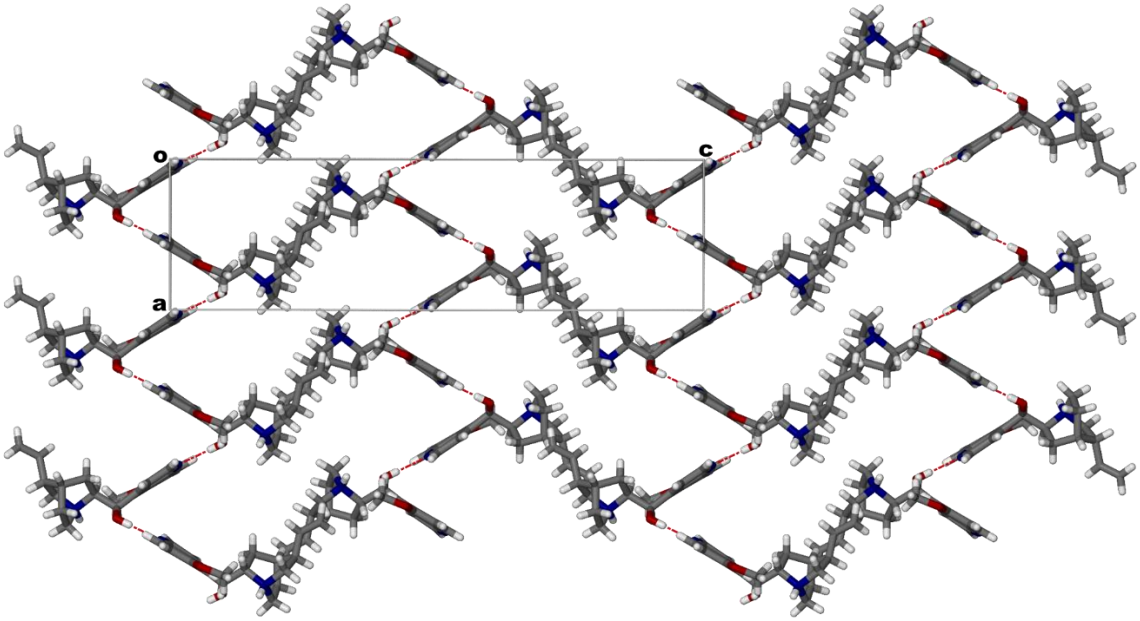

Figure 4.4 Rectangular voids formed by interactions of neighbouring chains (ASA is omitted for clarity, view down [010]).

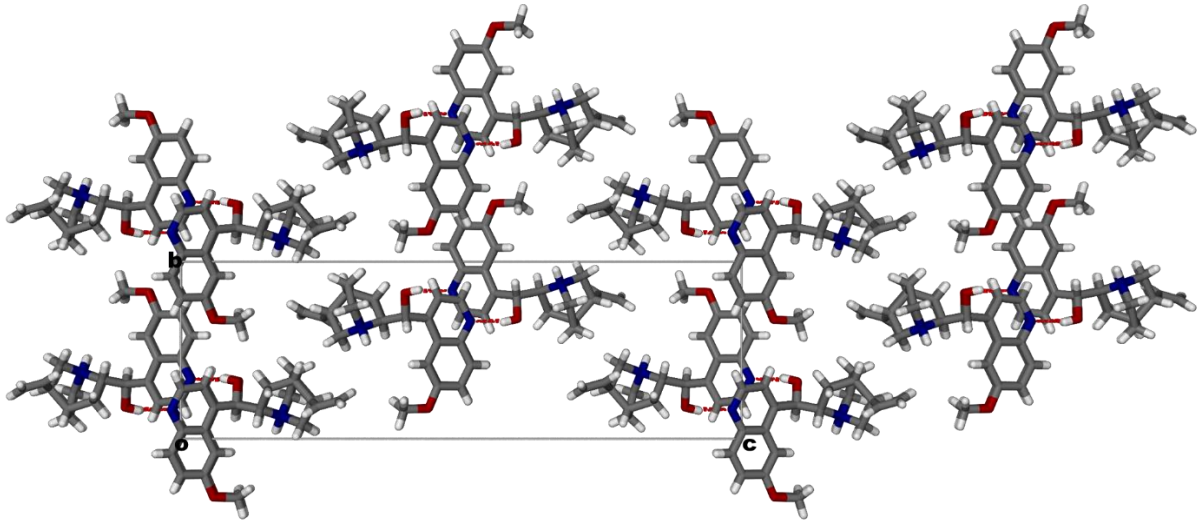

Figure 4.5 Packing in [QUIN$^+$][ASP$^-$] showing the stacking of the chains (ASA is omitted for clarity, view down [100]).

4.2 Bulk property analysis of [QUIN$^+$][ASA$^-$]

Differential scanning calorimetry was used to determine the melting point of the crystals obtained from solvent crystallisation and from liquid assisted grinding experiments to confirm the bulk property. From solvent evaporation, the resulting crystals of quininium acetylsalicylate had a melting endotherm (Figure 4.6, green) with an onset temperature (T_{onset}) of 153.72 ^oC and a peak (T_{peak}) of 162.3 ^oC. The melting point of the salt is higher than the melting point of acetylsalicylic acid (T_{onset} =137.01^oC, T_{peak}=142.3 ^oC), but lower than the melting point of quinine (T_{onset} = 176.4 ^oC, T_{peak}= 178.3 ^oC).

After many unsuccessful crystallisation attempts, liquid assisted grinding of the two starting materials resulted in the formation of [QUIN$^+$][ASA$^-$]. ASA and QUIN were ground together using both hand grinding and an in-house mechanical grinder. In both cases a few drops of acetonitrile were added. The in-house mechanical grinder gave better conversion of the starting materials; thus this product was identified with the aid of DSC and PXRD. The LAG product's melting endotherm (T_{onset} = 150.8 ^oC, T_{peak}= 157.1 ^oC) shows excellent match with the product from the solvent crystallisation (Figure 4.6).

Powder X-ray analysis was employed to prove that the SCXRD structure obtained via SE was representative of the material obtained from LAG. The PXRD pattern generated from the single crystal (Figure 4.7, purple) agrees well with the product obtained from LAG (Figure 4.7, green) proving that the salt can be prepared mechanochemically. However, there is a peak at 16° in 2θ (Figure 4.7, red arrow) that can be associated with the starting material QUIN, suggesting that conversion may not be 100%.

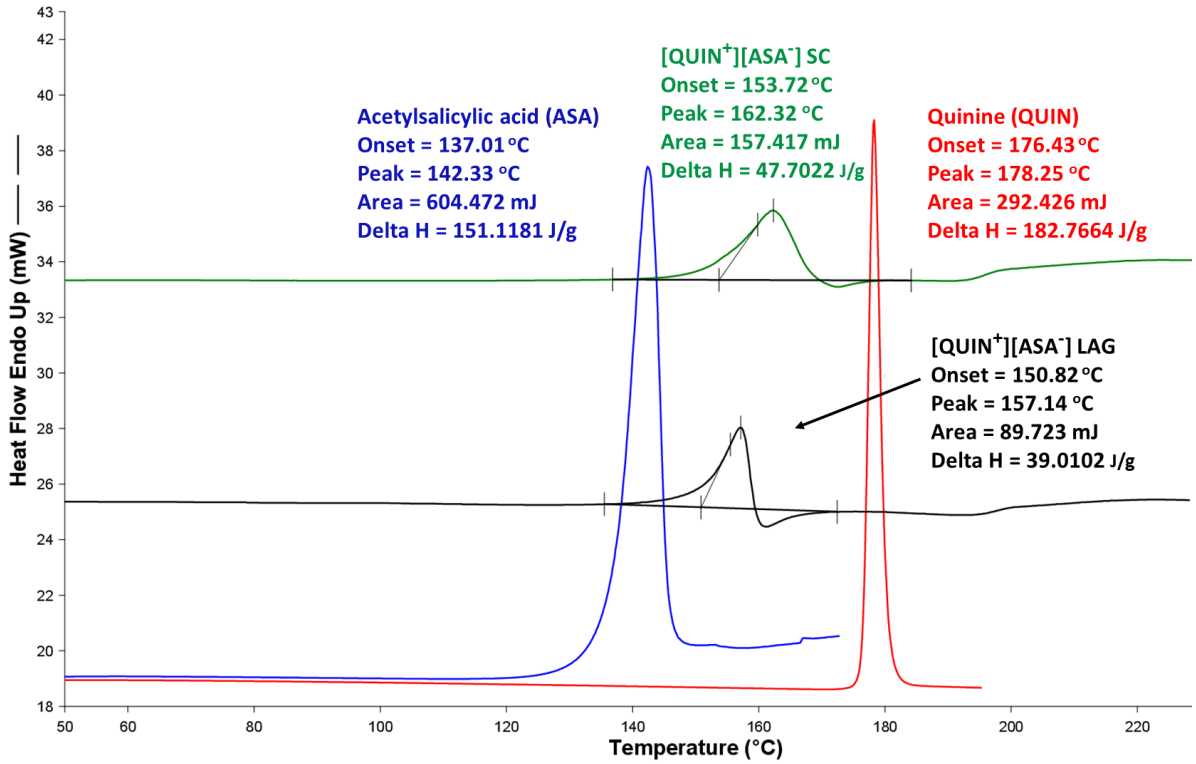

Figure 4.6 DSC curves for ASA, QUIN, and products of solvent evaporation and liquid assisted grinding experiments of [QUIN⁺][ASA⁻].

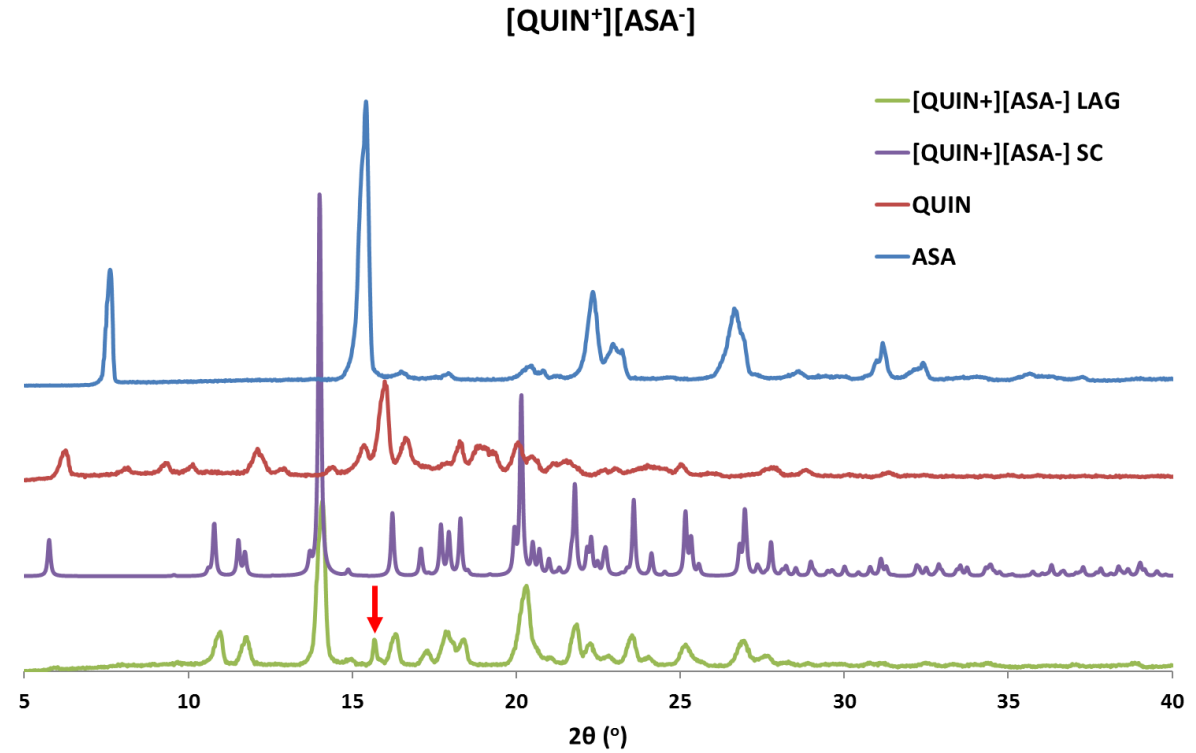

Figure 4.7 PXRD patterns of ASA (blue), QUIN (red), [QUIN⁺][ASA⁻] generated from single crystal data (purple) and [QUIN⁺][ASA⁻] of obtained via LAG (green).

4.3 Dissolution of [QUIN$^+$][ASA$^-$]

The rate of dissolution of [QUIN$^+$][ASA$^-$] and ASA in water was measured using HPLC-MS. The cumulative concentrations are summarised in Table A4. As indicated in the dissolution profile given in Figure 4.8, the rate of dissolution of the multicomponent crystal is lower than that of pure aspirin.

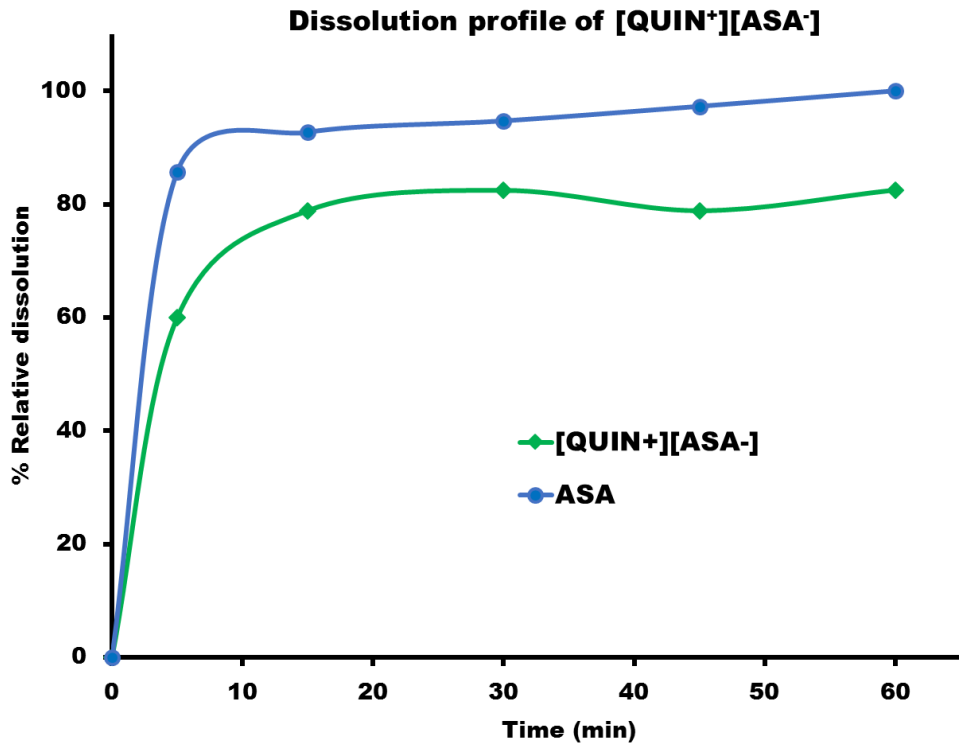

Figure 4.8 First hour dissolution profile of ASA and [QUIN$^+$][ASA$^-$]

In the same way as the cinchona alkaloid salicylates, the incorporation of the hydrophobic cinchona alkaloid into the crystal lattice of aspirin has successfully reduced the rate of release of the drug. However, to completely rationalise this observation, synthesis of more multicomponent crystals of ASA with other cinchona alkaloids and further investigation is required. Since the only difference in the structures of [QUIN$^+$][ASA$^-$] and [QUIN$^+$][SA$^-$] is the additional acetyl group on ASA, Hirshfeld analysis was carried out to investigate whether any similarities or differences in their interactions would explain the similar trend of reduced rate of dissolution. The 2D fingerprint plots for the ion pair of [QUIN$^+$][ASA$^-$] and [QUIN$^+$][SA$^-$] are shown in Figure 4.9, where spikes 1, 2, 3 and 4 represent H···H, O···H, C···H and N···H contacts, respectively. [QUIN$^+$][ASA$^-$] is more efficiently packed compared to [QUIN$^+$][SA$^-$], as indicated by the presence of long range H···H contacts in the latter structure (Figure 4.9, red circles).

In addition, the major interactions holding the ion pairs in [QUIN$^+$][ASA$^-$] are N···H contacts (spike 4), whilst in [QUIN$^+$][SA$^-$] the ion pairs bonded through O···H contacts (spike 2). The quantitative comparison of the percentage contribution of the intermolecular interactions is summarized in Figure 4.10. It is interesting to note that the % contribution from the H···H, N···H and C···C contacts are very similar in the two structures, but [QUIN$^+$][ASA$^-$] has ca. 5 % more O···H interactions. This is a logical outcome since ASA has an extra acetyl substituent.

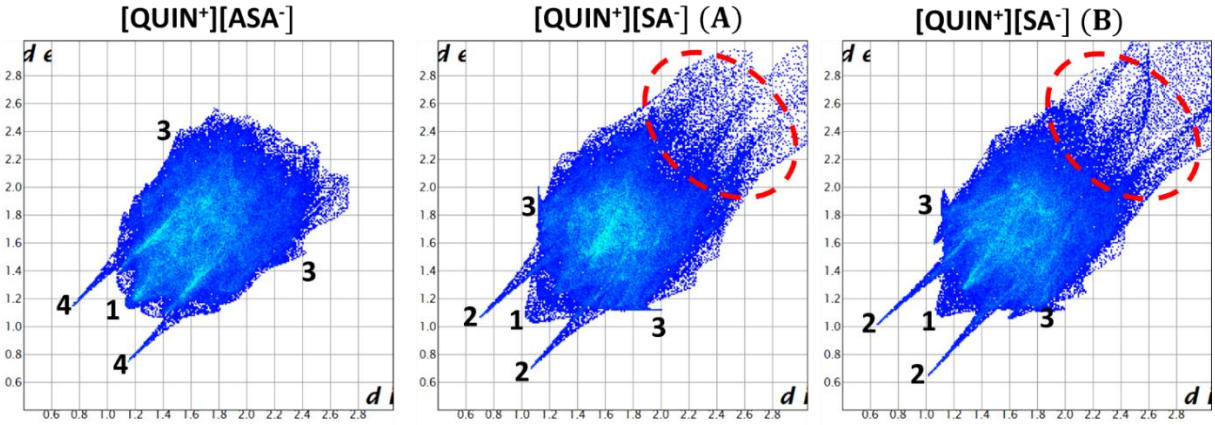

Figure 4.9 Fingerprint plots of [QUIN$^+$][ASA$^-$], [QUIN$^+$][SA$^-$] molecule A and [QUIN$^+$][SA$^-$] molecule B, with 1, 2, 3 and 4 representing H···H, O···H, C···H and N···H contacts respectively.

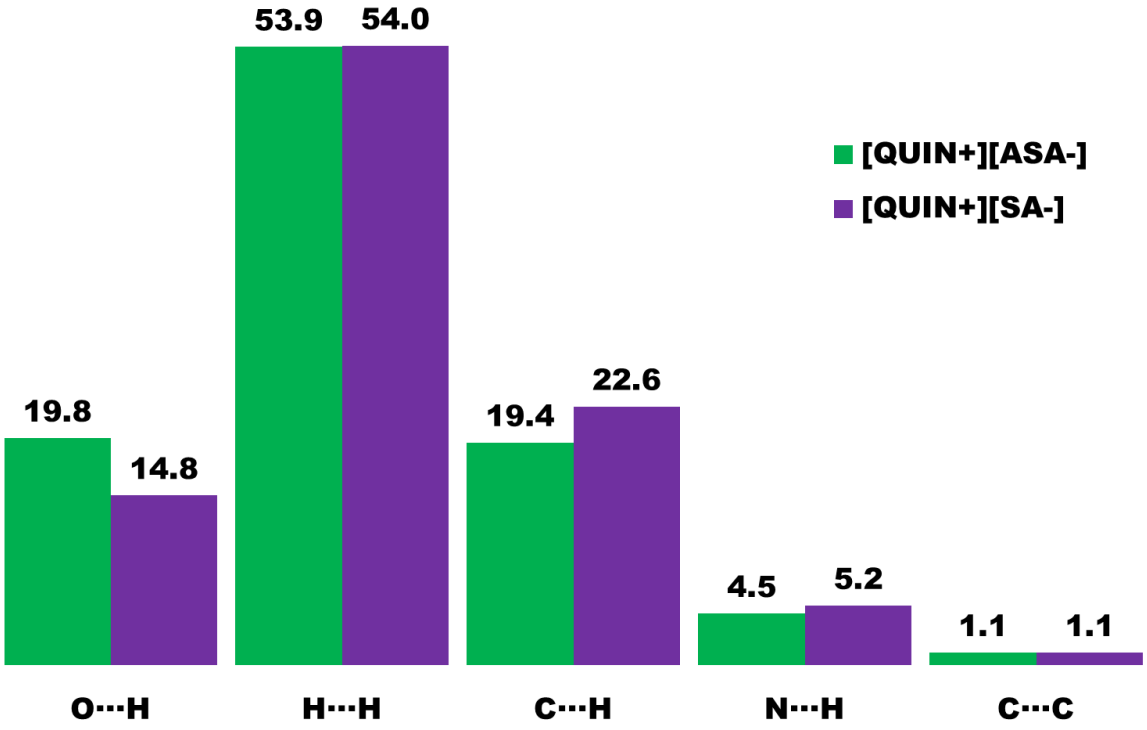

Figure 4.10 Summary of the percentage contributions of the different interactions in [QUIN$^+$][ASA$^-$] and [QUIN$^+$][SA$^-$].

Chapter 5

Summary and conclusion

Summary and conclusion

Considering the poor biopharmaceutical properties associated with a significant number of pharmaceutics, it is essential to find suitable strategies to alter these physicochemical properties. The objective of the research presented here was: (i) to systematically influence the rate of dissolution of salicylic acid (SA) and aspirin (acetylsalicylic acid, ASA), (ii) to investigate the possibility of forming drug-drug multicomponent crystals with enhanced properties relative to the parent APIs, and (iii) investigate the advantages of mechanochemistry for the synthesis of multicomponent crystals that are difficult to attain using solution methods.

We reported the formation of seven multicomponent crystals of SA with quinidine [$QUID^+$][SA^-], quinine [$QUIN^+$][SA^-], cinchonine [$CINC^+$][SA^-], cinchonidine [$CIND^+$][SA^-], N-benzylquininium chloride [$NBQUIN^+$][SA^-], N-benzylcinchoninium chloride [$NBCINC^+$][SA^-], and N-benzylcinchonidinium chloride [$NBCIND^+$][SA^-]. The formation of these novel solid forms was confirmed by SCXRD, PXRD, DSC and TGA. The crystal structures of [$CINC^+$][SA^-], [$CIND^+$][SA^-], [$QUID^+$][SA^-] and [$QUIN^+$][SA^-] are characterised by a proton transfer from the acid to the quinuclidine ring of the cinchona alkaloid forming the N^+-H···O^- charge assisted hydrogen bond. In the crystal structures of [$NBCINC^+$][SA^-], [$NBCIND^+$][SA^-] and [$NBQUIN^+$][SA^-] the characteristic interaction between the ion pairs is the formation of the O-H···O^- charge assisted hydrogen bond.

The aim was to systematically influence the rate of dissolution of SA using crystal engineering principles. The rate of dissolution of SA, measured in an aqueous media using LC-MS, shows an approximate 50% and 75% decrease for the unsubstituted cinchona alkaloid salicylates and N-benzylcinchona alkaloid salicylates, respectively (Figure 5.1). The molecular configurations at the surfaces of the multicomponent crystals have a relationship to the rate of dissolution. The disparate rate of dissolution between the cinchona alkaloid salicylates and N-benzylcinchona alkaloid salicylates was attributed to increased hydrophobic groups, which encapsulated the polar groups present.

Hirshfeld surfaces of the ion pairs were calculated for all crystal structures and the related fingerprint plots were generated. As a qualitative comparison of the structures, the shapes of the fingerprint plots were compared. Furthermore, to understand how the intermolecular interactions influenced the rate of dissolution, the percentage contributions of the various intermolecular interactions were plotted together with the melting points and solubility. For the unsubstituted cinchona alkaloids, the solubility showed a dependence on the O···H interactions. This observation supports the conclusion that the aqueous solubility of the salts increases with the % hydrophilic interactions formed by the ion pairs. In contrast, the solubility of the substituted cinchona alkaloid salicylates displays an inverse relationship to the C···H interactions. This indicated that the solubility of the N-benzylcinchona alkaloid salicylates is governed by the hydrophobic interactions. These deductions led us to conclude that the rate of dissolution can be influenced by methodically adding additional hydrophobic groups on the coformer.

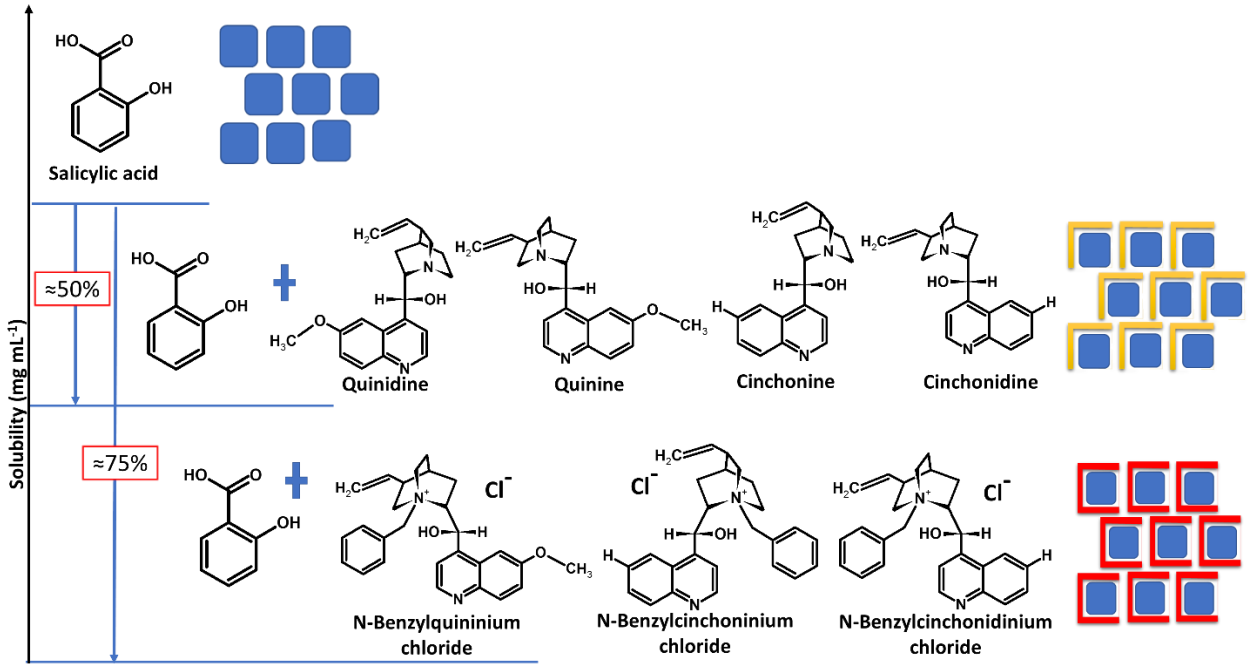

Figure 5.1 Successful control of the rate of dissolution of salicylic acid through cocrystallisation.

In the second section of the work, aspirin (ASA), an SA analogue was studied. Similarly to SA, ASA has high aqueous solubility and in addition, gradually hydrolyses when in contact with moisture. A 1:1 salt of quinine and aspirin [$QUIN^+$][ASA^-] was successfully prepared using solution methods and liquid assisted grinding. The salt exhibited physicochemical properties different from the parent drugs, and had a reduced rate of dissolution. The improved physicochemical properties were rationalised with the analysis of the crystal packing with the aid of Hirshfeld surfaces. The importance of liquid assisted grinding was presented further on, when attempts of solution crystallisation have failed to produce more [$QUIN^+$][ASA^-].

We believe that the findings of this work are a significant contribution to the field of supramolecular chemistry and pharmaceutical research, namely to the understanding of the selection of the coformers for cocrystallisation experiments, and their effect on the physicochemical properties of the multicomponent crystals. With the example of [$QUIN^+$][ASA^-] it was shown that mechanochemistry can be utilised to synthesize multicomponent crystals that are difficult to attain using solution methods. This work is being further investigated with the preparation and analysis of salts of ASA with the remaining cinchona alkaloids.

Appendix

Table A1 Measured Torsion Angles

	[CINC$^+$][SA$^-$]	[CIND$^+$][SA$^-$]		[QUIN$^+$][SA$^-$]		[QUID$^+$][SA$^-$]
		A	B	A	B	
C3-C4-C9-024	31.16	-16.38	-18.81	-17.78	-18.41	26.96
024-C9-C10-N11	62.68	-80.8	-80.17	-80.34	-74.72	61.91
C14-C13-C18-C19	-116.51	-116.35	-104.63	-127.73	-130.58	-108.13
C7-C6-022-C23	–	–	–	-177.48	-178.81	4.45/-149.63
N11-C25-C26-C27	–	–	–	–	–	–

	[NBCINC$^+$][SA$^-$]	[NBCIN$^+$] [SA$^-$]	[NBQUIN$^+$][SA$^-$]	[QUIN$^+$][ASA$^-$]
C3-C4-C9-024	11.16	-18.51	-17.74	-22.4
024-C9-C10-N11	55.76	-72.14	-66.89	-77.4
C14-C13-C18-C19	-13.16	-109.36	-130.22	106.82
C7-C6-022-C23	–	–	-177.97	-171.07
N11-C25-C26-C27	94.19	90.64	89.15	–

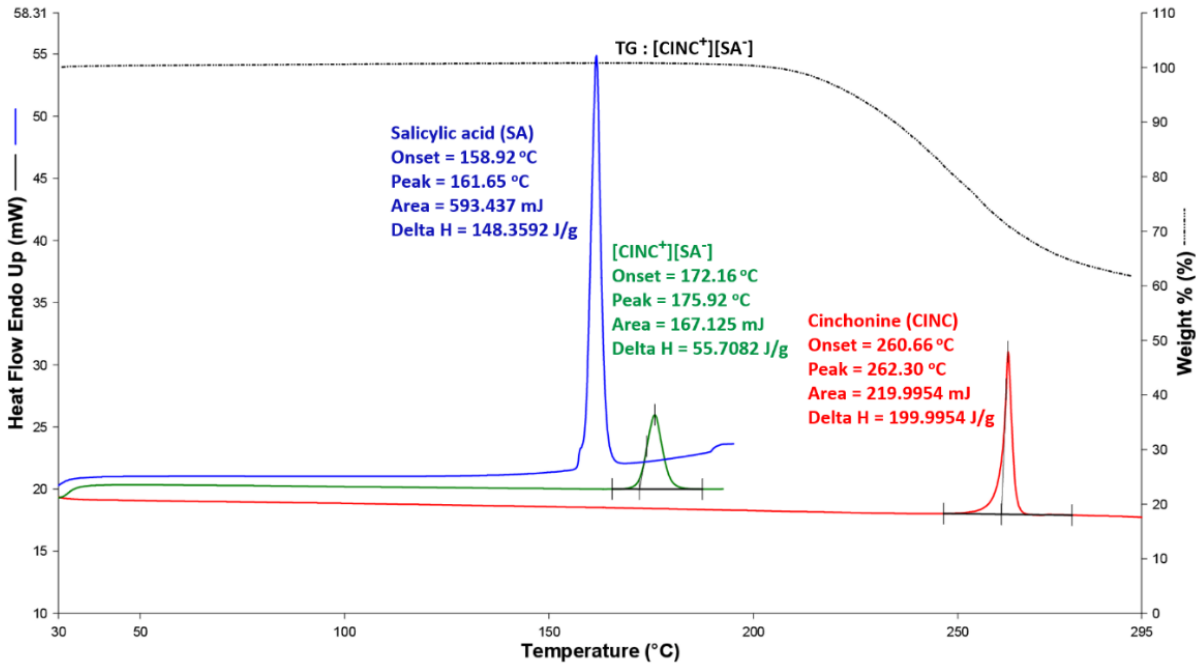

Figure A1 DSC curve for SA, CINC and [CINC$^+$][SA$^-$], plus the TGA curve for [CINC$^+$][SA$^-$].

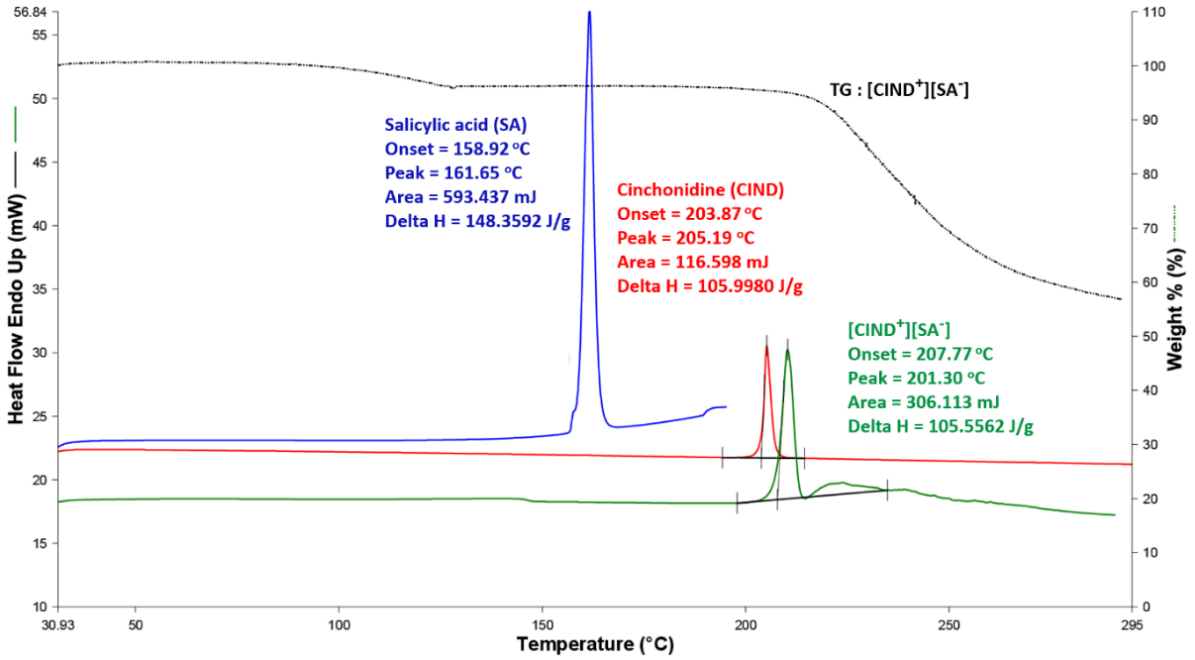

Figure A2 DSC curve for SA, CIND and [CIND⁺][SA⁻], and the TGA curve for [CIND⁺][SA⁻].

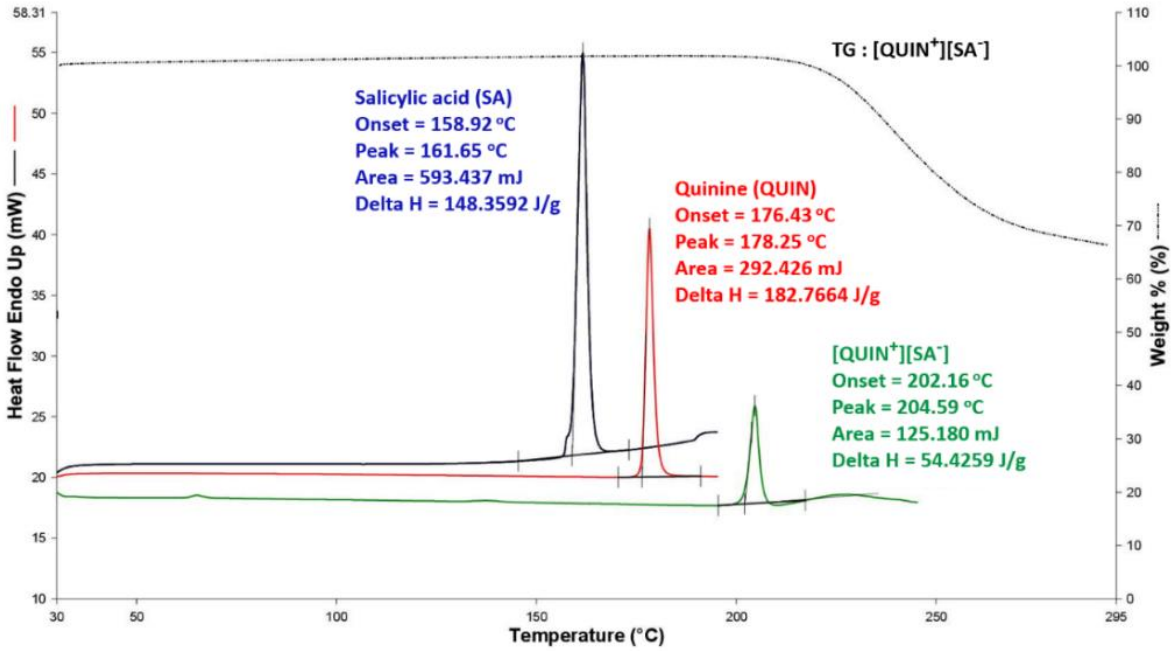

Figure A3 DSC curve for SA, QUIN and [QUIN⁺][SA⁻], and the TGA curve for [QUIN⁺][SA⁻].

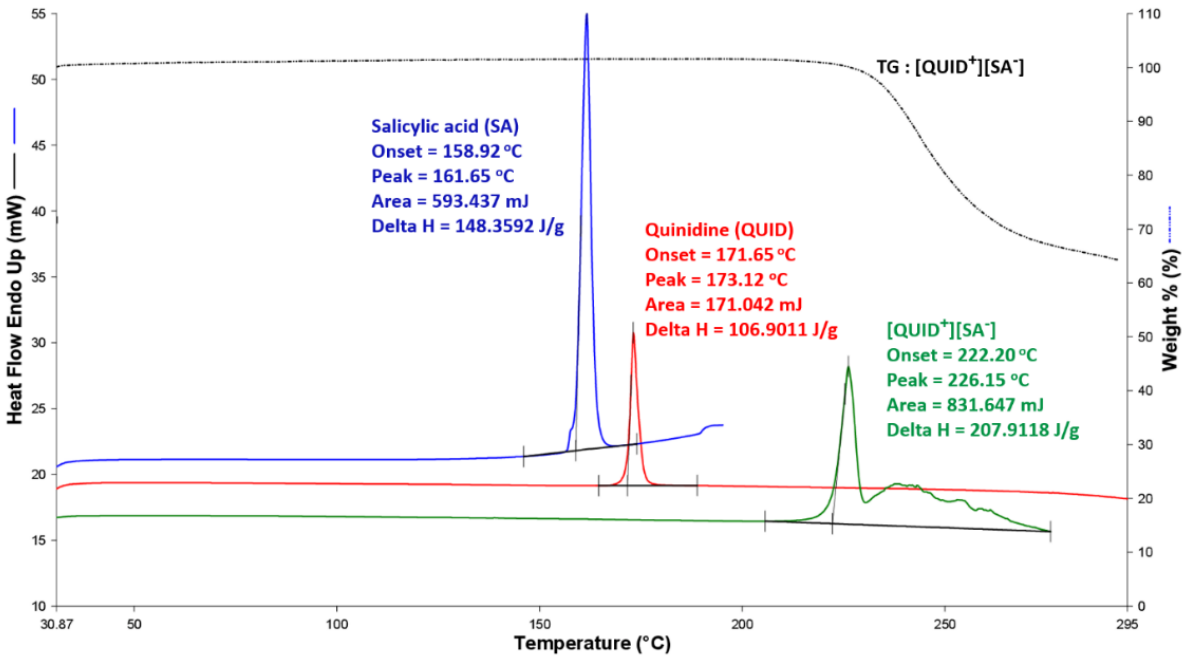

Figure A4 DSC curve for SA, QUID and [QUID⁺][SA⁻], and the TGA curve for [QUID⁺][SA⁻].

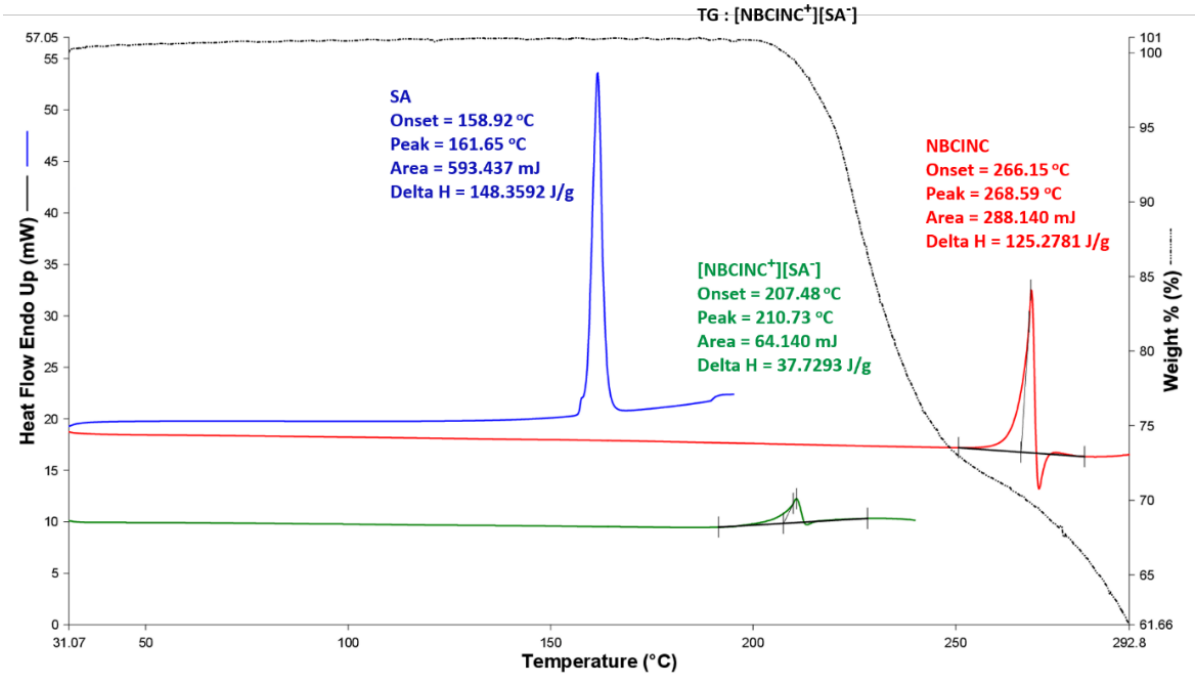

Figure A5 DSC curve for SA, NBCINC and [NBCINC⁺][SA⁻], and the TGA curve for [NBCINC⁺][SA⁻].

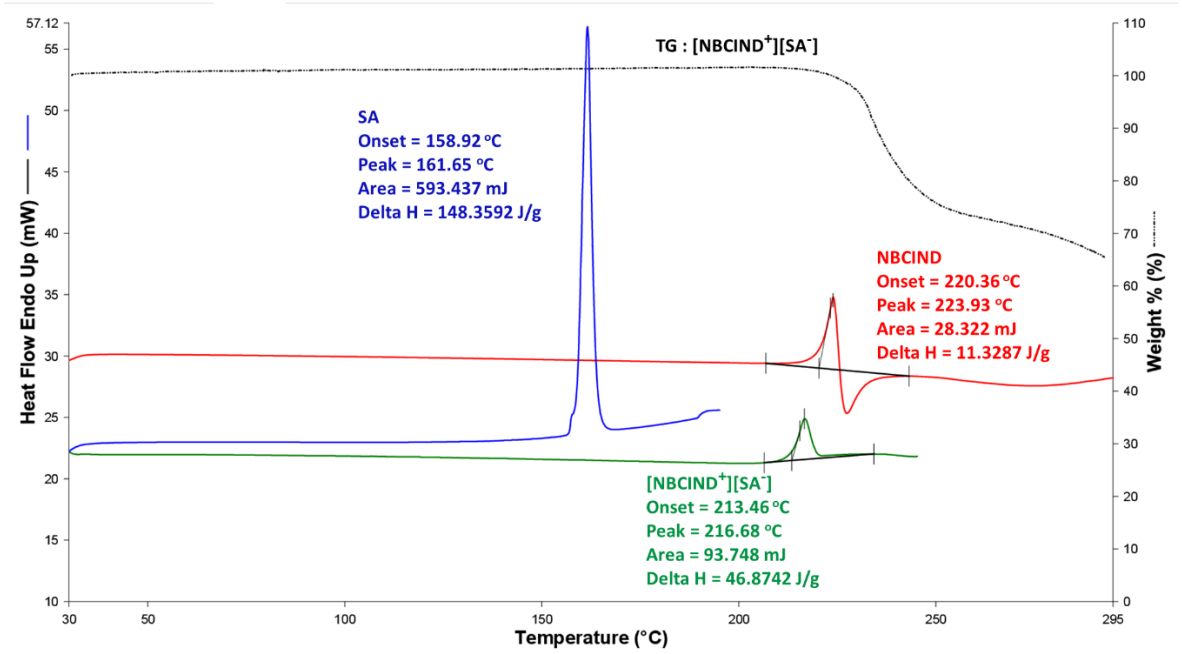

Figure A6 DSC curve for SA, NBCIND and [NBCIND$^+$][SA$^-$], plus the TGA curve for [NBCIND$^+$][SA$^-$].

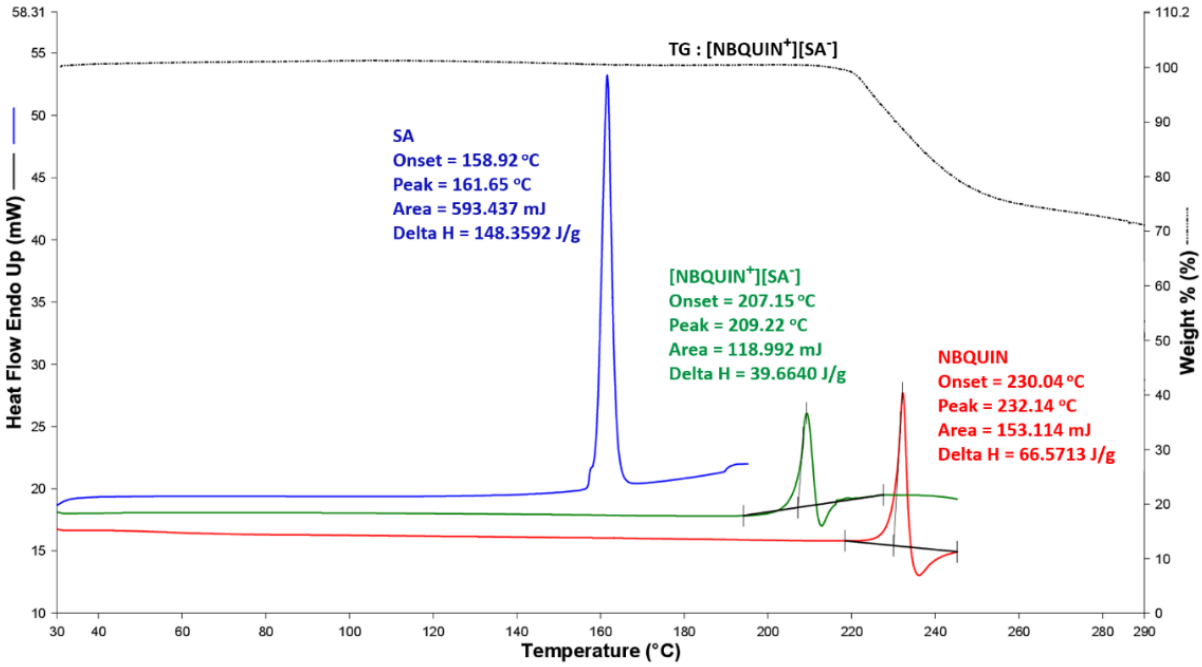

Figure A7 DSC curve for SA, NBQUIN and [NBQUIN$^+$][SA$^-$], plus the TGA curve for [NBQUIN$^+$][SA$^-$].

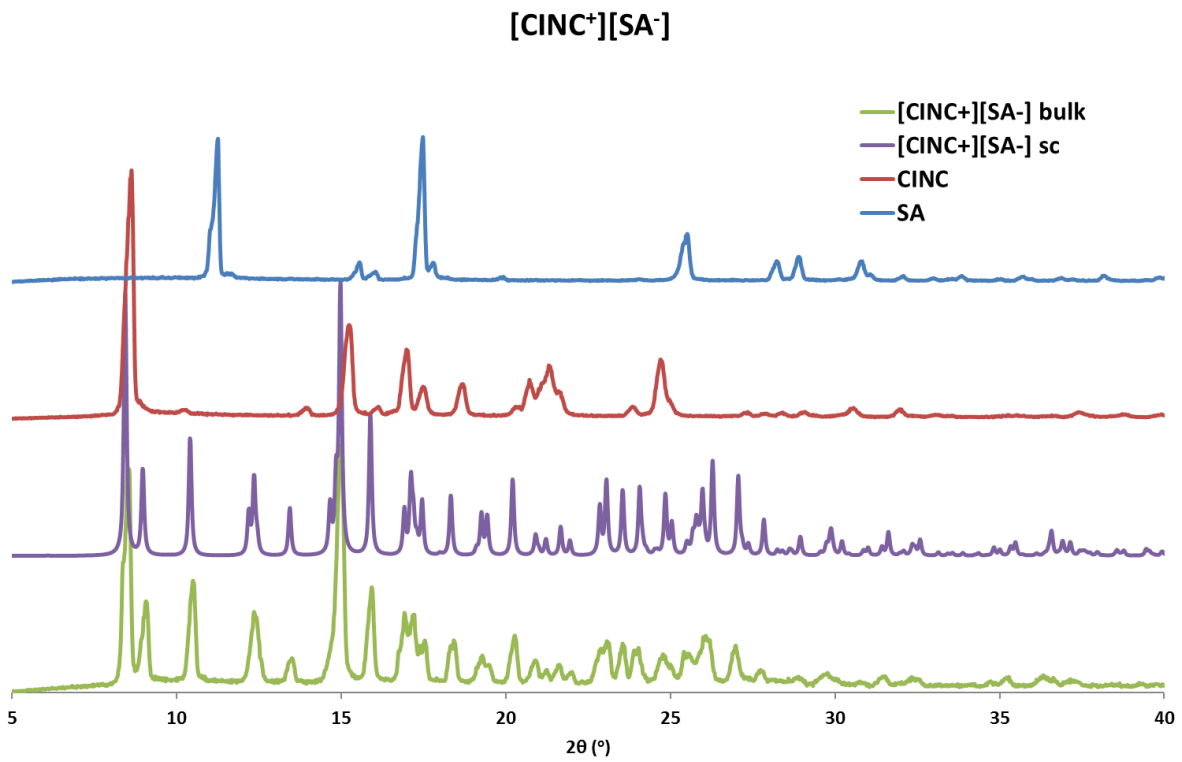

Figure A8 PXRD patterns of SA (blue), CINC (red), [CINC$^+$][SA$^-$] generated from single crystal (purple) and [CINC$^+$][SA$^-$] from bulk (green).

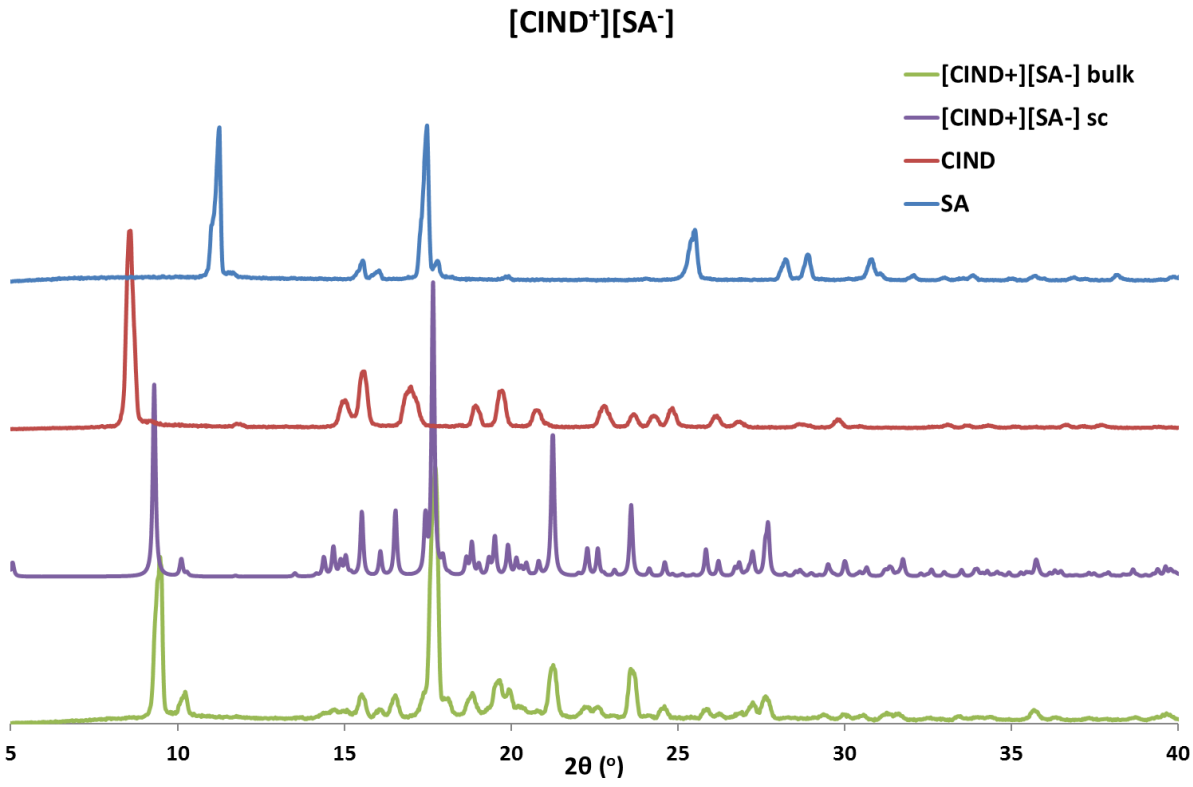

Figure A9 PXRD patterns of SA (blue), CIND (red), [CIND$^+$][SA$^-$] generated from single crystal (purple) and [CIND$^+$][SA$^-$] from bulk (green).

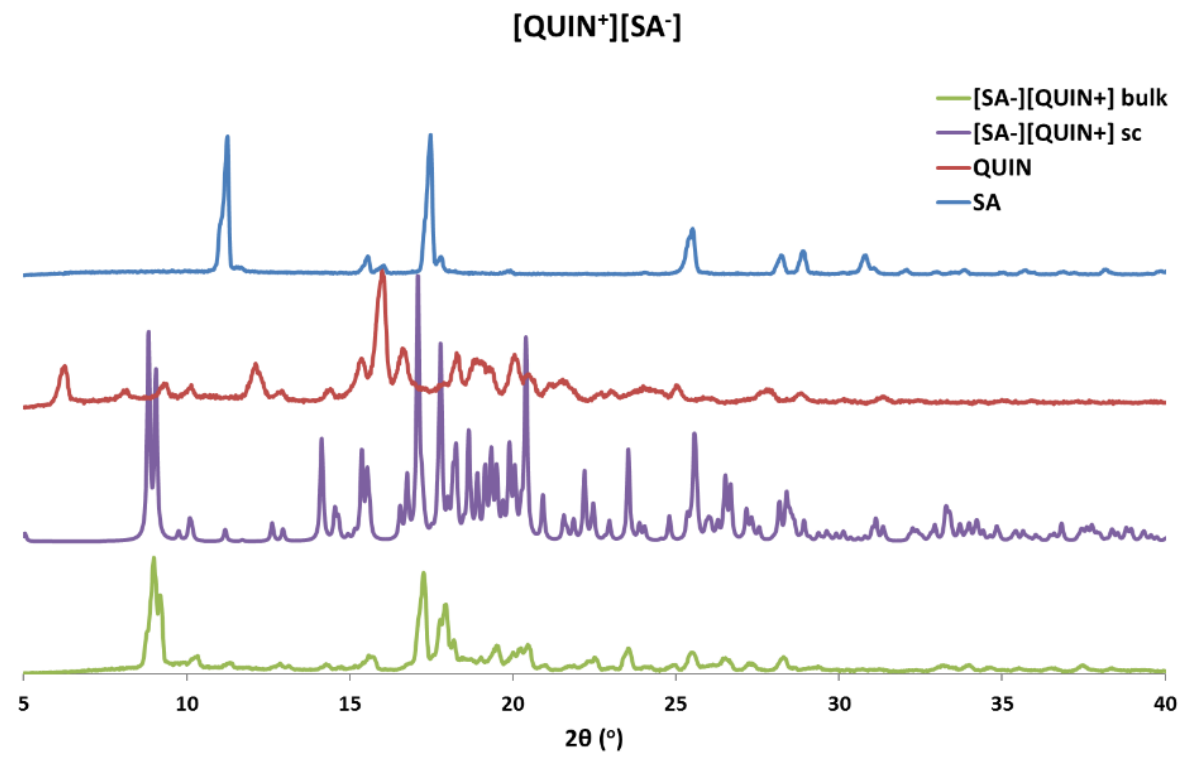

Figure A10 PXRD patterns of SA (turquoise), QUIN (red), [QUIN⁺][SA⁻] generated from single crystal (purple) and [QUIN⁺][SA⁻] from bulk (green).

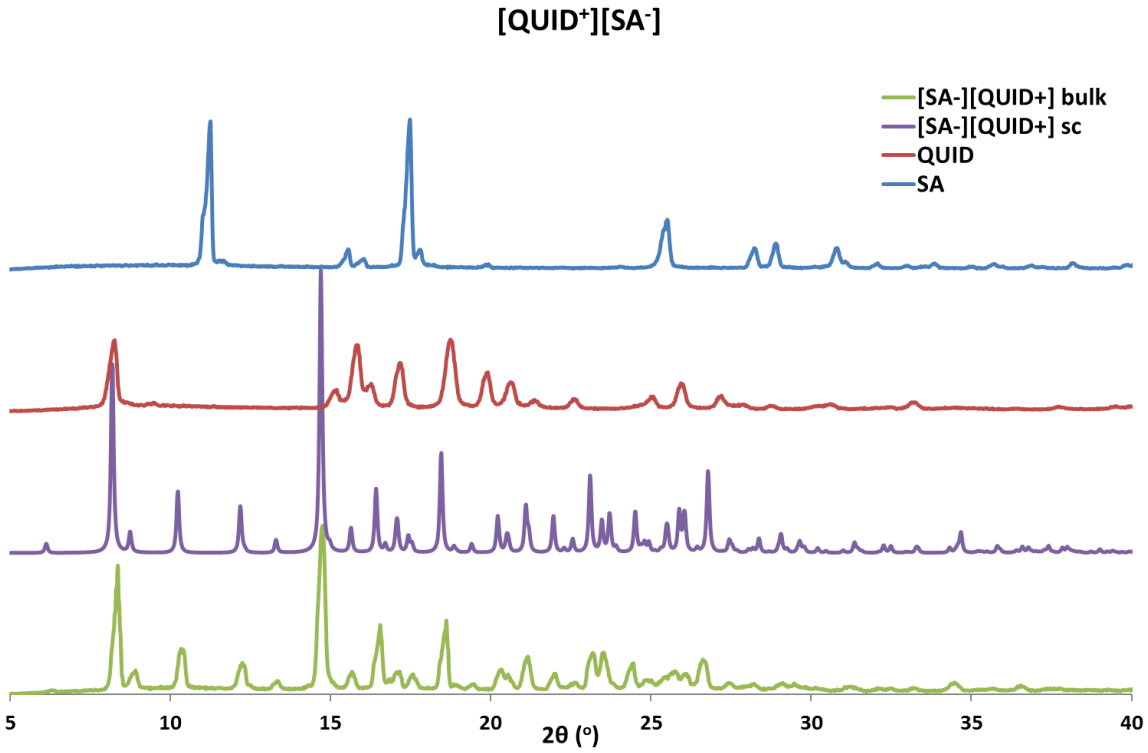

Figure A11 PXRD patterns of SA (turquoise), QUID (red), [QUID⁺][SA⁻] generated from single crystal (purple) and [QUID⁺][SA⁻] from bulk (green).

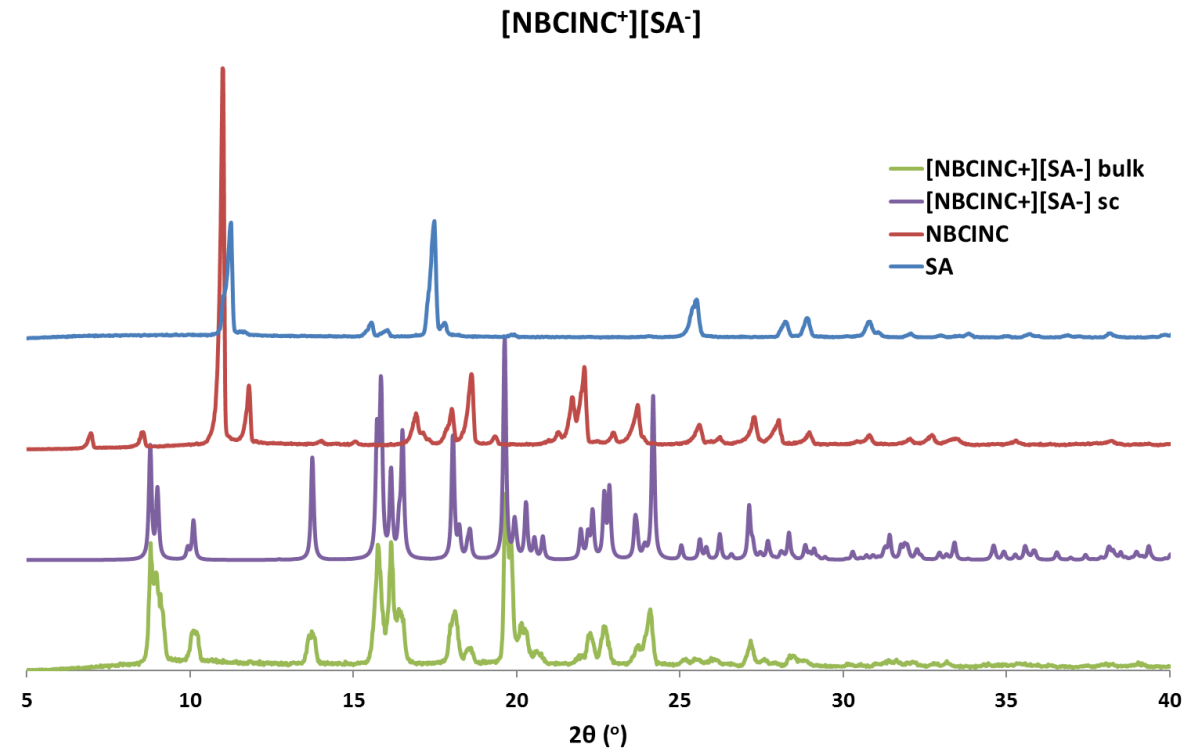

Figure A12 PXRD patterns of SA (blue), NBCINC (red), [NBCINC$^+$][SA$^-$] generated from single crystal (purple) and [NBCINC$^+$][SA$^-$] from bulk (green).

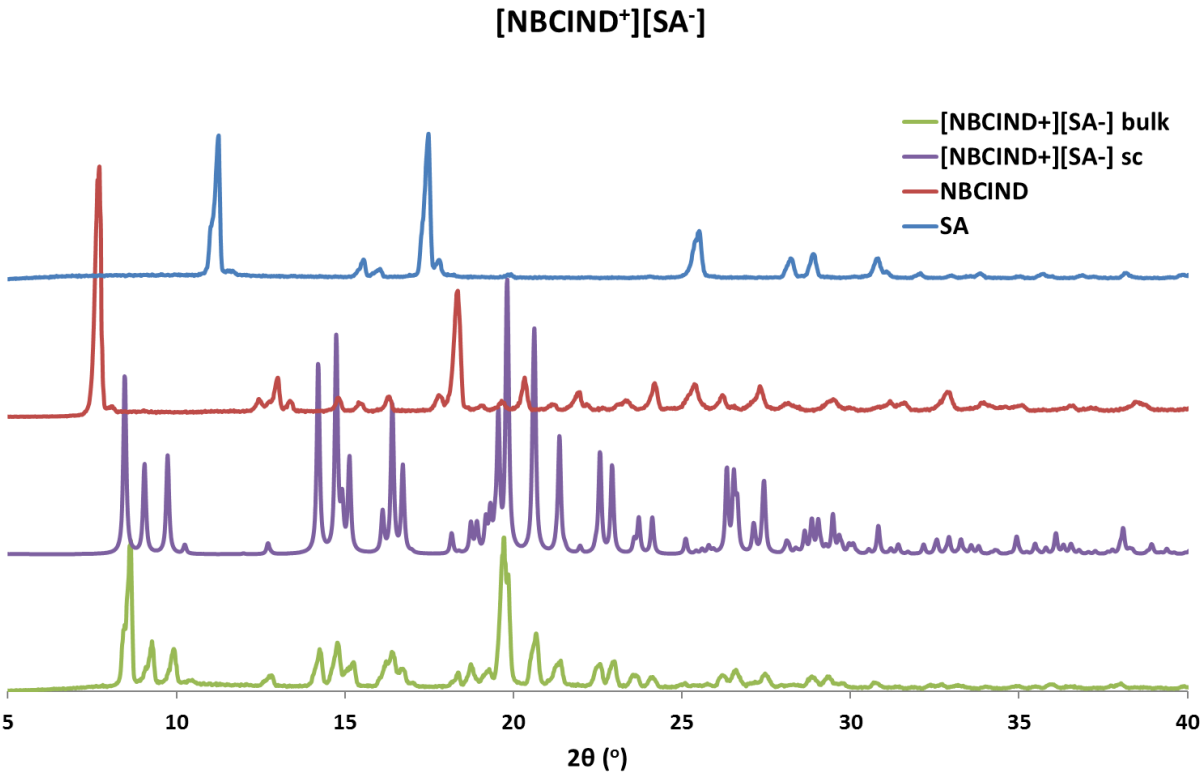

Figure A13 PXRD patterns of SA (blue), NBCIND (red), [NBCIND$^+$][SA$^-$] generated from single crystal (purple) and [NBCIND$^+$][SA$^-$] from bulk (green).

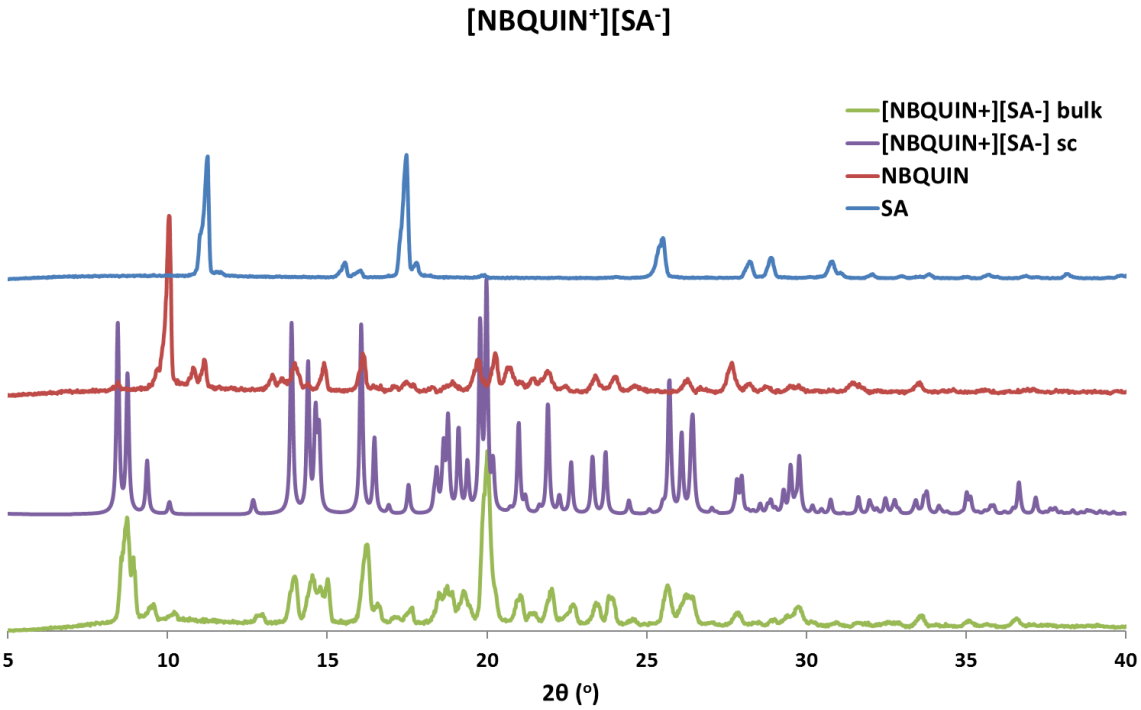

Figure A14 PXRD patterns of SA (blue), QUIN (red), [NBQUIN$^+$][SA$^-$] generated from single crystal (purple) and [NBQUIN$^+$][SA$^-$] from bulk (green).

Table A2 Salicylic acid calibration standard.

Concentration (mg/L)	Area
0.5	5253.3
1	34216.5
5	101915.5
20	244849.4
50	3496175.4
100	10403655.9
150	14453236.1
200	19682840.3

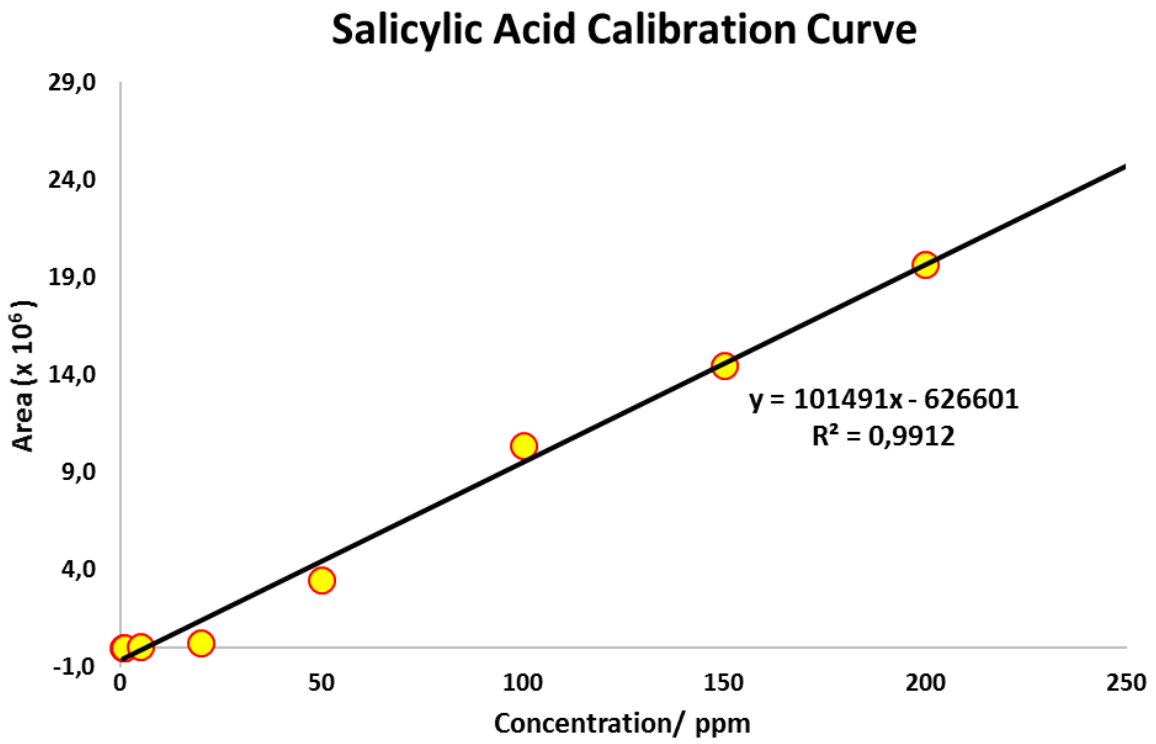

Figure A15 Salicylic acid calibration curve.

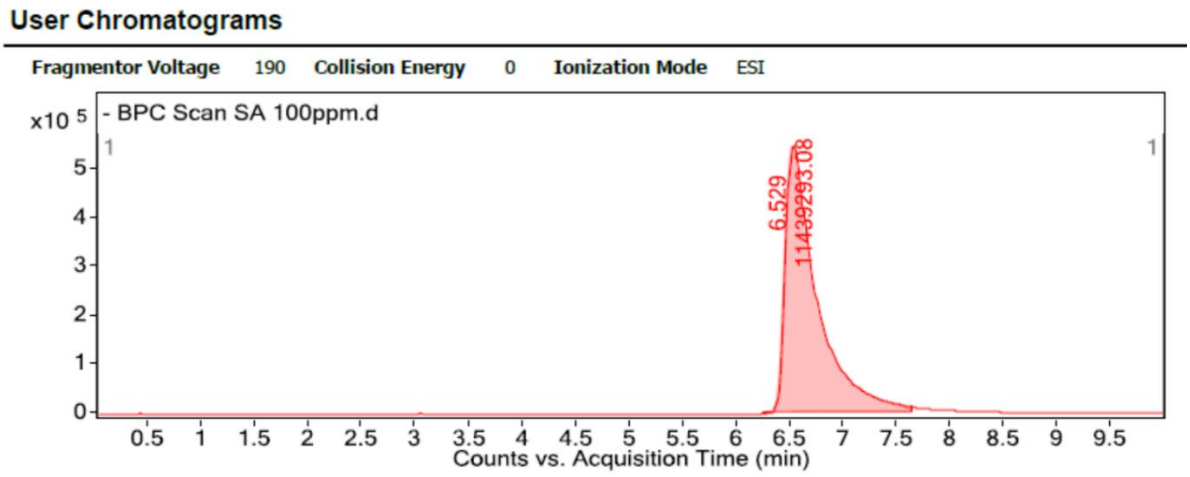

Integration Peak List

Peak	Start	RT	End	Height	Area	Area %
1	6.262	6.529	7.646	545965.35	11439293.08	100

Figure A16 BPC chromatogram of salicylic acid standard injection.

User Chromatograms

Fragmentor Voltage 190 **Collision Energy** 0 **Ionization Mode** ESI

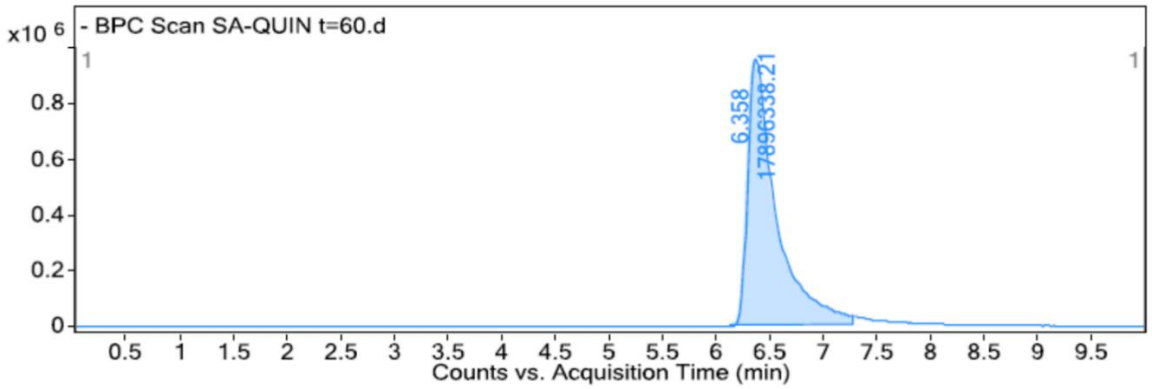

Integration Peak List

Peak	Start	RT	End	Height	Area	Area %
1	6.125	6.358	7.275	957768.06	17896338.21	100

Figure A17 BPC chromatogram of quininium salicylate dissolution at t=60min.

User Chromatograms

Fragmentor Voltage 190 **Collision Energy** 0 **Ionization Mode** ESI

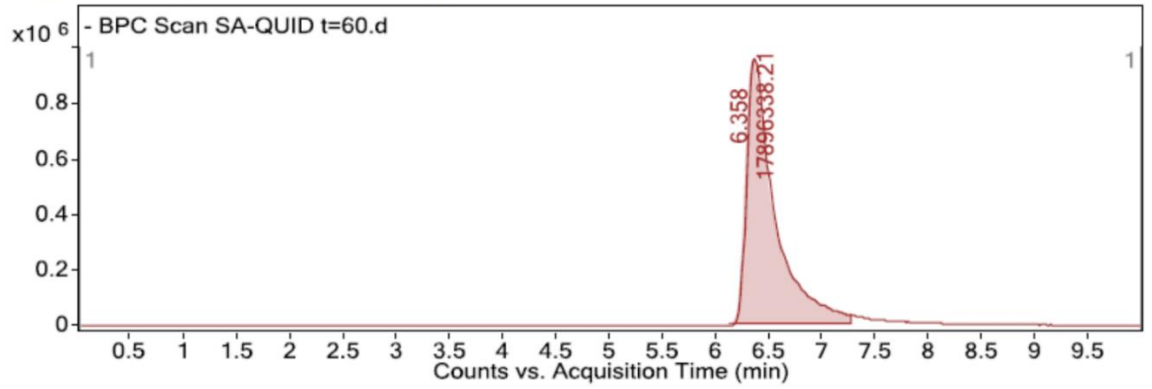

Integration Peak List

Peak	Start	RT	End	Height	Area	Area %
1	6.125	6.358	7.275	957768.06	17896338.21	100

Figure A18 BPC chromatogram of quinidinium salicylate dissolution at t=60min.

User Chromatograms

Fragmentor Voltage 190 **Collision Energy** 0 **Ionization Mode** ESI

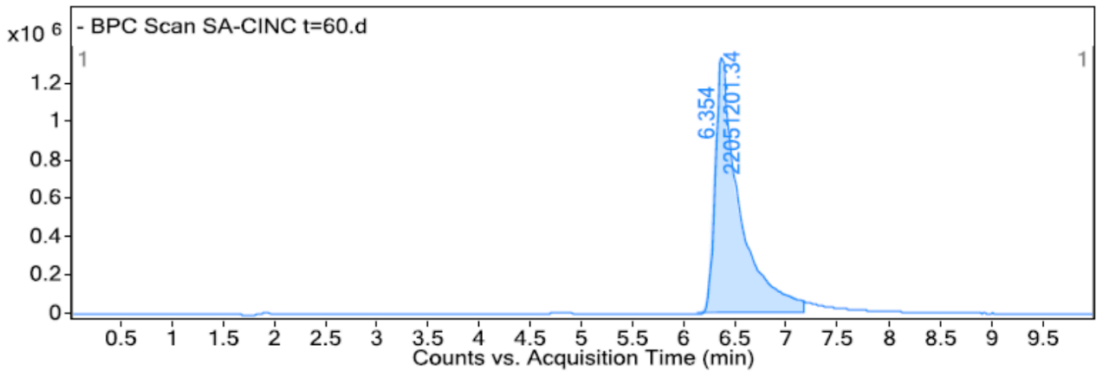

Integration Peak List

Peak	Start	RT	End	Height	Area	Area %
1	6.127	6.354	7.171	1327852.35	22051201.34	100

Figure A19 BPC chromatogram of cinchoninium salicylate dissolution at t=60min.

User Chromatograms

Fragmentor Voltage 190 **Collision Energy** 0 **Ionization Mode** ESI

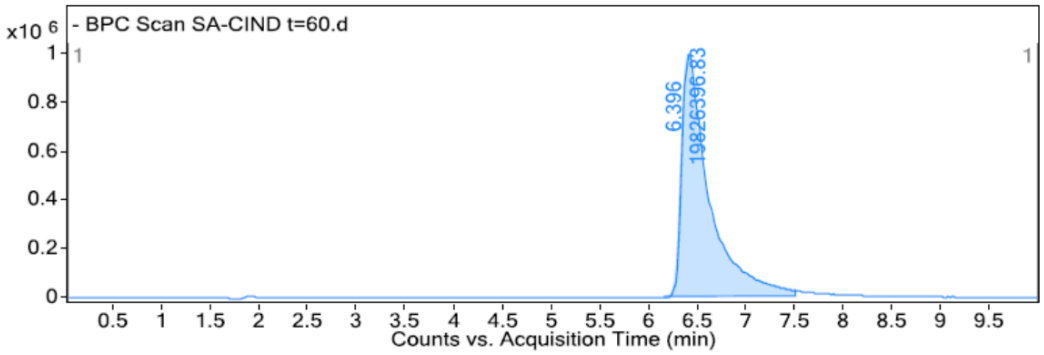

Integration Peak List

Peak	Start	RT	End	Height	Area	Area %
1	6.163	6.396	7.513	993471.3	19826396.83	100

Figure A20 BPC chromatogram of cinchonidinium salicylate dissolution at t=60min.

User Chromatograms

Fragmentor Voltage 190 Collision Energy 0 Ionization Mode ESI

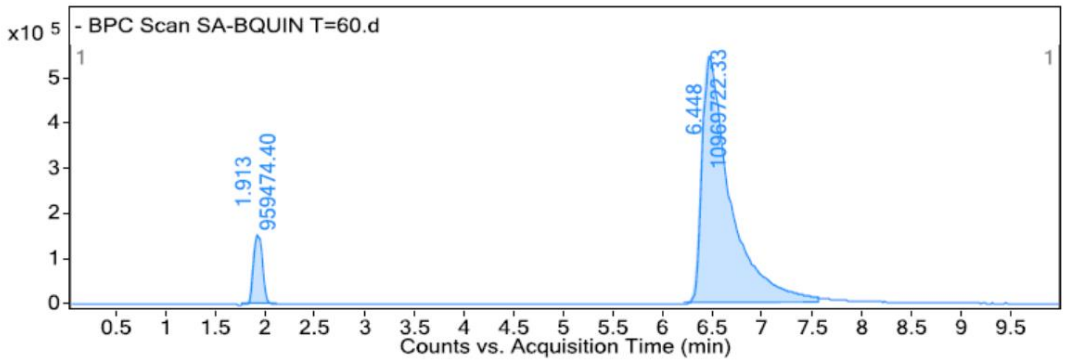

Integration Peak List

Peak	Start	RT	End	Height	Area	Area %
1	1.762	1.913	2.113	152542.17	959474.4	8.75
2	6.215	6.448	7.566	545494.33	10969722.33	100

Figure A21 BPC chromatogram of N-benzylquininium salicylate dissolution at t=60min.

User Chromatograms

Fragmentor Voltage 190 Collision Energy 0 Ionization Mode ESI

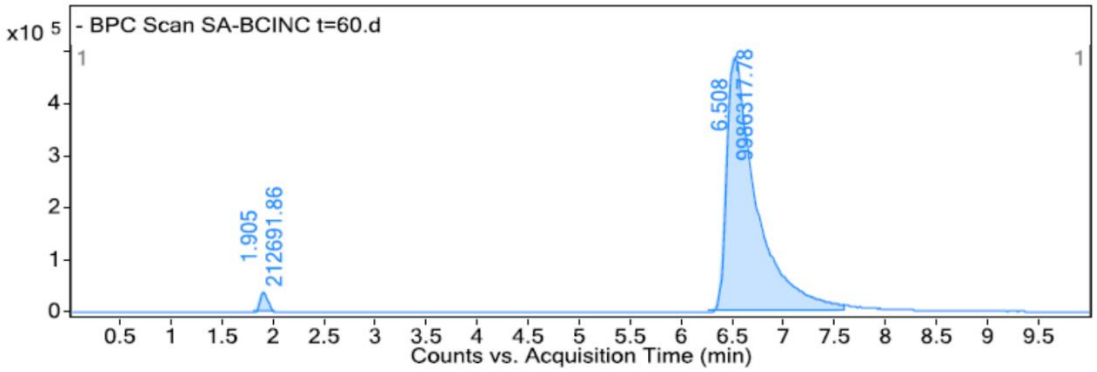

Integration Peak List

Peak	Start	RT	End	Height	Area	Area %
1	1.809	1.905	2.021	38978.79	212691.86	2.13
2	6.26	6.508	7.592	487084.19	9986317.78	100

Figure A22 BPC chromatogram of N-benzylcinchoninium salicylate dissolution at t=60min.

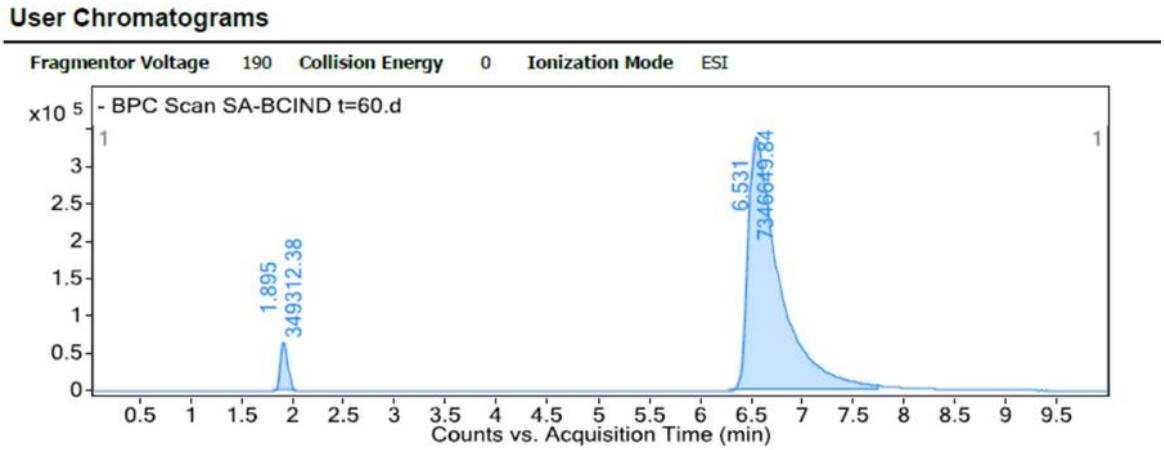

Integration Peak List

Peak	Start	RT	End	Height	Area	Area %
1	1.799	1.895	2.034	64616.61	349312.38	4.75
2	6.281	6.531	7.748	338425.04	7346649.84	100

Figure A23 BPC chromatogram of N-benzylcinchonidinium salicylate dissolution at t=60min.

Table A3 Cumulative concentrations of salicylic acid from multicomponent crystals.

	Concentration (mg/L)							
Time (min)	SA	[$QUIN^+$] [SA^-]	[$QUID^+$] [SA^-]	[$CINC^+$] [SA^-]	[$CIND^+$] [SA^-]	[$NBQUIN^+$] [SA^-]	[$NBCINC^+$] [SA^-]	[$NBCIND^+$] [SA^-]
0	0	0	0	0	0	0	0	0
5.0	271.0	110.4	112.9	212.5	115.8	72.2	65.0	26.4
15.0	400.0	145.2	148.4	239.1	146.9	89.4	91.7	44.2
30.0	469.6	149.4	166.3	231.9	186.5	98.5	96.9	60.7
45.0	474.7	154.7	178.0	221.9	193.7	105.5	98.3	71.3
60.0	500.1	165.4	182.5	223.4	201.5	114.3	104.6	78.6

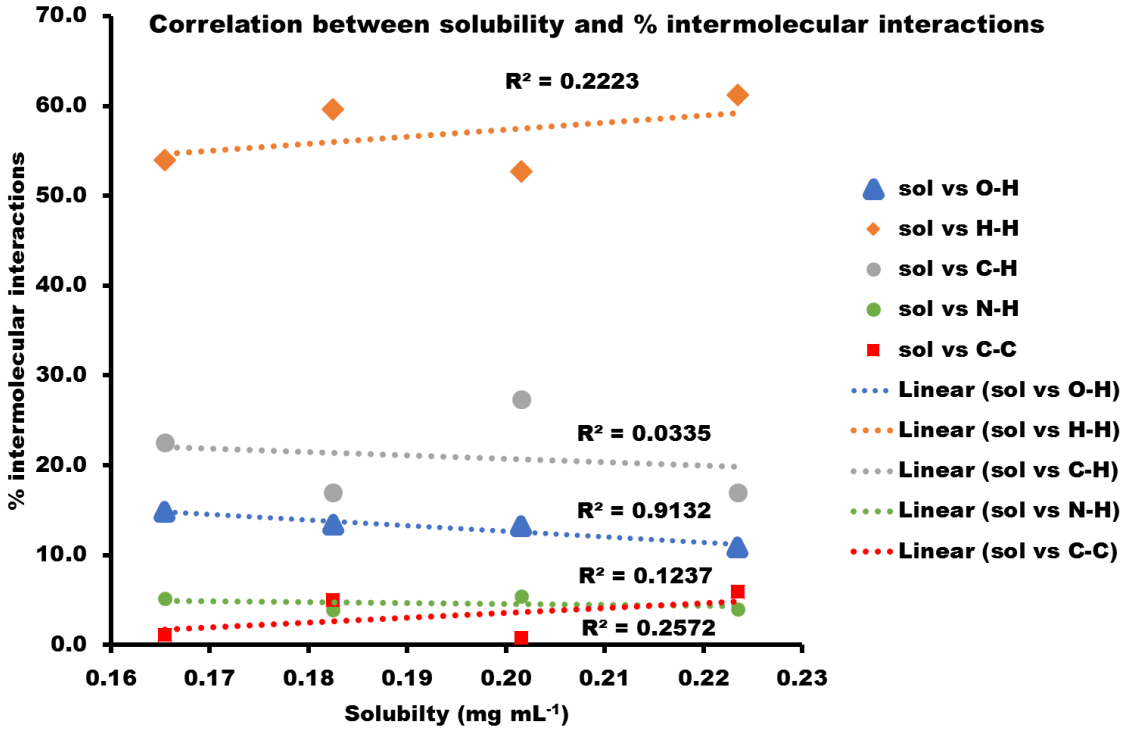

Figure A24 Correlation between solubility and the various intermolecular interactions in the unsubstituted cinchona alkaloids.

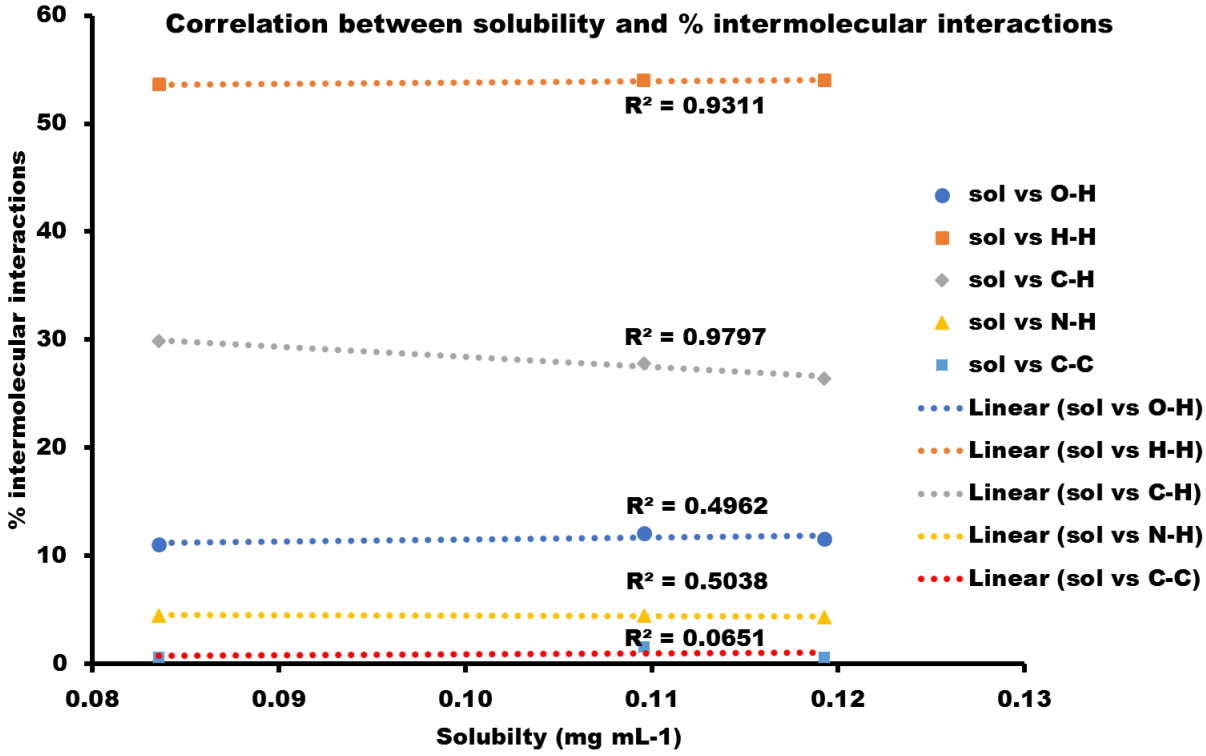

Figure A25 Correlation between solubility and the various intermolecular interactions in the N-benzyl substituted cinchona alkaloids.

User Chromatograms

Fragmentor Voltage 190 Collision Energy 0 Ionization Mode ESI

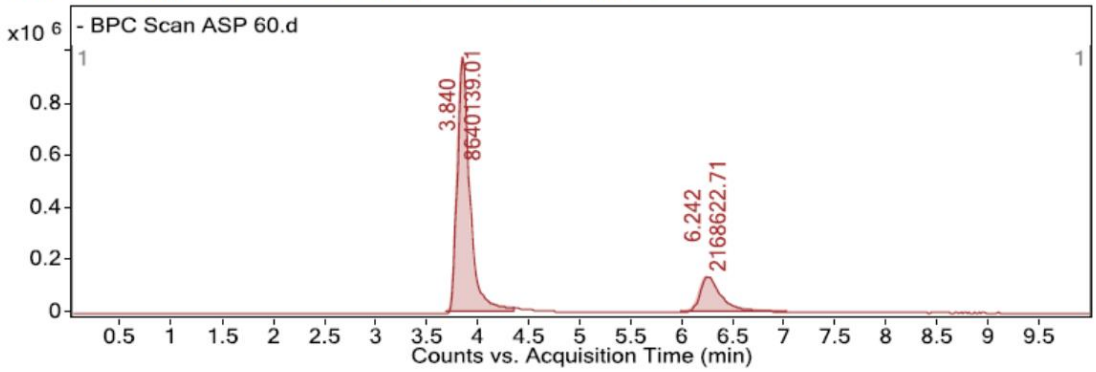

Integration Peak List

Peak	Start	RT	End	Height	Area	Area %
1	3.686	3.84	4.357	975663.6	8640139.01	100
2	5.991	6.242	7.025	138013.09	2168622.71	25.1

Figure A26 BPC chromatogram of acetylsalicylic acid dissolution at t=60min.

User Chromatograms

Fragmentor Voltage 190 Collision Energy 0 Ionization Mode ESI

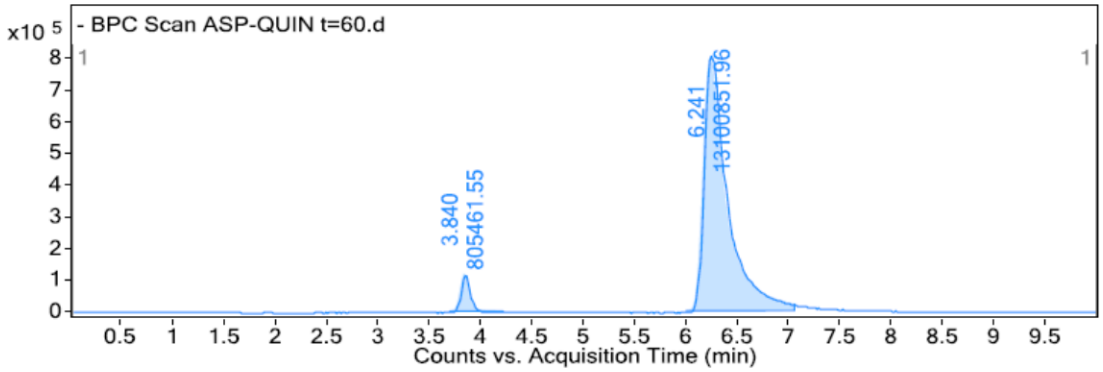

Integration Peak List

Peak	Start	RT	End	Height	Area	Area %
1	3.706	3.84	4.223	118960.92	805461.55	6.15
2	6.002	6.241	7.058	805871.5	13100851.96	100

Figure A27 BPC chromatogram of quininium acetylsalicylate dissolution at t=60min.

Table A.4 Cumulative concentrations of acetylsalicylic acid.

	HPLC response (Counts)	
Time (min)	ASP	$[QUIN^+][ASA^-]$
0	0.0	0.0
5	585834.3	836358.2
15	769789.1	904345.6
30	804774.0	923880.8
45	769688.7	948995.8
60	805461.6	975663.6